Electronic Supplementary Material (ESI) for Organic & Biomolecular Chemistry.
This journal is © The Royal Society of Chemistry 2023

Electronic Supplementally Information

Highly Chemoselective Ligands for Suzuki–Miyaura Cross-Coupling Reaction Based on Virtual Ligand-Assisted Screening

Wataru Matsuoka,*[ab] Yu Harabuchi,[abc] Yuuya Nagata,[bc] and Satoshi Maeda*[abcd]

[a]*Department of Chemistry, Faculty of Science, Hokkaido University, Sapporo, Hokkaido 060-0810, Japan.*

[b]*ERATO Maeda Artificial Intelligence for Chemical Reaction Design and Discovery Project, Hokkaido University, Sapporo, Hokkaido 060-0810, Japan.*

[c]*Institute for Chemical Reaction Design and Discovery (WPI-ICReDD), Hokkaido University, Sapporo, Hokkaido 001-0021, Japan.*

[d] *Research and Services Division of Materials Data and Integrated System (MaDIS), National Institute for Materials Science (NIMS), Tsukuba, Ibaraki 305-0044, Japan.*

e-mail addresses: matsuoka.wataru@sci.hokudai.ac.jp (W.Matsuoka),
smaeda@eis.hokudai.ac.jp (S.Maeda)

Table of Contents

1. Computational details

1.1 General

All energy and gradient calculations at the density functional theory (DFT) level were performed using the Gaussian 16[S1] software. Calculations at the GFN-xTB1 level were performed using the ORCA 4.2.0 software.[S2] Geometry optimization and automated reaction path searches using the single-component artificial force induced reaction (SC-AFIR) method were conducted in the developer version of the GRRM software[S3]. The Gibbs free energy values were estimated assuming a harmonic vibrational model, where all harmonic frequencies below 50 cm^{-1} were set to 50 cm^{-1}, as suggested in the literature.[S4] It is well known that gas-phase calculations overestimate the translational and rotational entropies of a molecule in solution because the solute molecule is surrounded by solvent molecules, which limits its translational and rotational motion. This can lead to significant errors in the Gibbs free energy when comparing systems with different numbers of molecules. Therefore, we applied the empirical correction method suggested by Martin *et al.*[S5]. Specifically, a correction of 4.3 kcal/mol was added to the Gibbs free energy of a system consisting of n+1 molecules when compared to a system consisting of n molecules, as described in the literature. [S5,S6]

The TEP values and cone angles of **L1**–**L62** were determined as follows. First, the conformational isomers of $LNi(CO)_3$, where L represents the corresponding ligand, were systematically explored using the SC-AFIR method[S3] at the GFN1-xTB level.[S7] All obtained conformers were then re-optimized in vacuo at the ωB97X-D/def2-SVP level with the "Grid=FineGrid" option, and harmonic vibrational frequency analyses were performed at the same computational level. Using the optimized $LNi(CO)_3$ structures, the cone angle of each conformer was calculated geometrically based on the definition.[S8] The TEP value was determined as the frequency of the (pseudo)symmetrical C–O vibrational mode, which was determined by the harmonic vibrational frequency analysis.[S9] Representative values of the cone angle and the TEP were calculated based on the obtained cone angles, TEP values, and relative Gibbs free energies for all conformers, as shown in Tables S2 and S3.

The TEP values and cone angles of **K1**–**K18** were determined as follows. The initial structures of $LNi(CO)_3$ were prepared based on the Cartesian coordinates of all accessible conformers for each ligand obtained from *kraken.*[S10] Geometry optimizations of these initial structures and subsequent harmonic vibrational frequency analyses were then performed in vacuo at the ωB97X-D/def2-SVP level using the "Grid=FineGrid" option. Using the optimized $LNi(CO)_3$ structures, the cone angle of each conformer was calculated geometrically based on the definition.[S8] The TEP value was determined as the frequency of the (pseudo)symmetrical C–O vibrational mode, which was determined by the harmonic vibrational frequency analysis.[S9] Representative values of the cone angle and the TEP were calculated based on the obtained cone angles, TEP values, and relative Gibbs free energies for all conformers, as shown in Table S4.

1.2 Procedure for the VLA screening

The VLA screening calculations were performed in the following four steps: (1) automated reaction path search using the SC-AFIR method with **VL1**, (2) path refinement calculations using the locally updated planes (LUP) method with **VL1**, (3) transition state (TS) optimizations using **VL2** and (4) parameter screening using **VL2**.

STEP 1: The automated reaction path search using the SC-AFIR method with **VL1**

The reaction path network for the oxidative addition of compound **1** to the Pd complex Pd(**VL1**)$_2$ (Fig. 3b) was obtained as follows: Automated reaction path searches using the SC-AFIR method were performed using the B3LYP functional, the LanL2DZ basis set with an effective core potential (ECP) for Pd, the 6-31G(d) basis set for S, and the 6-31G basis set for other atoms with the "Grid=FineGrid" option. The search was initiated using one of the stable geometries of compound **1** and Pd(**VL1**)$_2$. The target atoms for the SC-AFIR method were set as the Pd atom, the P atoms in the virtual ligands, and the C, O, and Cl atoms involved in the reaction. The model collision energy parameter (γ), which defines the strength of the artificial force, was set to 300 kJ/mol. In addition, weak forces ($\gamma = 100/{}_N C_2$, where N is the number of atoms) were applied between each pair of atoms to prevent the molecules from being too far apart. The electronic and steric parameters of **VL1** were set to reproduce those of PPh_3 (Table S7). All obtained AFIR paths were re-optimized using the LUP method.[S11] All reaction path searches were guided by a kinetic-based navigation method, where the obtained equilibrium structures (EQs) were evaluated based on the so-called traffic volume determined by the rate constant matrix contraction (RCMC) method,[S12] and the EQ to which the next SC-AFIR procedure was applied was chosen, as detailed previously.[S13] Kinetic analyses were performed based on the Gibbs free energies and the LUP path network. In this kinetic-based navigation, an initial population of one was assigned to the initial structure. The highest traffic volume among those obtained at the three reaction temperatures (200, 300, and 400 K) was regarded as the traffic volume for each EQ. The reaction time was set to 3600 s (1 h). Based on this kinetic navigation, the SC-AFIR procedure was applied only to EQs in which the bond connectivity of compound **1** remains unchanged to effectively explore the oxidative addition paths of compound **1**. The searches were terminated when 1000 effective AFIR paths were computed.

STEP 2: Path refinement calculations using the LUP method with **VL1**

All paths extracted from the reaction path network based on the criteria described in the manuscript (Fig. 3b and related discussions) were refined using the LUP method[S11] at the ωB97X-D/def2-SVP level and the "Grid=FineGrid" option. To consider the solvent effects, the implicit solvation SMD model[S14] (THF) was applied (hereafter, this computational level is denoted as *CL1*). Like the automated reaction path search calculation, the parameters of **VL1** were set to reproduce those of PPh_3 (Table S7).

STEP 3: TS optimizations using **VL2**

The geometry optimizations of **PT1**–**PT12** (Fig. 3b of the manuscript) were performed using **VL2**. The entire paths which include these PTs (obtained in Step 2) were further refined using the LUP method at the same computational level (*CL1*), employing **VL2**$_{\mathbf{PAr3}}$ rather than **VL1**. The parameters of **VL2**$_{\mathbf{PAr3}}$ were set to match those of PPh_3 (r_0 = 1.657 Å for the keep potential and θ = 165° for the cone potential). Following that, we performed the geometry optimizations of the transition states

at *CL1*, starting from the refined PTs and using the same virtual ligand. For the geometry optimizations of monoligated species (PTs corresponding to **PT4**–**PT6** and **PT10**–**PT12**), a virtual ligand that was not coordinated to the Pd atom was removed beforehand.

STEP 4: Parameter screening using **VL2**

Geometry optimization of **TS$_{CO–PdL1}$**, **TS$_{CO–PdL2}$**, **TS$_{CCl–PdL1}$**, and **TS$_{CCl–PdL2}$** (Fig. 3b of the manuscript) was performed using **VL2$_{PAr3}$** or **VL2$_{PR3}$** with 90 combinations of electronic and steric parameters (r_0 = 1.3, 1.4, 1.5, 1.6, 1.7, 1.8, 1.9, 2.0 or 2.1 Å for the keep potential, and θ = 120, 130, 140, 150, 160, 170, 180, 190, 200 or 210° for the cone potential) at the computational level *CL1*. Specifically, using the optimized structures for these TSs obtained in Step3 (**VL2$_{PAr3}$**, r_0 = 1.657 Å, and θ = 165°) as the initial structures, we performed geometry optimizations of the TSs with virtual ligand(s) (**VL2$_{PAr3}$** or **VL2$_{PR3}$**) with each combination of parameters. In certain cases, the calculation did not converge to the desired TS structure due to an inappropriate initial structure. In such cases, the corresponding TS structure was obtained by performing geometry optimization from the TS structure obtained using the same virtual ligand with the closest combination of parameters (arrows in Fig. S1). In addition, certain calculations of bis-ligated species (**TS$_{CO–PdL2}$** and **TS$_{CCl–PdL2}$**) with bulky virtual ligands (mainly θ = 200 and 210°) did not result in the desired TS structure due to the dissociation of the virtual ligand. These TSs were considered to be energetically unfavorable compared to the corresponding monoligated species (**TS$_{CO–PdL1}$** and **TS$_{CCl–PdL1}$** with the same parameters of the virtual ligands). The results of the parameter screening are summarized in Fig. S1. In these plots, each cross indicates the geometry optimization of the corresponding TS with the corresponding parameters of the virtual ligand successfully converged.

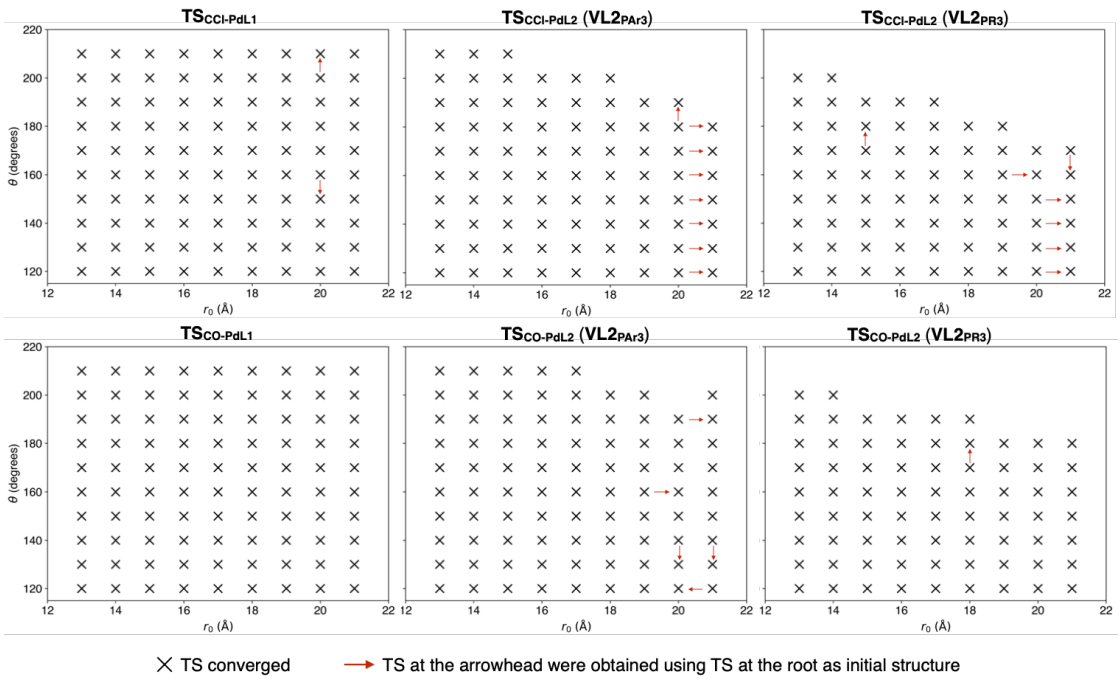

Fig. S1. Summary of the parameter screening.

2. Experimental details

2.1 General

Unless otherwise stated, all reactants and reagents, including dry solvents, were obtained from commercial suppliers and used as received. $Pd_2(dba)_3$, **L39**, **L40**, **L47**–**L50**, **L53**, and **L60**–**L62** were purchased from Sigma-Aldrich. 2-Methylphenyl boronic acid, potassium fluoride, **L33**–**L38**, **L41**–**L46**, **L51**, **L52**, and **L54**–**L59** were purchased from Tokyo Chemical Industry Co. Ltd. Tetrahydrofuran was purchased from Kanto Chemical Co., Inc. 4-Chlorophenyl triflate,[S15] **K9**,[S16] and **K14**[S17] were synthesized according to a previously reported procedure. Unless otherwise stated, all reactions were carried out in dry solvents under an atmosphere of N_2 or Ar gases in dried glassware, using standard vacuum-line techniques. Unless otherwise stated, all workup and purification procedures were performed using reagent-grade solvents in the air. Gas chromatography (GC) analysis was conducted using a Shimadzu GC-2025 instrument equipped with a DB-1 column (15 m × 0.320 mm, Agilent), with dodecane as an internal standard. All reactions were carried out using a Chemspeed SWING robotic platform with an iSynth reactor containing 48 individual reactors.

2.2 Experimental procedure

General procedure for chemoselective SMC reaction with **L33**–**L62** (Fig. 5)

$Pd_2(dba)_3$ (6.2 mg, 6.74 μmol, 1.5 mol%) and 2-methylphenyl boronic acid (61.2 mg, 0.45 mmol, 1.0 equiv) were added to an 8-mL vial, which was set in the iSynth reactor on the Chemspeed platform. The vial was then evacuated and refilled with Ar gas three times. The vial was opened under a flow of Ar gas and a THF solution (0.45 mL) containing 4-chlorophenyl triflate (72.9 μL, 0.45 mmol, 1.0 equiv) and dodecane (18 μL, internal standard for GC analysis) was added. Then, a 0.03 M THF solution of ligand (0.45 mL, 0.0135 mmol, 3.0 mol%) was added to the vial, and the vial was closed. The mixture was stirred for 30 min at room temperature, and the vial was opened under Ar gas flow. A 1.5 M degassed aqueous solution of KF (0.90 mL, 1.35 mmol, 3.0 equiv) was added to the vial and the vial was closed. The mixture was then stirred for 12 h at 70 °C. Following that, the mixture was cooled to room temperature and THF was removed under reduced pressure at 40 °C. CH_2Cl_2 (4.5 mL) was added to the vial and the resulting mixture was stirred for 5 min. A small amount of the organic phase (about 1.0 mL) was collected from this mixture and passed through a short pad of silica gel (eluent: ethyl acetate). The resulting solution was analyzed by GC without further purification.

General procedure for chemoselective SMC reaction with **K9** or **K14** (Fig. 6c)

To a J. Young Schlenk tube containing a magnetic stirring bar, $Pd_2(dba)_3$ (6.2 mg, 6.74 μmol, 1.5 mol%), 2-methylphenyl boronic acid (61.2 mg, 0.45 mmol, 1.0 equiv), and **K9** (5.9 mg, 0.0135 mmol, 3.0 mol%) or **K14** (3.3 mg, 0.0135 mmol, 3.0 mol%) were added. The tube was then evacuated and refilled with N_2 gas three times. THF (0.90 mL) and 4-chlorophenyl triflate (72.9 μL, 0.45 mmol, 1.0 equiv) were added to the tube under the flow of N_2 gas. The tube was sealed with a cap, and the mixture was stirred for 30 min at room temperature. The tube was then opened under the flow of N_2 gas, and a 1.5 M degassed aqueous solution of KF (0.90 mL, 1.35 mmol, 3.0 equiv) was added. The tube was sealed with a cap, and the mixture was stirred for 12 h at 70 °C. The mixture was cooled to room temperature and diluted with CH_2Cl_2 (about 5 mL). Dodecane (18 μL,

internal standard for GC analysis) was added to the mixture, and the resulting mixture was vigorously stirred. A small amount of the organic phase (about 100 μL) was collected from this mixture and passed through a short pad of silica gel (eluent: ethyl acetate). The resulting solution was analyzed by GC without further purification.

2.3 Experimental results

The experimental results obtained for **L33**–**L62**, **K9** and **K14** are summarized in Table S1. For all ligands, the experiments were repeated twice, and the averaged values of $\Delta\Delta G^{\ddagger}$ were used in the discussion.

Table S1. Experimental results for **L33**–**L62**, **K10** and **K14**.

	Run 1		Run 2		Average	
Ligand	Yield (%)	$\Delta\Delta G^{\ddagger}$ (kcal/mol)	Yield (%)	$\Delta\Delta G^{\ddagger}$ (kcal/mol)	Yield (%)	$\Delta\Delta G^{\ddagger}$ (kcal/mol)
L33	0.14	-	0.09	-	0.12	-
L34	N.D.	-	0.03	-	0.03	-
L35	20.39	3.47	5.79	2.59	13.09	3.03
L36	58.18	4.24	59.67	4.19	58.93	4.21
L37	1.21	-0.10	2.38	0.28	1.79	0.09
L38	0.37	-	0.35	-	0.36	-
L39	68.65	4.05	65.98	4.04	67.32	4.05
L40	36.32	4.94	35.09	4.02	35.70	4.48
L41	2.51	1.35	2.47	1.35	2.49	1.35
L42	35.97	3.27	43.67	3.60	39.82	3.43
L43	14.88	2.96	31.54	3.62	23.21	3.29
L44	0.79	-	0.88	-	0.84	-
L45	19.92	3.59	17.47	3.55	18.69	3.57
L46	0.65	-	0.56	-	0.60	-
L47	58.39	4.29	60.60	4.30	59.50	4.30
L48	34.11	3.79	27.35	3.65	30.73	3.72
L49	38.61	3.82	33.20	3.76	35.91	3.79
L50	0.75	-	0.89	-	0.82	-
L51	66.54	4.52	69.69	4.43	68.11	4.48
L52	0.91	-	0.86	-	0.89	-
L53	0.55	-	0.49	-	0.52	-
L54	3.56	1.90	2.80	1.91	3.18	1.91
L55	11.34	3.05	6.58	2.75	8.96	2.90
L56	8.76	2.58	4.55	2.36	6.66	2.47
L57	2.19	1.83	N.D.	-	2.19[a]	1.83[a]
L58	9.77	3.55	5.23	3.30	7.50	3.43
L59	53.48	-1.97	50.70	-1.59	52.09	-1.78
L60	26.24	-1.91	27.32	-1.98	26.78	-1.95
L61	33.39	3.97	45.46	4.04	39.42	4.01
L62	11.84	3.28	10.01	3.39	10.92	3.34
K09	13.44	-1.47	15.26	-1.77	14.35	-1.62
K14	12.60	-3.35	14.69	-3.54	13.64	-3.44
no ligand	0.02	-	0.04	-	0.03	-

[a] Run 2 was excluded.

3. List of calculated ligands and their parameters

3.1 Calculated TEP and cone angle

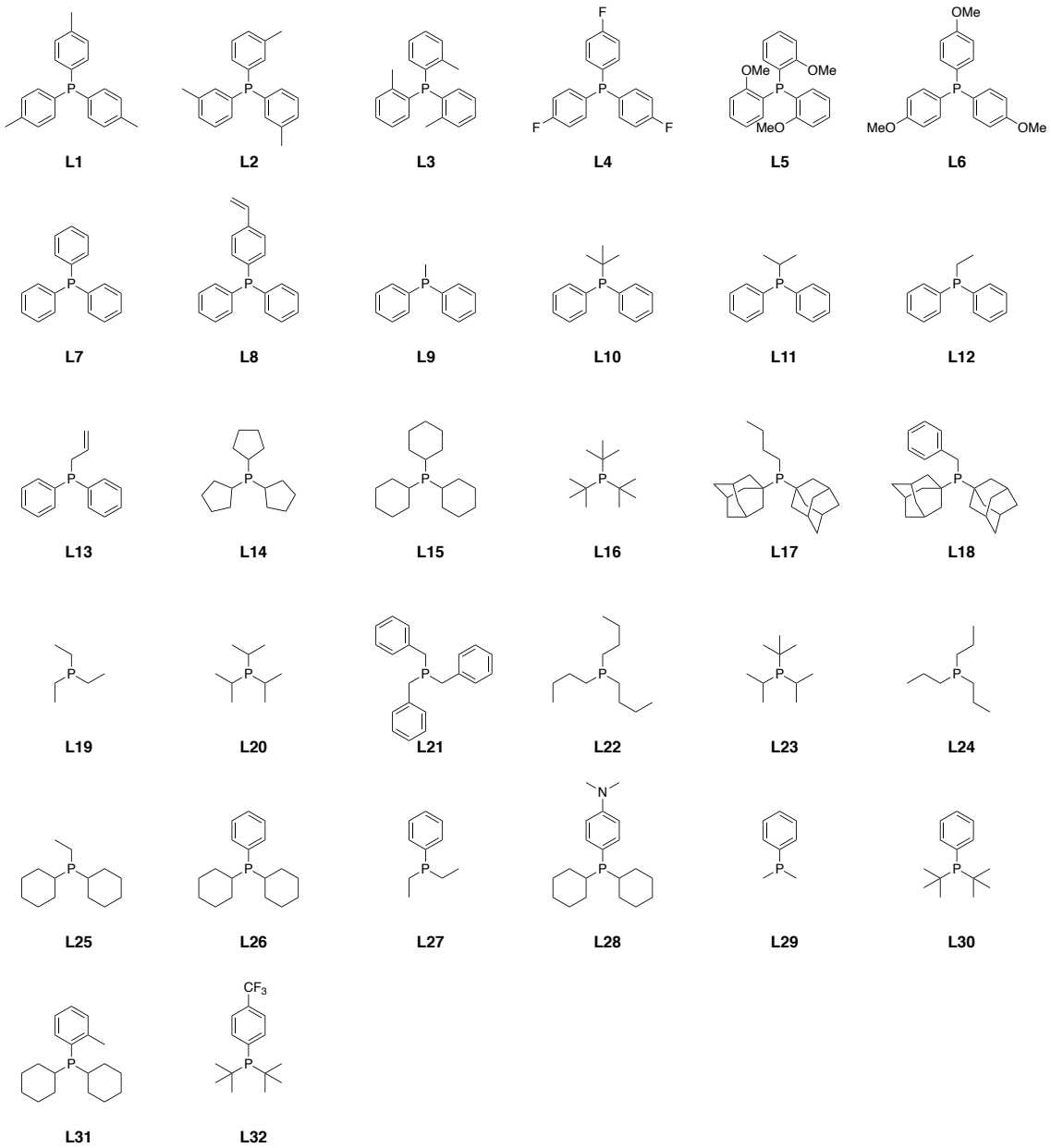

Fig. S2. Chemical structure of Phosphine ligands **L1**–**L32**.

Table S2. Calculated cone angles and TEP values of phosphine ligands **L1**–**L32**.

	most stable conformer		minimum cone angle conformer		Boltzmann-weighted average	
Ligand	θ (°)	ν_{CO} (cm^{-1})	θ (°)	ν_{CO} (cm^{-1})	θ (°)	ν_{CO} (cm^{-1})
L1	165	2221	165	2221	166	2220
L2	172	2220	166	2221	170	2220
L3	202	2216	168	2216	202	2216
L4	166	2225	166	2225	166	2225
L5	204	2202	175	2209	204	2202
L6	167	2219	166	2220	167	2218
L7	166	2223	166	2223	166	2223
L8	166	2222	166	2222	166	2222
L9	152	2221	150	2222	151	2221
L10	164	2216	164	2216	164	2216
L11	171	2218	159	2215	167	2217
L12	170	2222	145	2220	163	2220
L13	174	2221	158	2219	164	2220
L14	171	2208	162	2210	173	2209
L15	175	2210	166	2208	174	2210
L16	185	2206	185	2206	185	2206
L17	182	2208	168	2206	181	2208
L18	189	2209	168	2208	191	2209
L19	170	2216	143	2216	165	2216
L20	174	2211	168	2213	175	2212
L21	205	2217	161	2217	203	2217
L22	172	2214	136	2216	171	2214
L23	176	2212	173	2210	177	2212
L24	168	2214	142	2217	166	2215
L25	173	2213	152	2209	171	2212
L26	176	2213	156	2212	173	2214
L27	168	2219	134	2217	167	2219
L28	176	2211	160	2211	173	2211
L29	141	2221	141	2221	141	2221
L30	185	2213	185	2213	185	2213
L31	180	2213	167	2210	180	2213
L32	184	2216	184	2215	184	2215

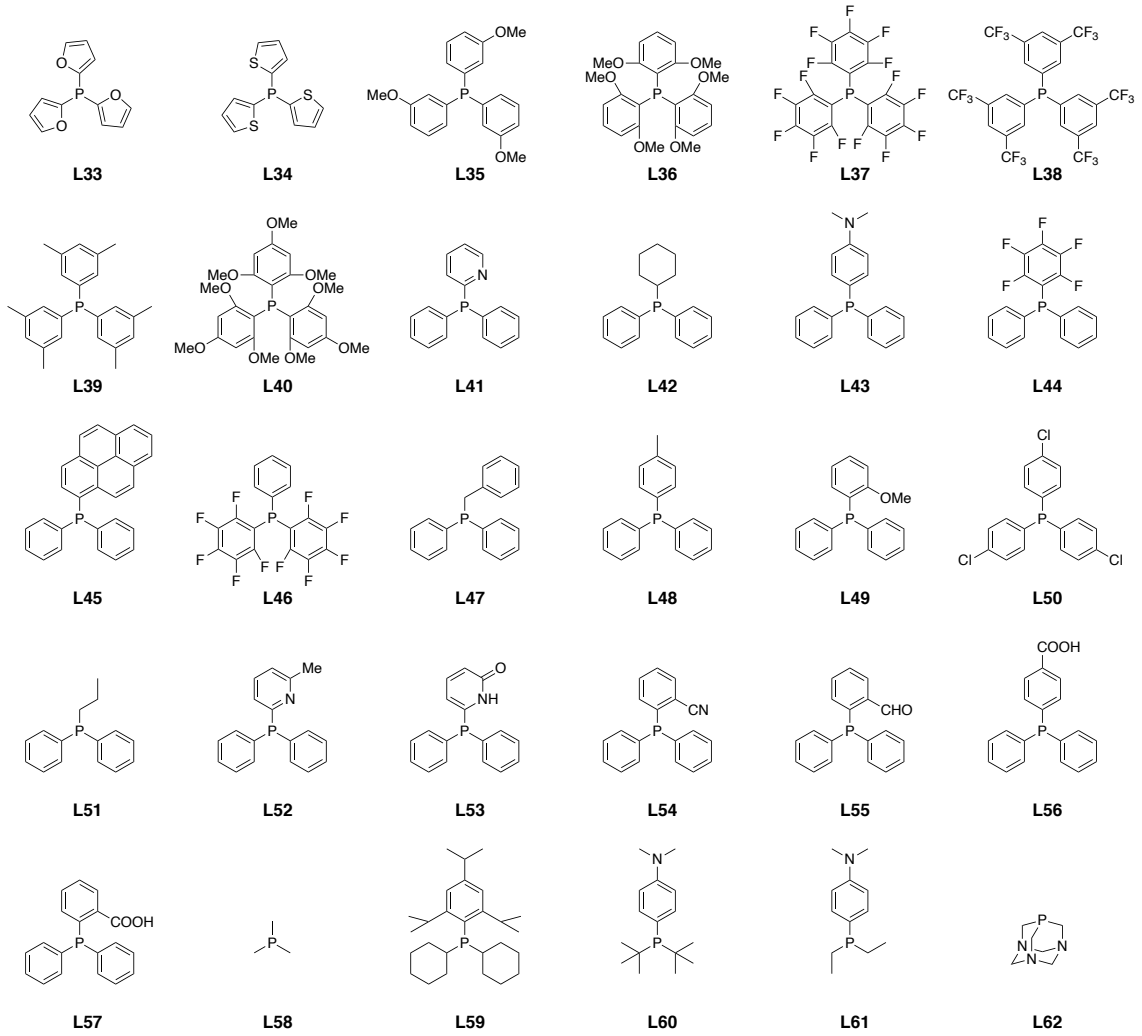

Fig. S3. Chemical structure of Phosphine ligands **L33**–**L62**.

Table S3. Calculated cone angles and TEP values of phosphine ligands **L33**–**L62**.

	most stable conformer		minimum cone angle conformer		Boltzmann-weighted average	
Ligand	θ (°)	ν_{CO} (cm^{-1})	θ (°)	ν_{CO} (cm^{-1})	θ (°)	ν_{CO} (cm^{-1})
L33	164	2229	142	2228	162	2229
L34	171	2226	161	2228	167	2227
L35	200	2216	164	2223	182	2219
L36	210	2196	199	2199	209	2197
L37	173	2232	159	2238	173	2232
L38	185	2235	179	2235	185	2235
L39	172	2219	172	2219	175	2219
L40	208	2194	200	2196	208	2195
L41	163	2220	150	2221	161	2221
L42	171	2219	154	2214	168	2218
L43	166	2220	166	2220	166	2220
L44	166	2226	166	2224	168	2226
L45	173	2220	162	2220	172	2220
L46	167	2232	167	2232	167	2232
L47	170	2219	149	2217	171	2219
L48	166	2221	166	2221	166	2221
L49	175	2216	163	2219	175	2216
L50	166	2226	166	2226	166	2226
L51	170	2219	145	2218	164	2219
L52	172	2221	160	2220	167	2221
L53	165	2227	165	2227	165	2227
L54	174	2225	161	2221	173	2225
L55	169	2224	161	2222	169	2223
L56	166	2221	166	2221	166	2222
L57	175	2221	158	2222	176	2221
L58	120	2219	120	2219	120	2219
L59	200	2211	175	2208	199	2210
L60	185	2212	185	2212	185	2212
L61	168	2214	137	2214	168	2214
L62	115	2224	115	2224	115	2224

The chemical structures of the ligands **K1**–**K18** are shown in the manuscript (Fig. 6b). **K1**, **K3**, **K4**, **K5**, and **K11** are the same molecules as **L58**, **L19**, **L62**, **L20**, and **L16**, respectively, but the procedure used to calculate each parameter (primarily conformation sampling) is different (Section 1.1 in the ESI). We confirmed that the parameters for each ligand obtained using the two procedures were largely similar.

Table S4. Calculated cone angles and TEP values of phosphine ligands **K1**–**K18**.

	most stable conformer		minimum cone angle conformer		Boltzmann-weighted average	
Ligand	θ (°)	ν_{CO} (cm^{-1})	θ (°)	ν_{CO} (cm^{-1})	θ (°)	ν_{CO} (cm^{-1})
K1	120	2219	120	2219	120	2219
K2	128	2219	128	2219	128	2219
K3	170	2216	143	2214	161	2216
K4	115	2224	115	2224	115	2224
K5	175	2213	168	2211	175	2212
K6	173	2216	133	2215	170	2217
K7	120	2228	120	2228	120	2228
K8	104	2228	104	2228	104	2228
K9	187	2203	187	2203	187	2203
K10	140	2234	134	2230	140	2233
K11	185	2211	185	2208	185	2209
K12	182	2238	151	2234	171	2237
K13	205	2208	202	2209	205	2208
K14	205	2215	183	2211	205	2214
K15	169	2242	169	2242	169	2242
K16	206	2230	196	2233	206	2230
K17	138	2252	138	2252	138	2252
K18	183	2252	163	2252	179	2252

3.2 Predicted values of $\Delta\Delta G^{\ddagger}$

Table S5. Predicted $\Delta\Delta G^{\ddagger}$ using representative values of the TEP and the cone angle.

	$\Delta\Delta G^{\ddagger}_{predicted}$ (kcal/mol)		
Ligand	most stable conformer	minimum cone angle conformer	Boltzmann-weighted average
L1	4.57	4.57	4.88
L2	4.33	4.48	4.48
L3	-1.41	6.15	-1.22
L5	2.44	6.79	2.53
L6	5.27	5.09	5.50
L7	3.70	3.70	3.70
L8	4.09	4.09	4.17
L9	4.92	4.63	4.80
L10	6.50	6.50	6.50
L11	5.46	6.97	5.89
L12	4.02	5.54	5.00
L13	4.03	5.56	5.09
L14	4.72	5.97	4.14
L15	3.24	5.95	3.37
L16	-0.66	-0.66	-0.66
L17	0.88	5.92	1.43
L18	-4.53	5.44	-5.28
L19	2.48	6.09	3.74
L20	3.13	4.27	2.84
L21	-7.61	4.35	-7.51
L22	2.63	6.35	2.96
L23	2.34	3.65	2.15
L24	3.84	5.76	4.07
L25	2.96	7.57	3.57
L26	2.08	6.37	2.47
L27	2.16	5.93	2.50
L28	2.81	6.11	3.49
L29	4.34	4.34	4.34
L30	-2.28	-2.28	-2.28
L31	0.19	5.27	0.04
L32	-3.12	-2.90	-2.96
L35	-0.05	4.03	3.32
L36	1.40	5.22	1.27
L37	-0.67	-1.93	-0.67
L39	4.67	4.67	4.54
L40	2.51	5.40	2.25
L41	5.08	4.82	4.70
L42	4.98	7.28	5.41

Table S5. (continued)

Ligand	$\Delta\Delta G^{\ddagger}_{predicted}$ (kcal/mol) most stable conformer	minimum cone angle conformer	Boltzmann-weighted average
L43	4.95	4.95	4.95
L45	4.57	5.23	4.61
L47	5.20	6.33	5.10
L48	4.73	4.73	4.56
L49	5.31	5.61	5.32
L51	4.92	6.01	5.50
L54	2.20	4.78	2.46
L55	3.23	4.57	3.46
L56	4.59	4.59	4.10
L57	3.72	4.54	3.48
L58	5.64	5.64	5.64
L59	-7.03	4.00	-6.90
L60	-1.99	-1.99	-1.99
L61	3.70	6.91	3.88
L62	3.13	3.13	3.13
K1	–	–	5.73
K2	–	–	5.52
K3	–	–	4.54
K4	–	–	3.36
K5	–	–	2.53
K6	–	–	2.41
K7	–	–	2.10
K8	–	–	-0.30
K9	–	–	-0.37
K10	–	–	-0.66
K11	–	–	-1.83
K12	–	–	-6.29
K13	–	–	-7.37
K14	–	–	-7.55
K15	–	–	-8.30
K16	–	–	-8.58
K17	–	–	-8.86
K18	–	–	-9.51

4. Sampling of ligand–ligand interaction

4.1 Procedure and results

The interaction energies between the real ligands ($E_{\text{L-L}}$) were computationally sampled using the following procedure: Assuming that two real ligands coordinate to a single metal atom with a bite angle ϕ (the term was originally coined for bidentate ligands, but we applied it to two molecules of monodentate ligands for convenience), these ligands were placed 2.28 Å from the origin (**O**) while directing the lone pair orbital to the origin (Fig. S4a). Geometry optimization of the system was performed with the Cartesian coordinates of the phosphorus atoms (**P₁** and **P₂**) fixed at $\boldsymbol{p_1} = (2.28, 0, 0)$ and $\boldsymbol{p_2} = (2.28\cos\phi, 2.28\sin\phi, 0)$, respectively, at the ωB97X-D/def2-SV(P) level. During the optimization process, a penalty function was added to the electronic energy of the system to prevent the rotation of ligands other than around $\mathbf{OP_i}$ axes, thus preserving the direction of the lone pair orbitals. Specifically, in each iteration of the geometry optimization, a harmonic potential based on the angles ψ_i (i = 1–6) defined by **O**, the phosphorus atom (**P₁** or **P₂**), and each atom bonded to the phosphorus atom (α atom) was added, as shown in Fig. S4b, in the same manner as the keep potential (see Section 5.2 of the ESI for implementation). After the geometry optimization of the system, $E_{\text{L-L}}$ was calculated as follows:

$$E_{\text{L-L}} = E_{\text{system}} - 2E_{\text{L}}$$

where E_{system} is the electronic energy of the optimized system (without penalty) and E_{L} is the electronic energy of the corresponding ligand optimized independently. A combination of 23 ligands and six bite angles (ϕ = 90°, 100°, 110°, 120°, 140 °, and 180°) were sampled and are summarized in Table S6.

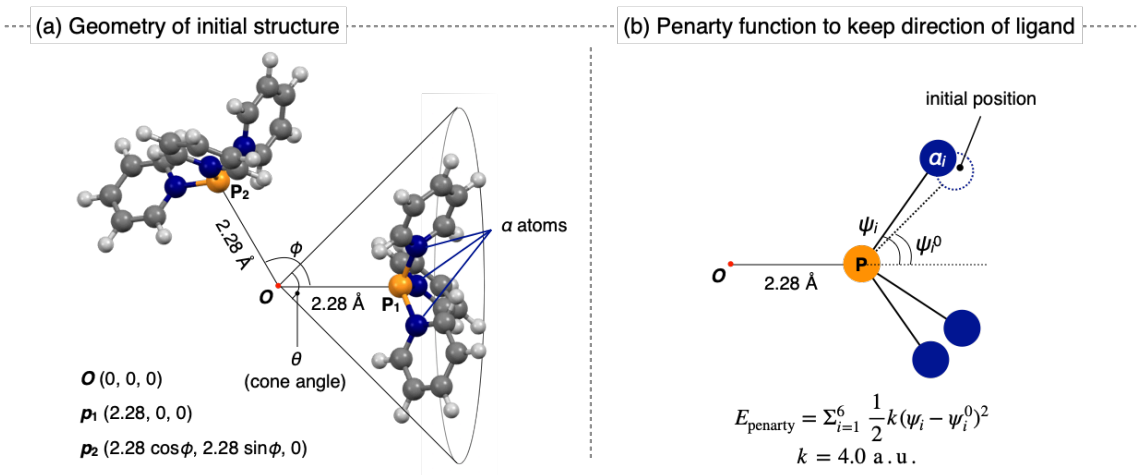

Fig. S4. Sampling procedure for L-L interaction energies ($E_{\text{L-L}}$) of real ligands.

Table S6. L-L interaction energies ($E_{\mathrm{L-L}}$) of various ligands and bite angles.

ligand	θ (°)	ϕ (°)	$E_{\mathrm{L-L}}$	ligand	θ (°)	ϕ (°)	$E_{\mathrm{L-L}}$
PCl_3	117	90	4.18	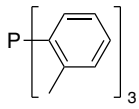	210	90	N.A.
		100	-1.16			100	4.61
		110	-1.73			110	-1.40
		120	-1.44			120	-7.49
		140	-0.88			140	-11.72
		180	-0.60			180	-8.95
PMe_3	117	90	11.05	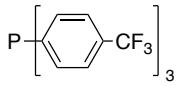	161	90	-3.30
		100	3.06			100	-9.35
		110	0.59			110	-11.11
		120	0.39			120	-10.12
		140	0.65			140	-6.76
		180	0.76			180	-2.24
$P(CCl_3)_3$	171	90	N.A.	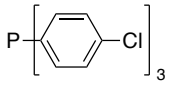	162	90	-0.29
		100	N.A.			100	-7.27
		110	(32.78)			110	-9.49
		120	14.95			120	-8.39
		140	-2.71			140	-5.35
		180	-3.15			180	-2.24
$P(CF_3)_3$	137	90	17.60	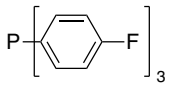	163	90	2.12
		100	4.08			100	-5.96
		110	-1.49			110	-8.18
		120	-2.68			120	-8.03
		140	-1.62			140	-4.89
		180	-0.88			180	-2.15
P^tBu_3	187	90	N.A.	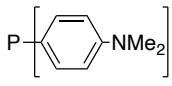	163	90	(80.03)
		100	N.A.			100	-5.44
		110	(57.27)			110	-8.60
		120	(34.67)			120	-10.04
		140	2.20			140	-5.63
		180	-4.77			180	-0.90

$E_{\mathrm{L-L}}$ values are reported in kcal/mol. N.A.: Not applied. $E_{\mathrm{L-L}}$ values larger than 30 kcal/mol are shown in parentheses but are ignored in the discussion below, as they are quite unrealistic.

Table S6. (continued)

ligand	θ (°)	ϕ (°)	E_{L-L}	ligand	θ (°)	ϕ (°)	E_{L-L}
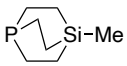	126	90	7.67	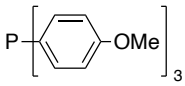	163	90	-1.30
		100	1.18			100	-6.15
		110	-0.42			110	-6.84
		120	-0.20			120	-11.15
		140	0.29			140	-5.66
		180	0.59			180	-1.75
PH_3	86	90	3.89	PPh_3	162	90	2.51
		100	1.77			100	-4.72
		110	0.93			110	-6.73
		120	0.59			120	-6.75
		140	0.42			140	-4.55
		180	0.40			180	-1.87
$P(SiH_3)_3$	126	90	8.49	$P(C_6F_5)_3$	191	90	(62.12)
		100	0.77			100	-13.20
		110	-1.66			110	-13.56
		120	-2.15			120	-15.65
		140	-1.00			140	-11.90
		180	-0.41			180	-7.63
$P(SiMe_3)_3$	182	90	N.A.	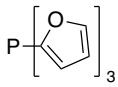	140	90	-0.50
		100	N.A.			100	-5.25
		110	24.47			110	-5.10
		120	9.32			120	-4.56
		140	-0.94			140	-1.34
		180	-3.64			180	-0.02
	113	90	7.21	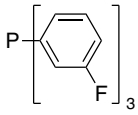	162	90	1.21
		100	0.34			100	-6.03
		110	-0.62			110	-7.96
		120	-0.43			120	-8.89
		140	-0.04			140	-5.84
		180	0.15			180	-2.12

E_{L-L} values are reported in kcal/mol. N.A.: Not applied. E_{L-L} values larger than 30 kcal/mol are shown in parentheses but are ignored in the discussion below, as they are quite unrealistic.

Table S6. (continued)

ligand	θ (°)	ϕ (°)	E_{L-L}	ligand	θ (°)	ϕ (°)	E_{L-L}
	103	90	0.57	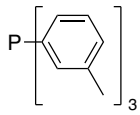	174	90	(65.53)
		100	-0.05			100	-8.82
		110	-0.20			110	-11.37
		120	-0.20			120	-10.73
		140	-0.09			140	-8.17
		180	0.05			180	-3.34
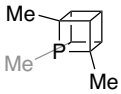	130	90	2.37				
		100	-1.74				
		110	-1.88				
		120	-1.67				
		140	-0.75				
		180	-0.16				

E_{L-L} values are reported in kcal/mol. N.A.: Not applied. E_{L-L} values larger than 30 kcal/mol are shown in parentheses but are ignored in the discussion below, as they are quite unrealistic.

4.2 Discussion

The calculated values of E_{L-L} were plotted against the cone angle (θ) of the ligands and bite angle (ϕ), as shown in Fig. S5a. We found that the trend of E_{L-L} cannot be described only by the θ and ϕ. For example, the E_{L-L} of $P(SiMe_3)_3$ at ϕ = 120° was 9.3 kcal/mol (repulsive), while the E_{L-L} of $P(C_6F_5)_3$, whose cone angle is slightly larger than that of $P(SiMe_3)_3$, was –13.6 kcal/mol (attractive) at the same bite angle. This is likely caused by the stabilization of the two molecules of $P(C_6F_5)_3$ through intermolecular π–π interactions, as shown in Fig. S5a (right). Considering these results, we classified ligands into two groups: triaryl phosphines (PAr_3) and others (PR_3, R≠Ar). The former group is expected to exhibit negative E_{L-L} values due to attractive π–π interactions when two ligands are located close together, while the latter group would exhibit positive E_{L-L} values due to the typical steric repulsion. This trend was confirmed by separately plotting the E_{L-L} values for each group (Fig. S5b). Specifically, the PR_3-type ligands showed a trend of E_{L-L} where combinations of a large cone angle (θ) and a small bite angle (ϕ) resulted in a large positive value of E_{L-L} (Fig. S5b, right). In contrast, the E_{L-L} values for triaryl phosphines (PAr_3) had a minimum around θ = 180° and ϕ = 120°, clearly showing the effect of stabilization through intermolecular π–π interactions (Fig. S5b, left). As a result, the V_{L-L} term of the cone potential of **VL2**, which describes the interactions of two virtual ligands, was separately optimized for each type of L-L interaction and implemented as $\mathbf{VL2_{PR3}}$ and $\mathbf{VL2_{PAr3}}$, respectively (Section 5.5 of the ESI).

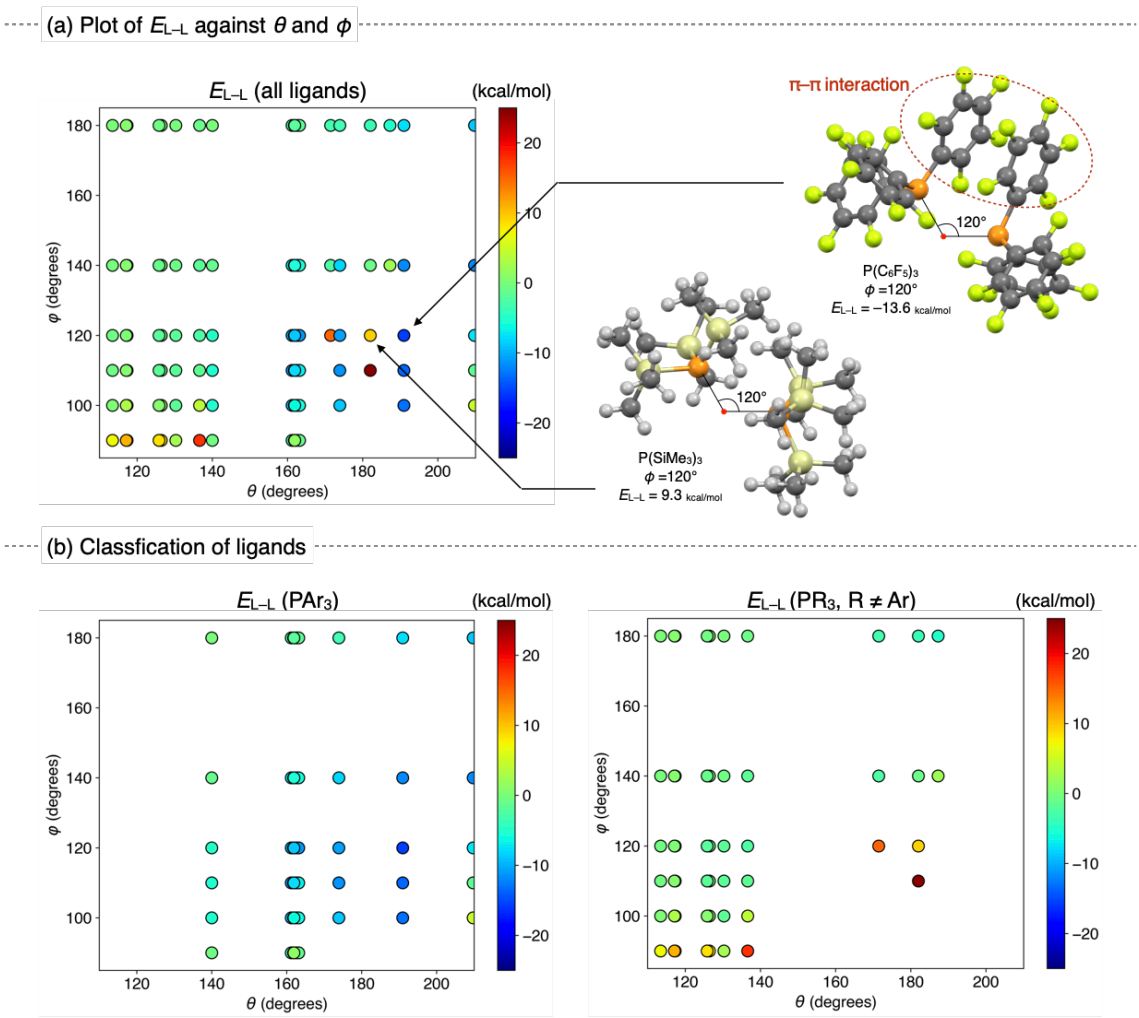

Fig. S5. Plot of the calculated E_{L-L} values against cone angle (θ) and bite angle (ϕ).

5. Implementation and performance of virtual ligands

5.1 General

In this study, virtual ligands were implemented in interface codes combining the GRRM program with Gaussian 16. During a geometry optimization process, Gaussian 16 performs an electronic structure calculation for a given geometry and sends the output, including energy, gradient vector, and Hessian matrix, to the GRRM software. The GRRM program then calculates a new geometry based on the given geometry, energy, gradient vector, and Hessian matrix, and sends it back to Gaussian 16. The virtual ligands were implemented by adding the energies, gradient vectors, and Hessian matrices resulting from the keep potential and either the cone potential (for the original version and **VL2**) or the 12-6 Lennard-Jones (LJ) potential (for **VL1**) to the Gaussian 16 output.

5.2 Implementation of keep potential

Using Cartesian coordinates of phosphorus atoms ($\boldsymbol{p} = (x_{\mathrm{P}}, y_{\mathrm{P}}, z_{\mathrm{P}})$) and chlorine atoms ($\boldsymbol{l_i} = (x_{\mathrm{Cl}-i}, y_{\mathrm{Cl}-i}, z_{\mathrm{Cl}-i})$, $i = 1-3$) in a virtual ligand, the energy arising from the keep potential can be formulated as follows:

$$V_{keep} = \sum_{i=1}^{3} \frac{1}{2} k (r_i - r_0)^2$$

$$r_i = |\boldsymbol{l_i} - \boldsymbol{p}|$$

where k, r_i, and r_0 are the force constant, the distance between the P and *i*th Cl atom, and the equilibrium distance of the harmonic potential, respectively. The force constant was set to 4.48×10^3 kcal/(mol Å^2) (2.0 a.u.). The gradient vector and Hessian matrix arising from the keep potential were calculated as partial derivatives.

The electronic effect of a real ligand can be simulated by adjusting the r_0 value to match the TEP value of the ligand calculated at the same computational level.[S9] The relationship between r_0 and TEP values of the virtual ligand is shown in Fig. S6.

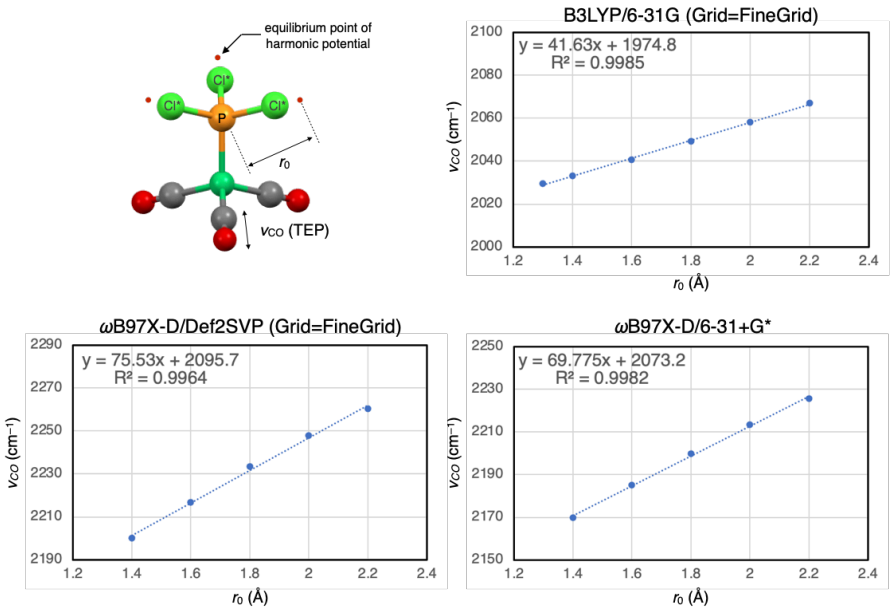

Fig. S6. Relationship between the r_0 and TEP value of the virtual ligand.

5.3 Implementation of VL1

The original virtual ligand used a cone potential to reproduce the steric effect of the real ligand (Fig. S7, left). The cone was positioned 2.28 Å from the phosphorus atom of PCl^*_3 and had an apex angle θ corresponding to the cone angle of the real ligands. The repulsion energy for each atom in the substrate was calculated based on the distance between the atom and the surface of the cone. The repulsive term of the optimized 12-6 LJ potential was used as the potential function. While the cone potential accurately captured the relationship between the cone angles and steric effects of real ligands, we identified a weakness in its design. The position of the apex, apex angle, and direction of the cone are uniquely defined by PCl^*_3 and the cone angle. However, the length of the cone (L in Fig. S7, left panel) is not fixed (it is treated as infinite). As a result, even if a substrate is located far from the virtual ligand (e.g., **1** in Fig. S7, left panel), the corresponding repulsion energy is still calculated, leading to an overestimation of the steric repulsion. Moreover, if a substrate is placed on the back of PCl^*_3 (e.g., **2**), an unrealistic, large repulsive energy is exerted. These incidents would not normally occur in typical quantum chemical calculations, such as geometry optimizations, unless there are "unnatural" forces working against the repulsive force from the cone exist. However, in the case of automated reaction path search calculations using the SC–AFIR method,[S3] where "artificial" forces are used to explore accessible minima and TSs from a given initial structure as much as possible, these situations could occur due to the rotation or flipping of the virtual ligand. To address this issue, we developed an alternative method for reproducing the steric effect of real ligands that is more robust in these types of calculations (Fig. S7, right panel). In this method, the steric effect of a real ligand is simulated using a simple 12-6 LJ potential between the substrate and Cl* atoms in the virtual ligand. The parameters for the 12-6 LJ potential were adopted from the values reported for the universal force field (UFF).[S18]

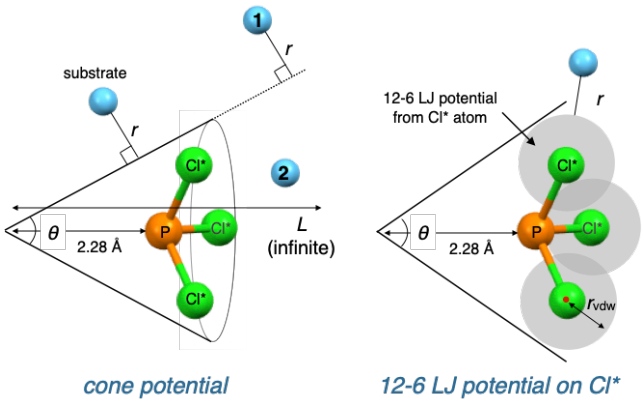

Fig. S7. Schematic illustration of the cone potential (left) and the newly developed steric approximation using 12-6 LJ potential form Cl* atoms (right).

In this method, the cone angle of a real ligand can be simulated by scaling the parameter of the 12-6 LJ potential based on the van der Waals radii of the Cl* atoms. Particularly, for a given geometry of PCl^*_3, the cone angle of the virtual ligand (θ) can be geometrically calculated as follows:

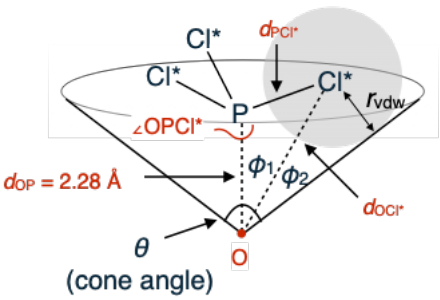

$$\theta = 2(\phi_1 + \phi_2)$$

$$\phi_1 = \arctan\left[\frac{d_{PCl^*}\sin(\pi - \angle OPCl^*)}{d_{OP} + d_{PCl^*}\cos(\pi - \angle OPCl^*)}\right]$$

$$\phi_2 = \arcsin\left(\frac{r_{vdw}}{d_{OCl^*}}\right)$$

$$d_{OCl^*} = \frac{d_{OP} + d_{PCl^*}\cos(\pi - \angle OPCl^*)}{\cos\phi_1}$$

where d_{OP}, d_{PCl^*}, and d_{OCl^*} are the distances between the apex of the cone and the P atom, the P atom and the Cl* atom, and the apex of the cone and the Cl* atom, respectively; $\angle OPCl^*$ is the angle defined by the apex, the P atom, and the Cl* atom, and r_{vdw} is the van der Waals radius of the Cl* atom. The position of apex (O) was set to be 2.28 Å from the P atom, following the definition of the cone angle.[S8] Since the values of d_{PCl^*}, and $\angle OPCl^*$ change depending on the r_0 value of the keep potential (see section 5.2 of the ESI), representative values were obtained from the optimized structure of $(Cl^*_3P)Ni(CO)_3$, as presented in Tables S7 and S8. The r_0 and r_{vdw} values used to reproduce the electronic and steric effects of PPh_3 are listed in Table S7. For example, the TEP (ν_{CO}) of PPh_3 was estimated to be 2027.7 cm^{-1} at the B3LYP/6-31G level, and the r_0 to reproduce this value was calculated to be 1.3 Å based on Fig. S6. The d_{PCl^*} and $\angle OPCl^*$ values were extracted from the optimized structure of $(Cl^*_3P)Ni(CO)_3$ (r_0 = 1.3 Å), and the r_{vdw} value to reproduce the steric effect of PPh_3 (θ = 165°) was calculated to be 2.51 Å according to the equations above. Similarly, the r_0 and r_{vdw} values for reproducing PPh_3 at the ωB97X-D/def2-SVP level (ν_{CO} = 2220.8 cm^{-1} and θ = 165°) were estimated to be 1.657 and 2.71 Å, respectively. The r_0 and r_{vdw} values (Table S7) were used in the automated reaction path search calculation using the SC-AFIR method or the following path refinement using the LUP method at the corresponding computational level. In contrast, in Table S8, the r_0 and r_{vdw} values corresponding to the grid points of the TEP and cone angle at the ωB97X-D/6-31+G(d) level were listed. These values were not used in the manuscript but in Section 5.4 of the ESI to confirm the accuracy of this steric approximation used in **VL1**.

Table S7. The r_0 and r_{vdw} values to reproduce electronic and steric effects of PPh_3.

	r_0 (Å)	d_{PCl^*} (Å)	$\angle OPCl^*$ (°)	r_{vdw} (Å) θ = 165° (PPh_3)	Usage
B3LYP/6-31G	1.3	1.53	106.7	2.51	SC-AFIR
ωB97X-D/def2-SVP	1.657	1.73	112.6	2.71	LUP

Table S8. The r_0 and r_{vdw} values to perform a grid search of electronic and steric parameters (TEP and cone angle) at the ωB97X-D/6-31+G(d) level.

r_0 (Å)	$d_{\mathrm{PCl^*}}$ (Å)	∠OPCl* (°)	r_{vdw} (Å)				
			θ = 120°	θ = 140°	θ = 160°	θ = 180°	θ = 200°
1.4	1.56	108.6	1.67	2.10	2.48	2.78	2.99
1.6	1.69	111.4	1.72	2.18	2.58	2.90	3.13
1.8	1.84	114.2	1.79	2.28	2.70	3.03	3.28
2.0	2.01	116.7	1.86	2.38	2.82	3.18	3.45
2.2	2.19	118.6	1.92	2.47	2.94	3.33	3.61

The parameters of the 12-6 LJ potential were scaled based on the determined van der Waals radii of the Cl* atoms. In the framework of the UFF, the nonbonding energy based on the 12-6 LJ potential is described as:

$$E_{\mathrm{vdw}} = \varepsilon_{ij}\left[\left(\frac{\sigma_{ij}}{r}\right)^{12} - 2\left(\frac{\sigma_{ij}}{r}\right)^{6}\right]$$

$$\varepsilon_{ij} = \sqrt{\varepsilon_i \varepsilon_j}$$

$$\sigma_{ij} = \sqrt{\sigma_i \sigma_j}$$

where the ε_{ij}, σ_{ij} and r are the wall depth, van der Waals bond length, and distance between two atoms, respectively; the ε_i is the atomic van der Waals energy; and the σ_i is the van der Waals distance. Therefore, the steric interactions between the substrates and the Cl* atoms in **VL1** can be described using the following equation:

$$V_{\mathrm{L\text{-}S}} = \sum_{i\in \mathrm{S}}\sum_{j=1}^{3}\sqrt{\varepsilon_i \varepsilon_{\mathrm{Cl}}}\left[\left(\frac{\sqrt{\sigma_i \sigma_{\mathrm{Cl}}}}{r_{ij}}\right)^{12} - 2\left(\frac{\sqrt{\sigma_i \sigma_{\mathrm{Cl}}}}{r_{ij}}\right)^{6}\right]$$

where the r_{ij} is the distance between *i*th atom in the substrate (S) and *j*th Cl* atom in **VL1**. To change the van der Waals radii of the Cl* atom, the parameter σ_{Cl} was scaled by the ratio of the r_{vdw} required to reproduce the desired cone angle (Tables S7 and S8) to the original van der Waals radius of the Cl atom (1.75 Å).

5.4 Performance of VL1

The performance of the virtual ligand **VL1** was validated computationally and compared with that of the original virtual ligand.[S19] Contour maps indicating the activation energy ($\Delta E^{\ddagger}$) or the reaction energy (ΔE) of an intramolecular C–H activation from the aryl palladium **S1** were prepared using either the original virtual ligand or **VL1** (Fig. S8), following a previously reported procedure.[S19] The calculated values of $\Delta E^{\ddagger}$ and ΔE using real ligands (also reported in a previous study) were plotted on the corresponding contour maps (circles). Additionally, the values of $\Delta E^{\ddagger}$ and ΔE were predicted based on their TEP values and cone angles. The predicted values ($\Delta E^{\ddagger}_{\mathrm{virtual}}$ and $\Delta E_{\mathrm{virtual}}$) are plotted against the calculated values ($\Delta E^{\ddagger}_{\mathrm{real}}$ and ΔE_{real}), as shown on the right side of Fig. S8. For $\Delta E^{\ddagger}$, **VL1** (represented by orange dots) provided predictions of lower accuracy compared to the original virtual ligand (represented by blue dots). The mean absolute errors (MAE) for $\Delta E^{\ddagger}$ were estimated to be 4.32 kcal/mol for the prediction by **VL1**, and 2.46 kcal/mol for the prediction based on the original

virtual ligand. However, qualitative correlations between predicted and calculated values of $\Delta E^{\ddagger}$ were still high, and the coefficient of determination (R^2) of the regression line (orange dotted line) was 0.74 (0.75 for the original virtual ligand, blue dotted line). In contrast, the prediction accuracy for ΔE was improved by **VL1**, where the MAE was 1.43 kcal/mol for **VL1** and 2.15 kcal/mol for the original virtual ligand. Although **VL1** resulted in a slightly worse performance for the prediction of $\Delta E^{\ddagger}$, the problems derived from the cone potential (described in Section 5.3 of the ESI) can be mitigated. Therefore, we used **VL1** for the automated reaction path search calculations using the SC-AFIR method and the following path refinement calculations using the locally updated planes (LUP) method.

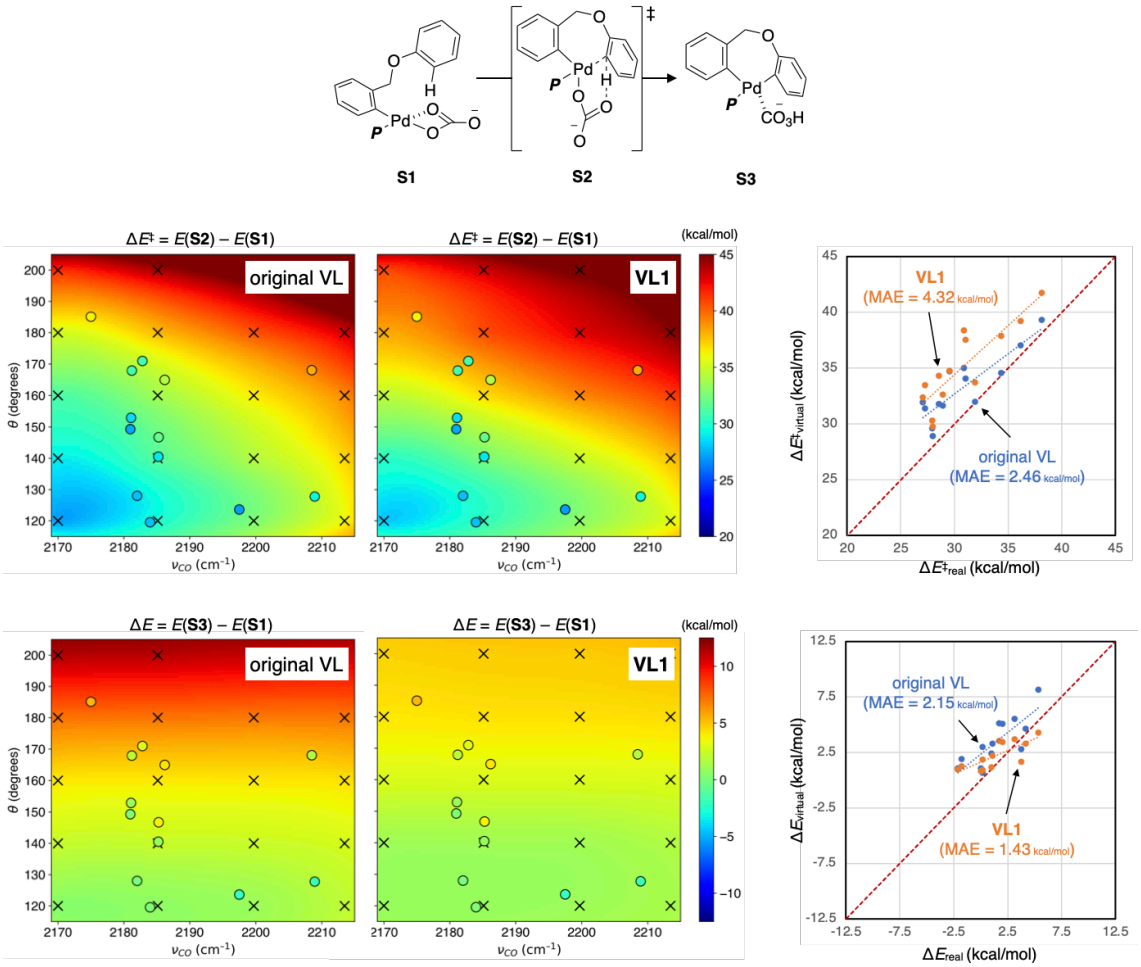

Fig. S8. Comparison of the performance between the original virtual ligand and the **VL1**.

5.5 Implementation of VL2$_{PR3}$ and VL2$_{PAr3}$

In the parameter screening step of the VLA screening, we employed a modified version of the cone potential for steric approximation to improve accuracy. In the original version, the interactions between the virtual ligand and the substrates (L-S interactions) were described only by the repulsive term of the 12-6 LJ potential. In the modified version, the full 12-6 LJ potential, including the attractive term, is used as a potential function. The modified version of the cone potential can be formulated as follows. First, the energy arising from the cone potential is described as the sum of the L-S interaction energies (V_{L-S}) and L-L interaction energies ($V_{\mathrm{L-L}}$). The apex of the cone is located 2.28 Å from the phosphorus atom of PCl*$_3$, and its direction should be the same as that of the lone pair orbital of the phosphorus atom. Therefore, the coordinates of the apex ($\boldsymbol{a} = (x_{\mathrm{a}}, y_{\mathrm{a}}, z_{\mathrm{a}})$) can be defined as:

$$\boldsymbol{a} = \boldsymbol{p} - 2.28\ (\text{Å}) \cdot \frac{(\boldsymbol{l_1} - \boldsymbol{p}) + (\boldsymbol{l_2} - \boldsymbol{p}) + (\boldsymbol{l_3} - \boldsymbol{p})}{|(\boldsymbol{l_1} - \boldsymbol{p}) + (\boldsymbol{l_2} - \boldsymbol{p}) + (\boldsymbol{l_3} - \boldsymbol{p})|}$$

$$= \boldsymbol{p} - 2.28\ (\text{Å}) \cdot \frac{\boldsymbol{l_1} + \boldsymbol{l_2} + \boldsymbol{l_3} - 3\boldsymbol{p}}{|\boldsymbol{l_1} + \boldsymbol{l_2} + \boldsymbol{l_3} - 3\boldsymbol{p}|}$$

where $\boldsymbol{p}$ and $\boldsymbol{l_i}$ (i = 1–3) are the Cartesian coordinates of the phosphorus and chlorine atoms in the virtual ligands, respectively. Using the Cartesian coordinates of the ith atom in substrate S ($\boldsymbol{i} = (x_i, y_i, z_i)$, $i \in$ S), the V_{L-S} can be calculated as:

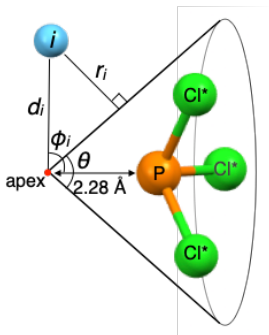

$$V_{L-S} = \sum_{i \in \mathrm{S}} 4\varepsilon \left[\left(\frac{\sigma}{r_i + a\sigma} \right)^{12} - \left(\frac{\sigma}{r_i + a\sigma} \right)^{6} \right]$$

$$r_i = \begin{cases} d_i \sin\left(\phi_i - \frac{\theta}{2}\right) & \left(\phi_i - \frac{\theta}{2} \leq \frac{\pi}{2}\right) \\ d_i & \left(\phi_i - \frac{\theta}{2} > \frac{\pi}{2}\right) \end{cases}$$

$$d_i = |\boldsymbol{i} - \boldsymbol{a}|$$

$$\phi_i = \arccos\left(\frac{(\boldsymbol{p} - \boldsymbol{a}) \cdot (\boldsymbol{i} - \boldsymbol{a})}{|\boldsymbol{p} - \boldsymbol{a}||\boldsymbol{i} - \boldsymbol{a}|} \right)$$

where θ denotes the apex angle of the cone potential (cone angle). The constants ε, σ, and a were determined based on He$_8$_steric and related steric descriptors. He$_8$_steric, which was proposed by Fey *et al.*,[S20] is defined by the interaction energy (E_{ster}) between a phosphorus(III) ligand and a ring of eight helium atoms. The helium atoms were arranged in regular positions in a circle with a radius of 2.5 Å, while the phosphorus atom in the ligand was fixed at a distance of 2.28 Å from the center of the ring (Fig. S9a, l = 2.28 Å). Previous research by Fey *et. al.*,[S20] used the BP86 functional, which does not include dispersion term. In this study, we calculated the He$_8$_steric of 30 phosphine ligands using the ωB97X-D functional (the ωB97X-D/def2-SV(P) level), which includes dispersion term, to properly evaluate the attractive steric effect of the real ligands. Additionally, we calculated related steric descriptors, in which the phosphorus atom in each ligand was fixed at 2.78 or 3.28 Å (Fig. S9a, l = 2.78 or 3.28 Å) from the center of the ring. The calculated values for each ligand correlated well with the cone angle, as shown in Fig. S9c (left, dots). In contrast, the interaction energy (E_{ster}) between a virtual ligand and a ring of eight helium atoms can be numerically calculated, as shown in Fig. S9b. The constants ε, σ, and a were optimized using a grid search,

such that the relationship between E_{ster} and θ of the cone potential (Fig. S9b) reproduced the correlation between E_{ster} and θ in real systems (Fig. S9c, left). The grid search was performed with ε values in the range of 0–10 kcal/mol with 0.01 kcal/mol step width, σ values in the range of 0–20 Å with 0.01 Å step width, and a values in the range of 0–2 with 0.01 step width. The optimal values for ε, σ, and a were 0.41 kcal/mol, 13.84 Å, and 0.93, respectively. The plot of E_{ster} against θ for the cone potential with these optimal constants is shown in Fig. S9c (left, solid lines). The calculated values of E_{ster} for real ligands and the values predicted by the optimized cone potential exhibited a strong correlation with a coefficient of determination (R^2) of 0.84 (Fig. S9c, right). The structures of the real ligands and the calculated values of E_{ster} are listed in Table S9.

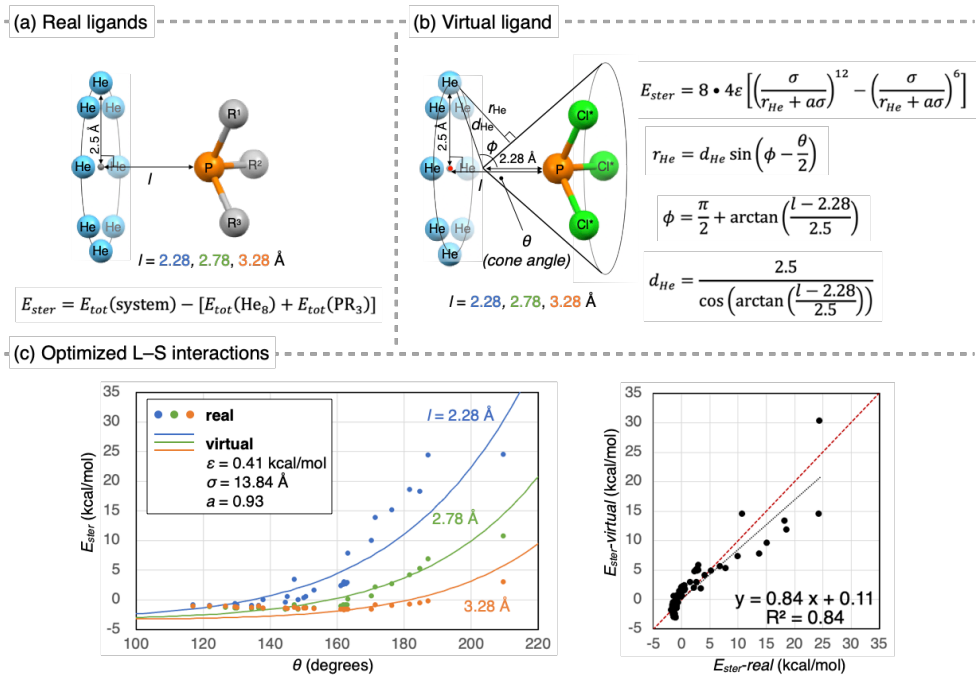

Fig. S9. He_8_steric and related steric descriptors. (a) Definition of descriptors for real ligands. (b) Expected steric interactions between the He_8 ring and the cone potential. (c) Comparison between real and optimized virtual systems.

Table S9. Cone angle and calculated interaction energies (E_{ster}) for real ligands.

Ligand	θ (degrees)	E_{ster} (kcal/mol)		
		l = 2.28 Å	l = 2.78 Å	l = 3.28 Å
PMe_3	117	-0.8	-1.1	-1.1
PEt_3	150	0.3	-1.4	-1.4
$P(CF_3)_3$	137	-1.0	-1.4	-1.1
$P(CCl_3)_3$	171	13.8	2.2	-0.9
PPh_3	162	2.7	-0.9	-1.6
P^tBu_3	187	24.3	6.9	-0.2
$P(p\text{-}OMeC_6H_4)_3$	163	2.8	-0.8	-1.6
$P(p\text{-}NMe_2C_6H_4)_3$	163	2.8	-0.8	-1.6
$P(p\text{-}FC_6H_4)_3$	163	2.7	-0.9	-1.6
$P(p\text{-}ClC_6H_4)_3$	162	2.5	-1.0	-1.6
$P(p\text{-}CF_3C_6H_4)_3$	161	2.3	-1.0	-1.6
$P(o\text{-tol})_3$	210	24.4	10.7	3.0
$PMe(CCl_3)_2$	147	3.4	-0.8	-1.3
$PMe(CF_3)_2$	127	-1.1	-1.3	-1.1
$PMe_2(CCl_3)$	130	-0.7	-1.4	-1.2
$PMe_2(CF_3)$	122	-1.0	-1.2	-1.1
PMe_2Ph	130	-0.9	-1.4	-1.3
$PMe_2{}^tBu$	138	0.0	-1.6	-1.4
$PMe(Ph)(CF_3)$	135	-0.9	-1.5	-1.3
$PMePh_2$	145	-0.4	-1.6	-1.4
$PMe({}^tBu)(CF_3)$	145	0.6	-1.5	-1.5
$PMe{}^tBu_2$	163	7.8	0.1	-1.6
$PPh(CF_3)_2$	151	0.6	-1.3	-1.4
$PPh_2(CF_3)$	149	-0.1	-1.6	-1.5
$P^tBu(CCl_3)_2$	176	15.1	2.6	-1.0
$P^tBu(CF_3)_2$	153	1.6	-1.5	-1.5
P^tBuPh_2	162	3.0	-1.4	-1.8
$P^tBu_2(CCl_3)$	182	18.6	4.1	-0.8
$P^tBu_2(CF_3)$	170	10.0	0.7	-1.6
P^tBu_2Ph	185	18.2	5.2	-0.6

The $V_{\mathrm{L-L}}$ term, which describes L-L interactions, was also modified. To describe L-L interactions, the interaction between two virtual ligands must be considered (Fig. S10, top). However, this interaction is more complex to implement compared to the L-S interaction because it depends on the distance between the ligands and their relative orientation. To simplify the modeling of the L-L interaction in the cone potential, we considered the interaction between one cone (e.g., a cone containing a P_i atom) and the phosphorus atom of another virtual ligand (P_j) rather than considering two cones (Fig. S10, bottom). As P_j is located inside the cone, which is subjected to the L-L interaction, this evaluation underestimates the strength of the L-L interaction. To address this systematic error in the original version of the cone potential, a larger cone with an apex angle of 1.7θ (where θ is the apex angle of the original cone) was defined (dotted line, Fig. S10, bottom left). The larger cone shared the same apex and axis as the original cone. The L-L interaction was estimated using the distance between a phosphorus atom and the newly defined cone (r_{ij}' and r_{ji}') under the potential function optimized for the L-S interaction. In the modified version of the cone potential, a new potential function was prepared to more accurately describe the L-L interactions of real ligands (Fig. S10, bottom right). This new potential function was used to estimate the L-L interactions using the distance between a phosphorus atom and the original cone (r_{ij} and r_{ji}), rather than attempting to correct the systematic error through modification of the cone angle. The 12-6 LJ potential was used as the potential function for the L-L interactions.

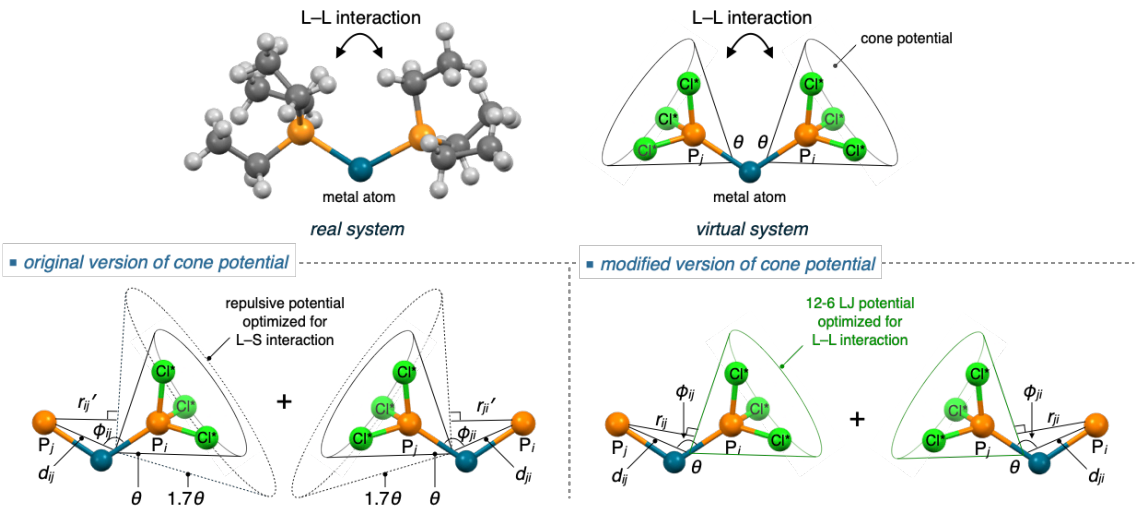

Fig. S10. Approximation of ligand-ligand (L-L) interactions. Interaction between two real ligands (top left), interaction between two virtual ligands (top right), simplified model in the original version (bottom left), and the modified version (bottom right) of the cone potential.

The $V_{\mathrm{L-L}}$ term of the modified cone potential can be calculated as follows:

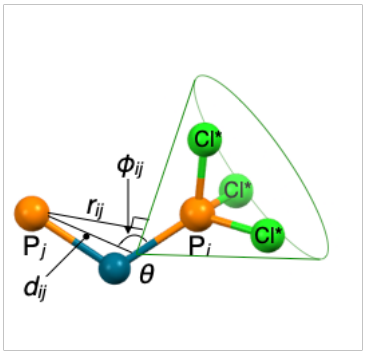

$$V_{\mathrm{L-L}} = \sum_{i \in \mathrm{P_{virt}}} \sum_{j \in \mathrm{P_{virt}}, i \neq j} \frac{1}{2} \bullet 4\varepsilon' \left[\left(\frac{\sigma'}{r_{ij} + a'\sigma'} \right)^{12} - \left(\frac{\sigma'}{r_{ij} + a'\sigma'} \right)^{6} \right]$$

$$r_{ij} = \begin{cases} d_{ij} \sin\left(\phi_{ij} - \frac{\theta}{2}\right) & \left(\phi_{ij} - \frac{\theta}{2} \leq \frac{\pi}{2}\right) \\ d_{ij} & \left(\phi_{ij} - \frac{\theta}{2} > \frac{\pi}{2}\right) \end{cases}$$

$$d_{ij} = |\boldsymbol{p_j} - \boldsymbol{a_i}|$$

$$\phi_{ij} = \arccos\left(\frac{(\boldsymbol{p_i} - \boldsymbol{a_i}) \cdot (\boldsymbol{p_j} - \boldsymbol{a_i})}{|\boldsymbol{p_i} - \boldsymbol{a_i}||\boldsymbol{p_j} - \boldsymbol{a_i}|} \right)$$

where θ is the apex angle of the cone potential (cone angle), $\boldsymbol{p_i}$ is the Cartesian coordinate of the phosphorus atom in the *i*th virtual ligand, and $\boldsymbol{a_i}$ is the Cartesian coordinate of the cone apex for the *i*th virtual ligand. The constants ε', σ', and a' were determined based on the L-L interactions of the real ligands sampled in Section 4 of the ESI (Table S6). To optimize the constants ε', σ', and a' in the new potential function for the L-L interaction, the interaction energy between two virtual ligands ($E_{\mathrm{L\text{-}L}}$) in a geometry given in Fig. S4a was numerically calculated, as shown in Fig. S11a. We performed a grid search to determine the values for these constants that reproduced the observed correlation between $E_{\mathrm{L\text{-}L}}$, θ and ϕ in real systems (Fig. S5). A grid search was performed for ε' values in the range of 0–10 kcal/mol with 0.01 kcal/mol step width, for σ' values in the range of 0-20 Å with 0.01 Å step width, and for a' values in the range of 0–2 with 0.01 step width. The optimal values of the constants ε' σ', and a' were 0.81 kcal/mol, 5.56 Å, and 0.69 for the L–L interactions of PR_3, and 7.4 kcal/mol, 7.82 Å, and 0.99 for the L-L interactions of PAr_3, respectively. Fig. S11b shows the plots of $E_{\mathrm{L\text{-}L}}$ against θ and ϕ with optimal constants.

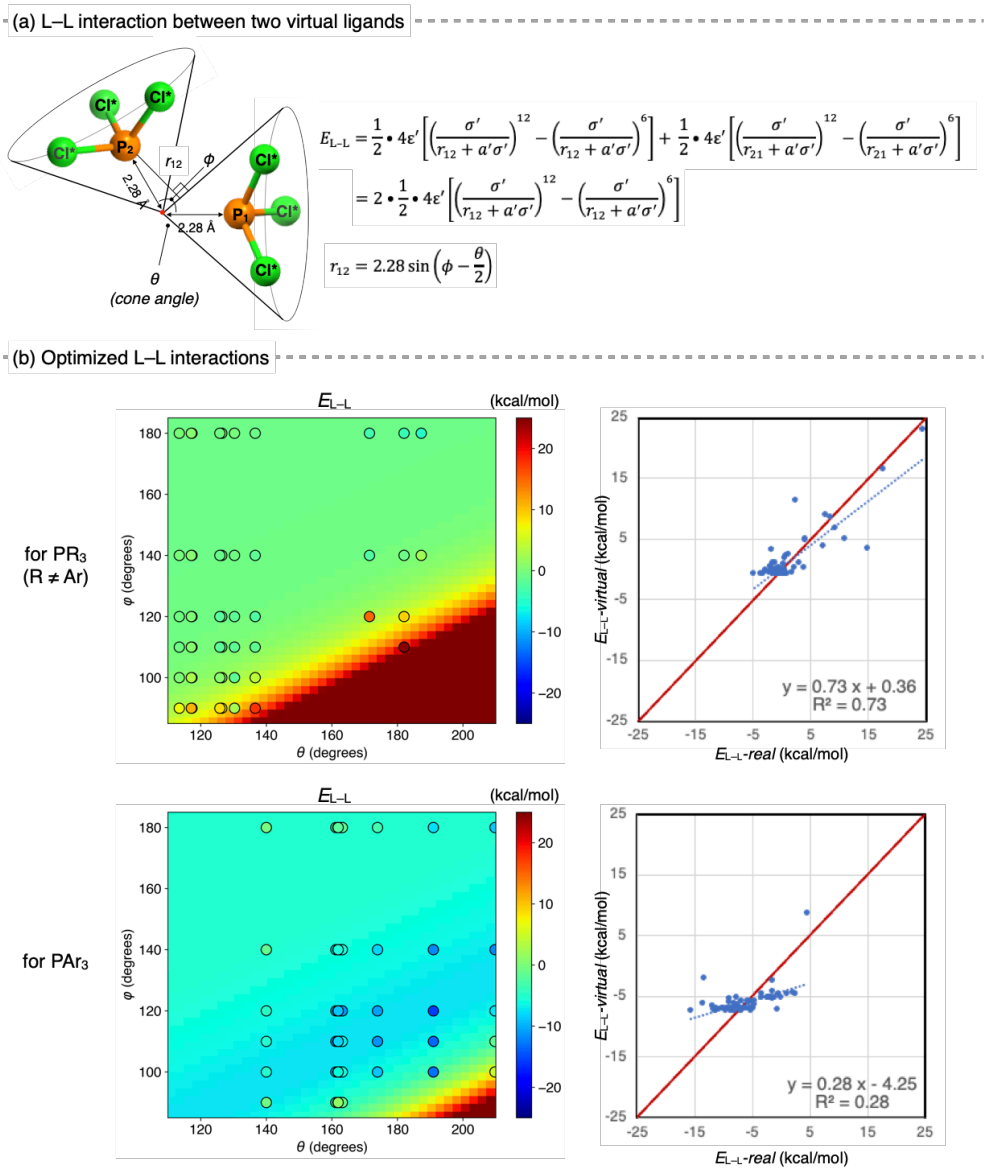

Fig. S11. Optimization of the 12-6 LJ potential for ligand-ligand (L-L) interactions. (a) Expected interaction energies between two virtual ligands in a given geometry. (b) Comparison between real and optimized virtual systems.

The energy arising from the cone potential was calculated as the sum of the energies described by the optimized V_{L-S} and $V_{\mathrm{L-L}}$ potentials. The gradient vector and Hessian matrix arising from the cone potential were calculated as partial derivatives.

5.6 Performance of VL2$_{PR3}$ and VL2$_{PAr3}$

The performance of the newly developed virtual ligands **VL2$_{PR3}$** and **VL2$_{PAr3}$** was validated computationally and compared with the original virtual ligand.[S19] Contour maps, which indicate the activation energy ($\Delta E^{\ddagger}$) or the reaction energy (ΔE) of an intramolecular C-H activation from the aryl palladium **S1**, were prepared using either the original virtual ligand or **VL2$_{PR3}$** (Fig. S12), following a previously reported procedure[S19]. The calculated values of $\Delta E^{\ddagger}$ and ΔE using real ligands (also reported in a previous study) were plotted on the corresponding contour maps (circles). The values of $\Delta E^{\ddagger}$ and ΔE were then predicted based on their TEP values and cone angles. The predicted values ($\Delta E^{\ddagger}_{virtual}$ and $\Delta E_{virtual}$) are plotted against the calculated values ($\Delta E^{\ddagger}_{real}$ and ΔE_{real}), as shown on the right side of Fig. S12. For $\Delta E^{\ddagger}$ and ΔE, the values predicted using the contour map prepared by **VL2$_{PR3}$** (shown by orange dots) were closer to the calculated values using real ligands compared to the values predicted by the original virtual ligand (shown by blue dots). The mean absolute errors (MAE) for $\Delta E^{\ddagger}$ and ΔE were 1.79 and 1.21 kcal/mol for values predicted based on **VL2$_{PR3}$**, and 2.46 and 2.15 kcal/mol for ones based on the original virtual ligand, indicating a significant improvement in the prediction performance. The prediction using **VL2$_{PAr3}$** should give the same results as **VL2$_{PR3}$** because only one virtual ligand exists in the system and **VL2$_{PAr3}$** is essentially identical to **VL2$_{PR3}$**, except for the description of L-L interactions.

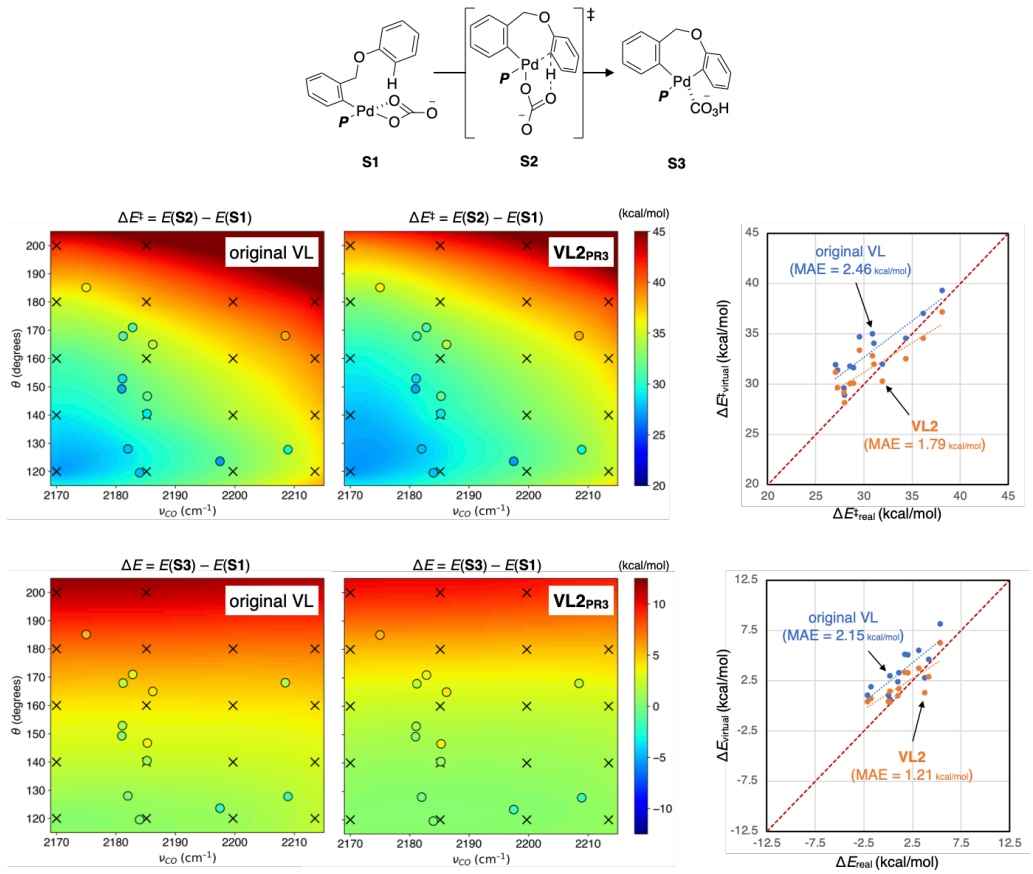

Fig. S12. Comparison of the performance between the original virtual ligand and the **VL2**.

To further verify the prediction abilities of **VL2**, the insertion of ethylene from rhodium complex **S4** was also calculated. According to a previously reported procedure,[S19] contour maps were generated to show the $\Delta E^{\ddagger}$ and ΔE of the reaction. In this case, three types of virtual ligands were used (the original version, **VL2$_{PR3}$**, and **VL2$_{PAr3}$**), and six contour maps were prepared. The calculated values of $\Delta E^{\ddagger}$ and ΔE using real ligands (reported in a previous report) were plotted on the contour maps (circles). While all ligands were uniformly plotted on the contour maps prepared by the original version of the virtual ligand, for the contour maps prepared by **VL2$_{PR3}$** and **VL2$_{PAr3}$**, each ligand was classified as PR_3-type or PAr_3-type based on its chemical structure and plotted on the corresponding contour maps. Fig. S13 (right side) shows the plot of the predicted energies ($\Delta E^{\ddagger}_{virtual}$ and $\Delta E_{virtual}$) against the calculated values ($\Delta E^{\ddagger}_{real}$ and ΔE_{real}). The values predicted by **VL2$_{PR3}$** and **VL2$_{PAr3}$** were combined and indicated as **VL2** (orange dots). For the prediction of $\Delta E^{\ddagger}$, the MAEs were 0.82 kcal/mol for the original version and 0.85 kcal/mol for **VL2**, indicating excellent prediction performance in both cases. However, the prediction performance of **VL2** for ΔE was significantly better than that of the original version, with MAEs of 2.57 kcal/mol for the original version and 2.07 kcal/mol for **VL2**.

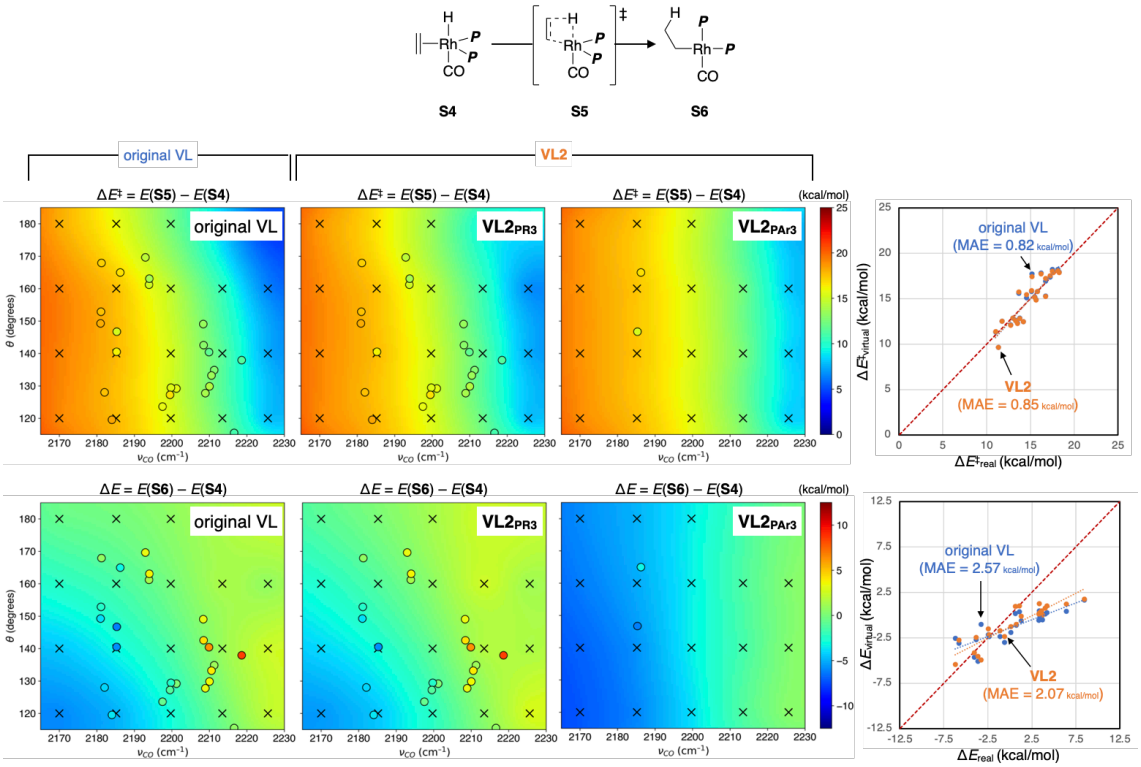

Fig. S13. Comparison of the performance between the original virtual ligand and the **VL2** in the insertion of ethylene from Rh complex **S4**.

Based on these results (Figs. S12 and S13), we concluded that the modified version of the virtual ligands **VL2$_{PR3}$** and **VL2$_{PAr}$** would be more accurate for describing phosphine ligands compared to the original version of the virtual ligand. This is likely due to the improved descriptions of attractive L-S interactions and the optimized potential functions for L-L interactions in the modified version.

6. Supplemental references

S1. Gaussian 16, Revision C.01, M. J. Frisch, G. W. Trucks, H. B. Schlegel, G. E. Scuseria, M. A. Robb, J. R. Cheeseman, G. Scalmani, V. Barone, G. A. Petersson, H. Nakatsuji, X. Li, M. Caricato, A. V. Marenich, J. Bloino, B. G. Janesko, R. Gomperts, B. Mennucci, H. P. Hratchian, J. V. Ortiz, A. F. Izmaylov, J. L. Sonnenberg, D. Williams-Young, F. Ding, F. Lipparini, F. Egidi, J. Goings, B. Peng, A. Petrone, T. Henderson, D. Ranasinghe, V. G. Zakrzewski, J. Gao, N. Rega, G. Zheng, W. Liang, M. Hada, M. Ehara, K. Toyota, R. Fukuda, J. Hasegawa, M. Ishida, T. Nakajima, Y. Honda, O. Kitao, H. Nakai, T. Vreven, K. Throssell, J. A. Montgomery, Jr., J. E. Peralta, F. Ogliaro, M. J. Bearpark, J. J. Heyd, E. N. Brothers, K. N. Kudin, V. N. Staroverov, T. A. Keith, R. Kobayashi, J. Normand, K. Raghavachari, A. P. Rendell, J. C. Burant, S. S. Iyengar, J. Tomasi, M. Cossi, J. M. Millam, M. Klene, C. Adamo, R. Cammi, J. W. Ochterski, R. L. Martin, K. Morokuma, O. Farkas, J. B. Foresman and D. J. Fox, Gaussian, Inc., Wallingford CT, 2016.

S2. F. Neese, F. Wennmohs, U. Becker and C. Riplinger, *J. Chem. Phys.*, 2020, **152**, 224108.

S3. S. Maeda, Y. Harabuchi, M. Takagi, K. Saita, K. Suzuki, T. Ichino, Y. Sumiya, K. Sugiyama and Y. Ono, *J. Comput. Chem.*, 2018, **39**, 233–250.

S4. R. F. Ribeiro, A. V. Marenich, C. J. Cramer and D. G. Truhlar, *J. Phys. Chem. B*, 2011, **115**, 14556–14562.

S5. R. L. Martin, P. J. Hay and L. R. Pratt, *J. Phys. Chem. A*, 1998, **102**, 3565–3573.

S6. For selected examples, see: (a) Y. Liu, Y. Tang, Y.-Y. Jiang, X. Zhang, P. Li and S. Bi, *ACS Catal.*, 2017, **7**, 1886–1896; (b) P.-P. Chen, E. L. Lucas, M. A. Greene, S.-Q. Zhang, E. J. Tollefson, L. W. Erickson, B. L. H. Taylor, E. R. Jarvo and X. Hong, *J. Am. Chem. Soc.*, 2019, **141**, 5835–5855.

S7. (a) S. Grimme, C. Bannwarth and P. Shushkov, J. *Chem. Theory Comput.*, 2017, **13**, 1989–2009; (b) D. Grimme and C. Bannwarth, *J. Chem. Phys.*, 2016, **145**, 054103.

S8. C. A. Tolman, *Chem. Rev.*, 1977, **77**, 313–348.

S9. L. Perrin, E. Clot, O. Eisenstein, J. Loch and R. H. Crabtree, *Inorg. Chem.*, 2001, **40**, 5806–5811.

S10. T. Gensch, G. dos Passos Gomes, P. Friederich, E. Peters, T. Gaudin, R. Pollice, K. Jorner, A. Nigam, M. Lindner-D'Addario, M. S. Sigman and A. Aspuru-Guzik, *J. Am. Chem. Soc.*, 2022, **144**, 1205–1217.

S11. C. Choi and R. Elber, *J. Chem. Phys.*, 1991, **94**, 751–760.

S12. Y. Sumiya and S. Maeda, *Chem. Lett.*, 2020, **49**, 553–564.

S13. Y. Sumiya and S. Maeda, *Chem. Lett.*, 2019, **48**, 47–50.

S14. A. V. Marenich, C. J. Cramer and D. G. Truhlar, *J. Phys. Chem. B*, 2009, **113**, 6378–6396.

S15. L. J. Gooßen, P. P. Lange, N. Rodríguez and D. Linder, *Chem.–Eur. J.*, 2010, **16**, 3906–3909.

S16. L. Chen, P. Ren and B. P. Carrow, *J. Am. Chem. Soc.*, 2016, **138**, 6392–6395.

S17. F. Rampf and H.-C. Militzer, EP1354886A1, October 22, 2003.

S18. A. K. Rappé, C. J. Casewit, K. S. Colwell and W. M. Skiff, *J. Am. Chem. Soc.*, 1992, **114**, 10024–10035.

S19. W. Matsuoka, Y. Harabuchi and S. Maeda, *ACS Catal.*, 2022, **12**, 3752–3766.

S20. N. Fey, A. C. Tsipis, S. E. Harris, J. N. Harvey, A. G. Orpen and R. A. Mansson, *Chem.–Eur. J.*, 2006, **12**, 291–302.

7. GC spectra

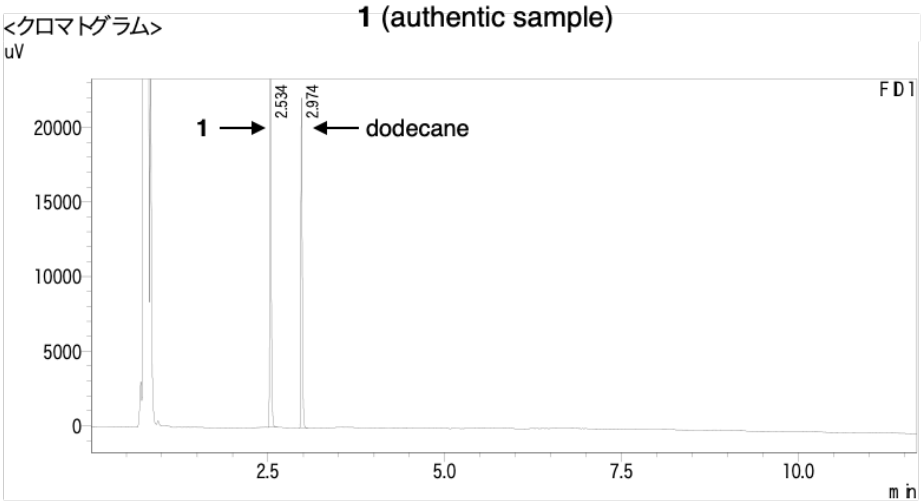

<ピークレポート>

FD1	Ret. Time	Area	Height				
ピーク#	保持時間	面積	高さ	濃度	単位	マーク	化合物名
1	2.534	37377	27055	0.000			
2	2.974	30049	21070	0.000			
Total		67426	48125				

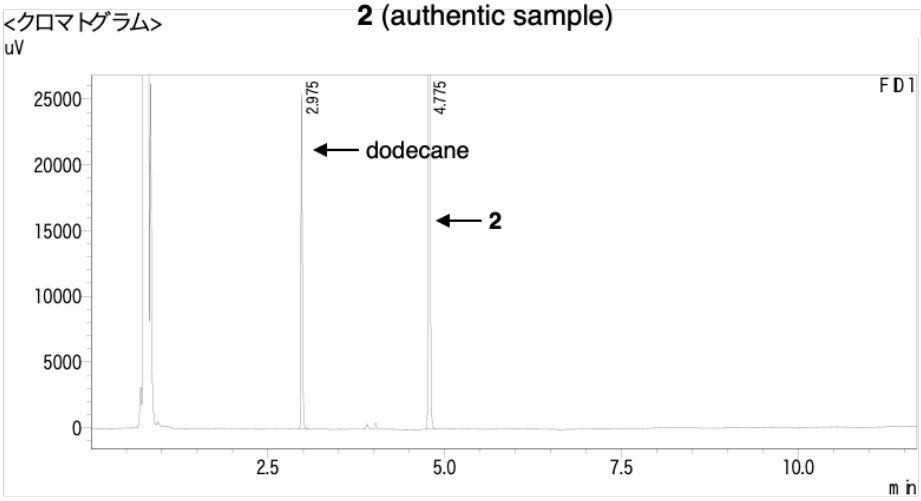

<ピークレポート>

FD1	Ret. Time	Area	Height				
ピーク#	保持時間	面積	高さ	濃度	単位	マーク	化合物名
1	2.975	34444	25014	0.000			
2	4.775	129778	87412	0.000			
Total		164223	112426				

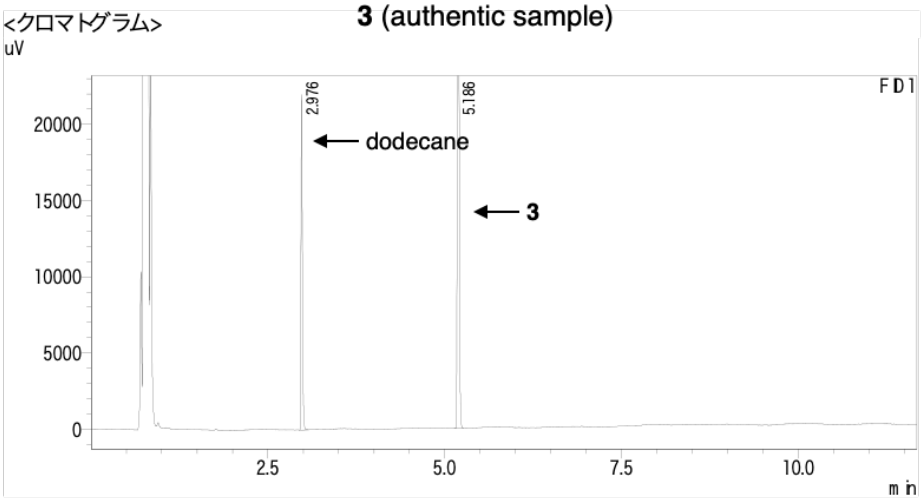

<ピークレポート>

FD1

ピーク#	Ret. Time 保持時間	Area 面積	Height 高さ	濃度	単位	マーク	化合物名
1	2.976	29809	21650	0.000			
2	5.186	100041	68485	0.000			
Total		129850	90134				

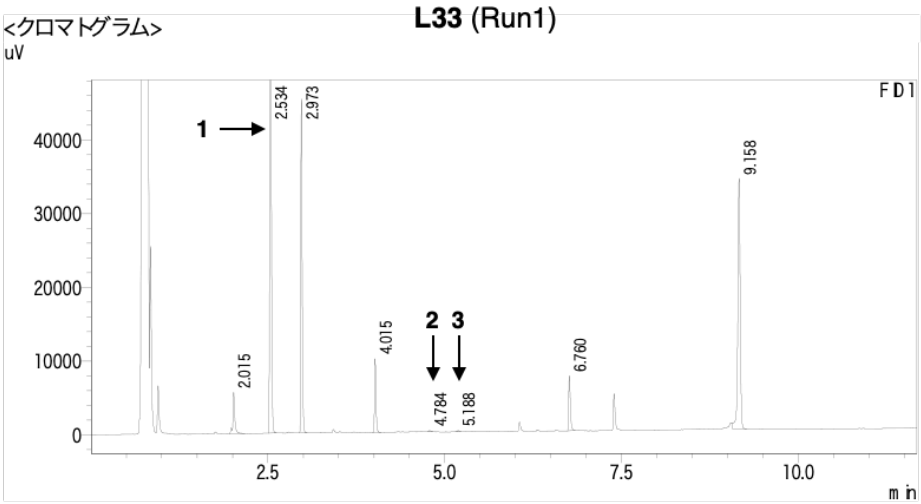

<ピークレポート>

FD1	Ret. Time	Area	Height				
ピーク#	保持時間	面積	高さ	濃度	単位	マーク	化合物名
1	2.015	10535	5575	3.400			
2	2.534	133873	97224	43.209			
3	2.973	61057	44142	19.707			
4	4.015	14141	9751	4.564			
5	4.784	295	172	0.095		M	
6	5.188	309	192	0.100		M	
7	6.760	12166	7369	3.927			
8	9.158	77447	33754	24.997		V	
Total		309824	198177				

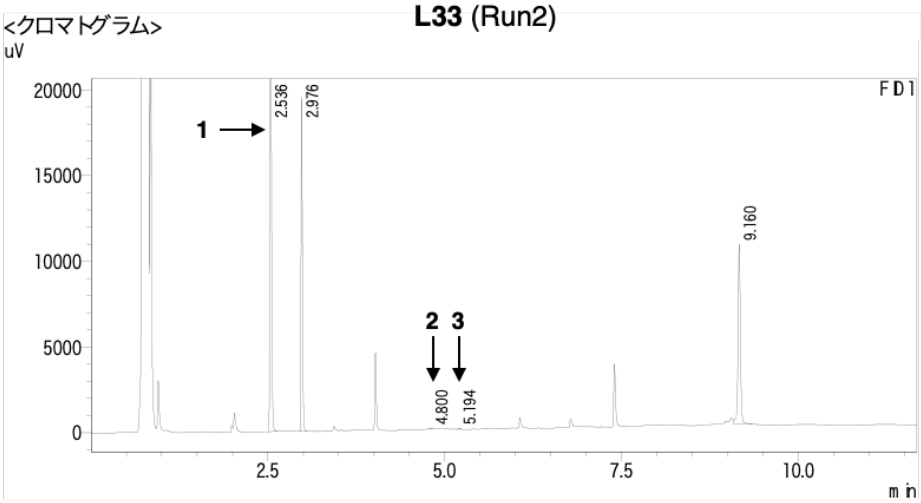

<ピークレポート>

FD1	Ret. Time	Area	Height				
ピーク#	保持時間	面積	高さ	濃度	単位	マーク	化合物名
1	2.536	57169	40923	52.776			
2	2.976	26556	19246	24.515			
3	4.800	77	38	0.071		M	
4	5.194	92	60	0.085		M	
5	9.160	24431	10447	22.553		V	
Total		108326	70714				

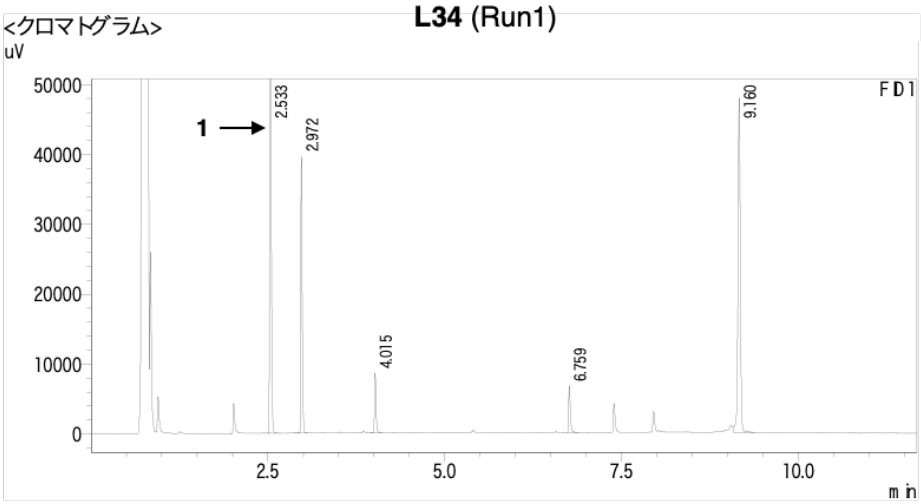

<ピークレポート>

FD1	Ret. Time	Area	Height				
ピーク#	保持時間	面積	高さ	濃度	単位	マーク	化合物名
1	2.533	119419	87600	0.000			
2	2.972	53372	38801	0.000		V	
3	4.015	12374	8355	0.000		V	
4	6.759	11070	6576	0.000			
5	9.160	108195	47539	0.000		V	
Total		304430	188871				

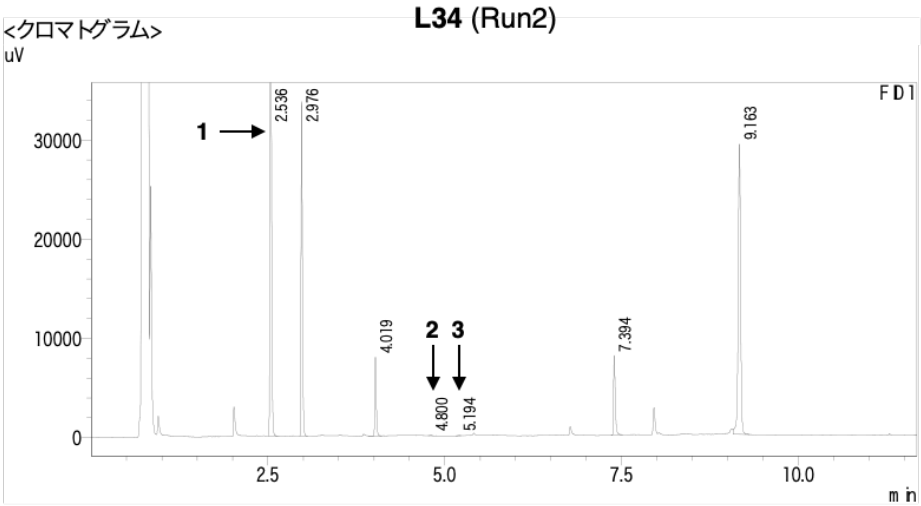

<ピークレポート>

FD1	Ret. Time	Area	Height				
ピーク#	保持時間	面積	高さ	濃度	単位	マーク	化合物名
1	2.536	98488	72335	41.542			
2	2.976	45327	33329	19.119			
3	4.019	11414	7593	4.814		V	
4	4.800	42	32	0.018		M	
5	5.194	63	39	0.027		M	
6	7.394	13475	7937	5.684			
7	9.163	68271	29110	28.797		V	
Total		237081	150375				

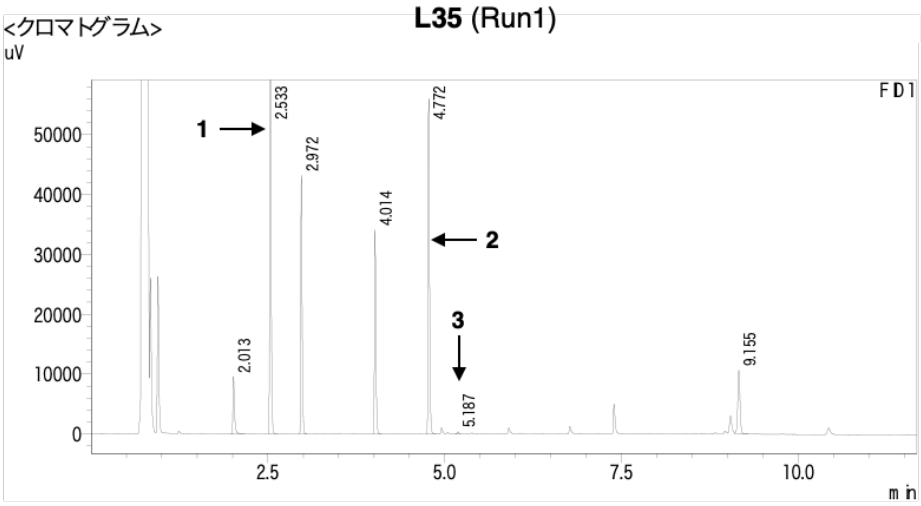

<ピークレポート>

FD1	Ret. Time	Area	Height				
ピーク#	保持時間	面積	高さ	濃度	単位	マーク	化合物名
1	2.013	14940	9335	4.668			
2	2.533	94325	69469	29.471			
3	2.972	57958	42371	18.109			
4	4.014	47556	32558	14.859			
5	4.772	80987	55340	25.304			
6	5.187	512	324	0.160		M	
7	9.155	23779	10598	7.429		V	
Total		320057	219995				

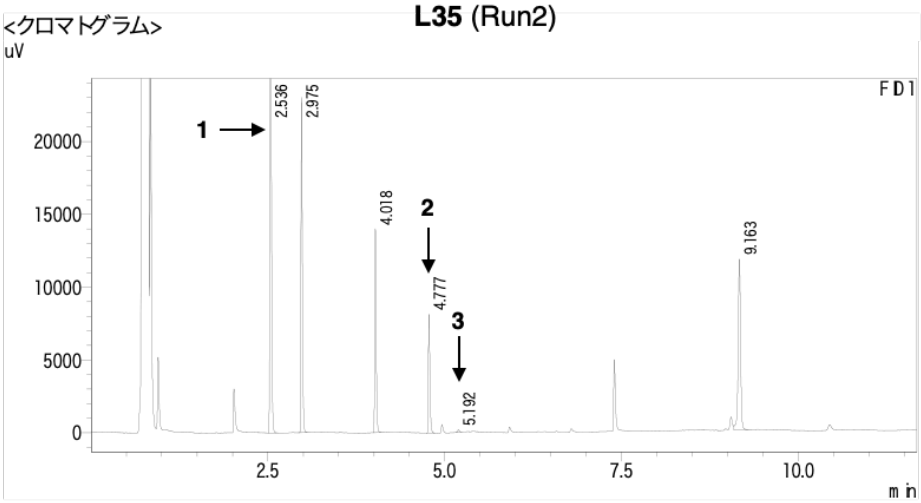

<ピークレポート>

FD1	Ret. Time	Area	Height				
ピーク#	保持時間	面積	高さ	濃度	単位	マーク	化合物名
1	2.536	62524	44887	40.722			
2	2.975	31210	22654	20.327			
3	4.018	19828	13669	12.914			
4	4.777	12188	8062	7.938			
5	5.192	279	173	0.182		M	
6	9.163	27511	11637	17.918		V	
Total		153539	101082				

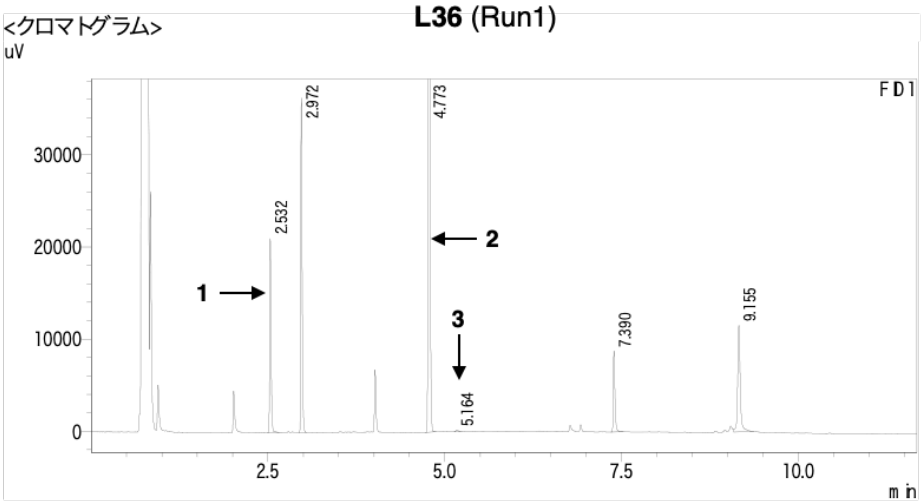

<ピークレポート>

FD1	Ret. Time	Area	Height				
ﾋﾟｰｸ#	保持時間	面積	高さ	濃度	単位	ﾏｰｸ	化合物名
1	2.532	28843	20793	9.059			
2	2.972	48970	35721	15.380			
3	4.773	196060	136321	61.578			
4	5.164	397	166	0.125		M	
5	7.390	14545	8692	4.568			
6	9.155	29580	11507	9.290		V	
Tota		318395	213199				

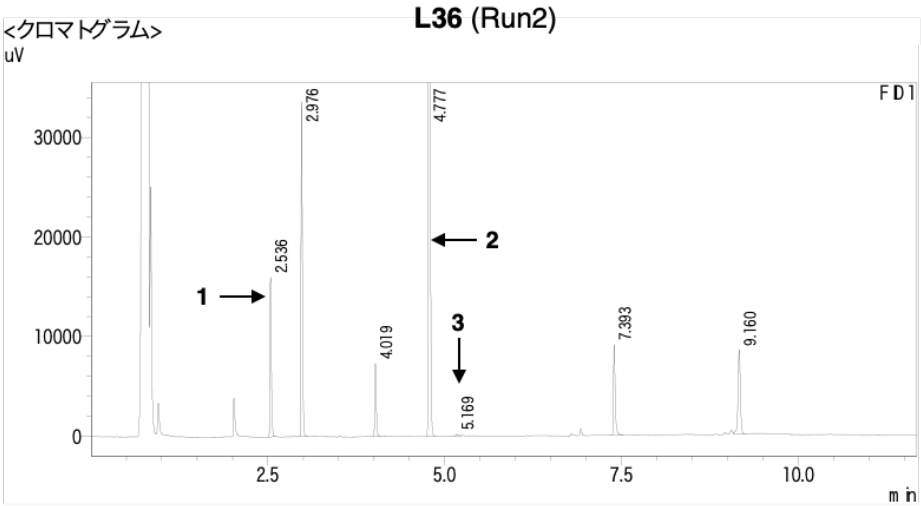

<ピークレポート>

FD1	Ret. Time	Area	Height				
ﾋﾟｰｸ#	保持時間	面積	高さ	濃度	単位	ﾏｰｸ	化合物名
1	2.536	21961	15677	7.329			
2	2.976	45443	33227	15.166			
3	4.019	10499	7044	3.504			
4	4.777	186570	129102	62.265			
5	5.169	410	164	0.137		M	
6	7.393	15170	8810	5.063			
7	9.160	19585	8417	6.536		V	
Tota		299639	202440				

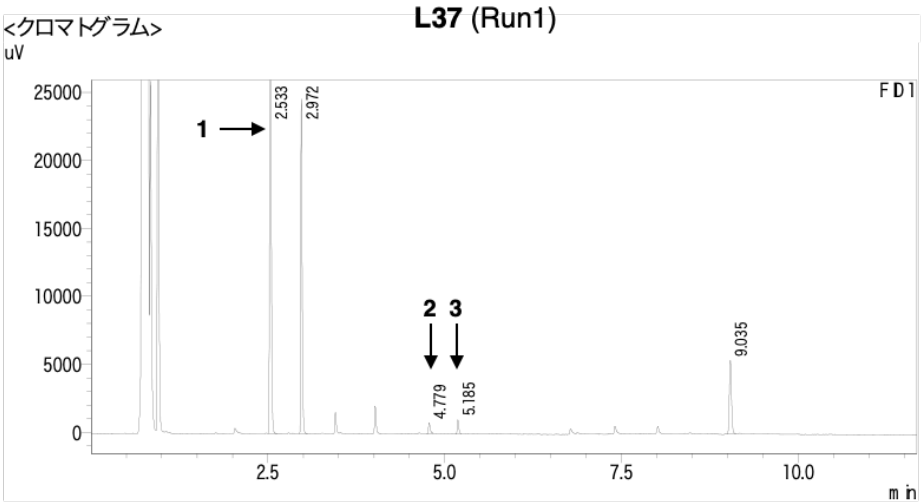

<ピークレポート>

FD1

ピーク#	Ret. Time 保持時間	Area 面積	Height 高さ	濃度	単位	マーク	化合物名
1	2.533	70204	51492	59.653			
2	2.972	33292	24155	28.288			
3	4.779	1285	790	1.092		M	
4	5.185	1513	1002	1.286		M	
5	9.035	11393	5365	9.680			
Total		117687	82804				

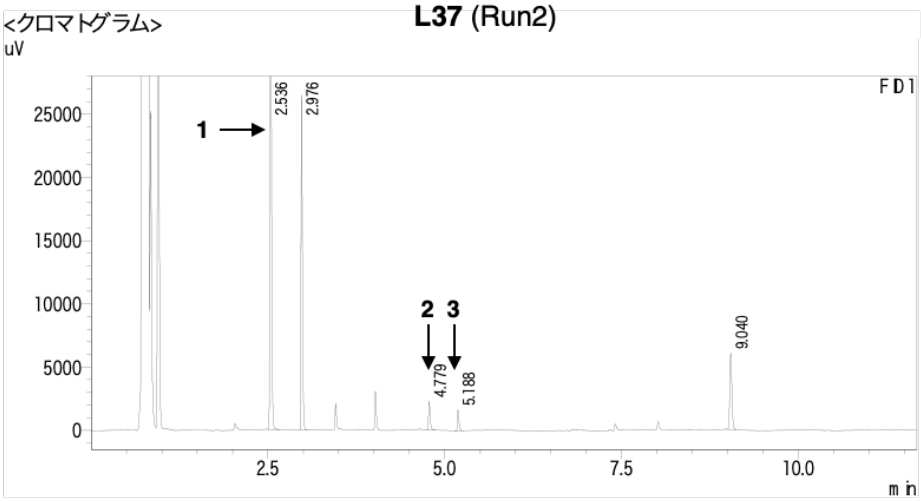

<ピークレポート>

FD1

ピーク#	Ret. Time 保持時間	Area 面積	Height 高さ	濃度	単位	マーク	化合物名
1	2.536	81435	59161	59.873			
2	2.976	35922	26181	26.411			
3	4.779	3541	2166	2.603		M	
4	5.188	2396	1618	1.761		M	
5	9.040	12719	5955	9.351		V	
Total		136012	95080				

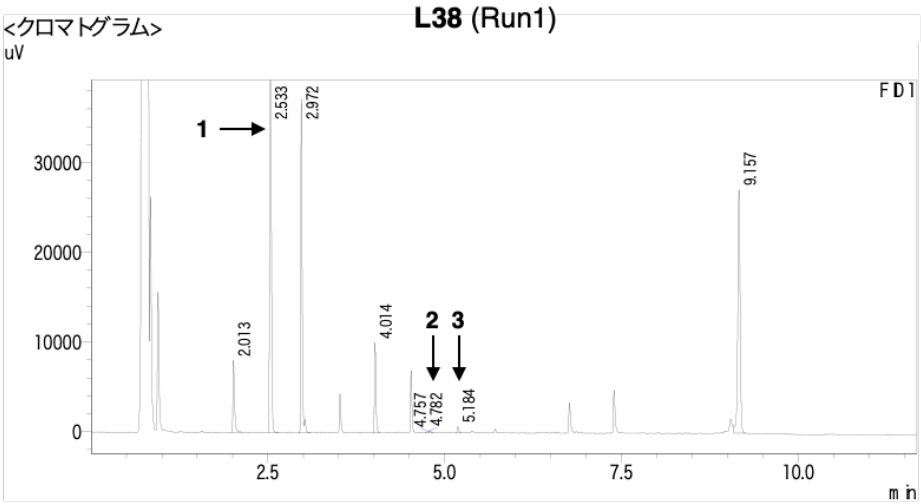

<ピークレポート>

FD1	Ret. Time	Area	Height				
ピーク#	保持時間	面積	高さ	濃度	単位	マーク	化合物名
1	2.013	12582	7843	4.998			
2	2.533	109300	80015	43.421			
3	2.972	51910	36569	20.622			
4	4.014	14291	9701	5.677			
5	4.757	182	152	0.072		M	
6	4.782	355	203	0.141		V M	
7	5.184	977	666	0.388		M	
8	9.157	62127	26716	24.681		V	
Total		251723	161865				

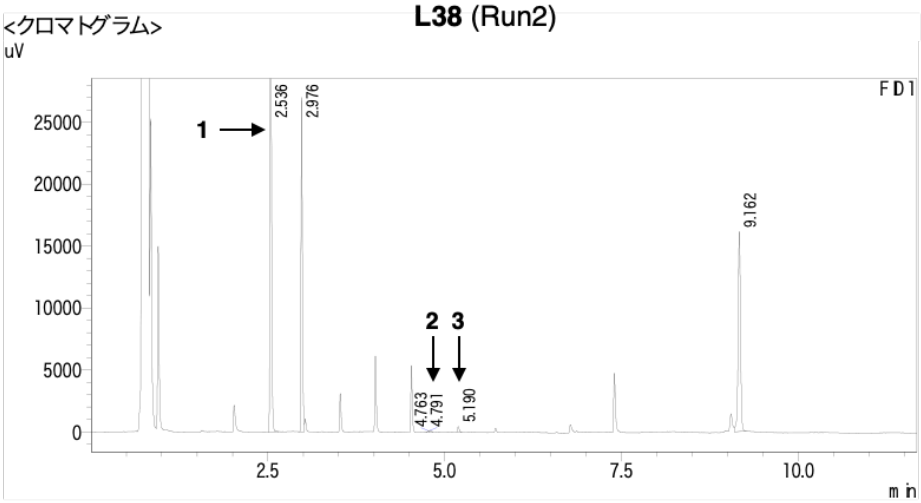

<ピークレポート>

FD1	Ret. Time	Area	Height				
ピーク#	保持時間	面積	高さ	濃度	単位	マーク	化合物名
1	2.536	78852	57480	51.293			
2	2.976	36529	26682	23.762			
3	4.763	130	104	0.084		M	
4	4.791	203	117	0.132		V M	
5	5.190	684	437	0.445		M	
6	9.162	37330	15936	24.283		V	
Total		153728	100756				

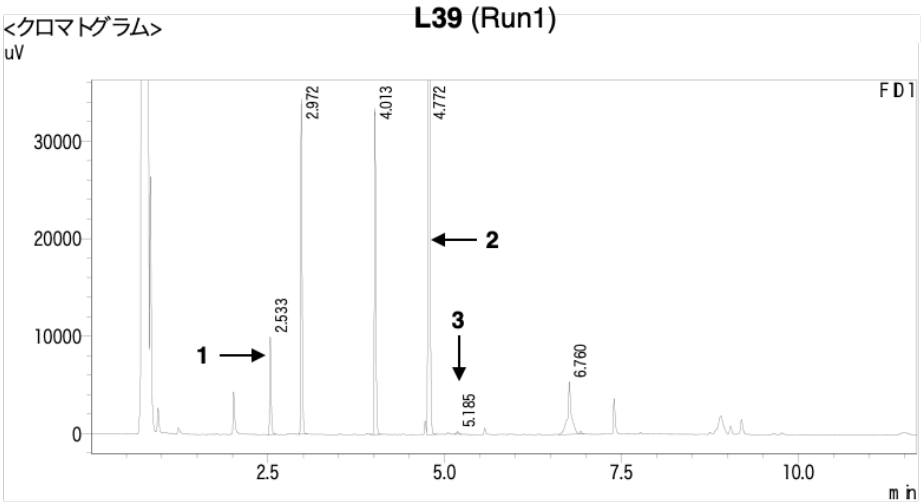

<ピークレポート>

FD1 Ret. Time Area Height

ピーク#	保持時間	面積	高さ	濃度	単位	マーク	化合物名
1	2.533	13883	9920	3.973			
2	2.972	46806	34000	13.394			
3	4.013	47174	32709	13.499		V	
4	4.772	220983	152781	63.236		V	
5	5.185	595	280	0.170		M	
6	6.760	20016	5357	5.728		S	
Tota		349458	235047				

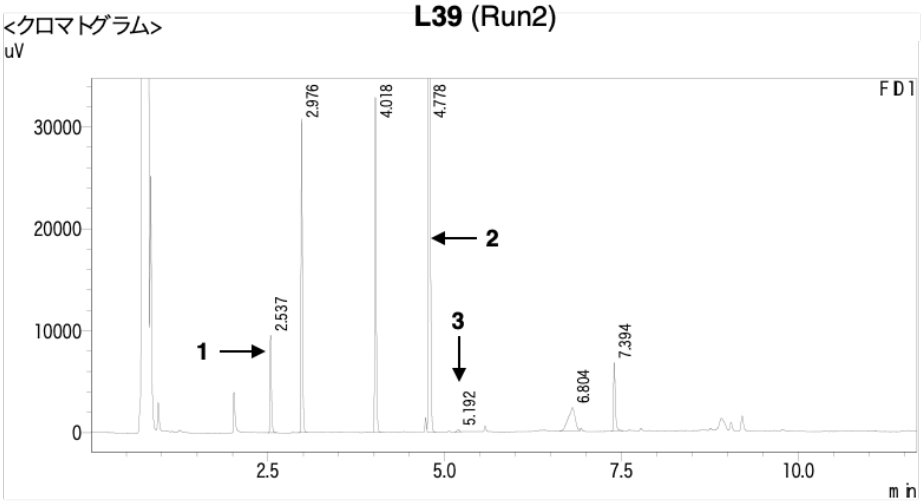

<ピークレポート>

FD1 Ret. Time Area Height

ピーク#	保持時間	面積	高さ	濃度	単位	マーク	化合物名
1	2.537	13373	9432	4.196			
2	2.976	41701	30433	13.086			
3	4.018	46451	32092	14.577		V	
4	4.778	189204	132058	59.373		V	
5	5.192	512	233	0.161		M	
6	6.804	15872	2317	4.981			
7	7.394	11556	6657	3.626			
Tota		318668	213223				

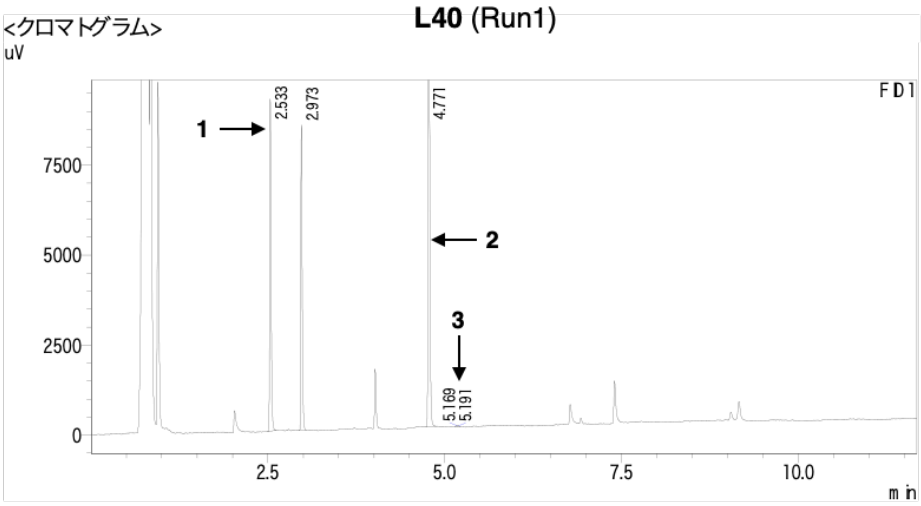

<ピークレポート>

FD1 Ret. Time Area Height

ピーク#	保持時間	面積	高さ	濃度	単位	マーク	化合物名
1	2.533	12878	9126	23.995			
2	2.973	11627	8274	21.664			
3	4.771	29099	19664	54.219			
4	5.169	45	29	0.083		M	
5	5.191	21	23	0.039		V M	
Total		53670	37115				

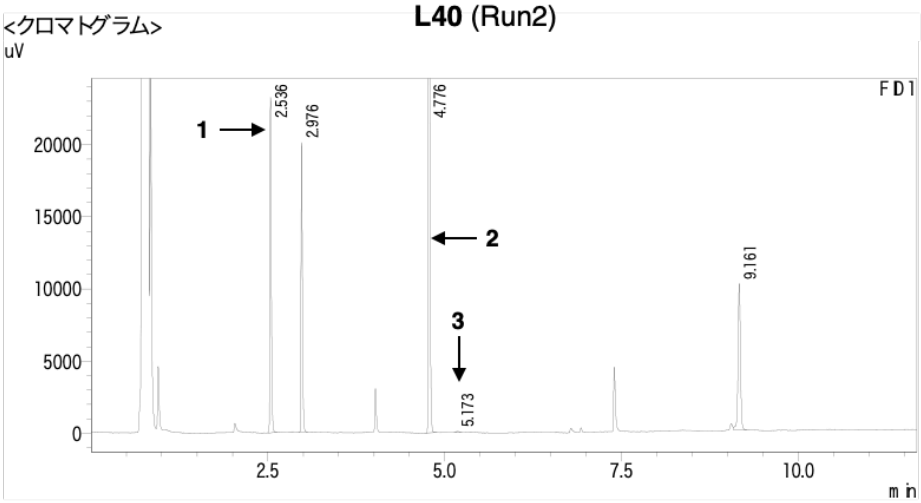

<ピークレポート>

FD1 Ret. Time Area Height

ピーク#	保持時間	面積	高さ	濃度	単位	マーク	化合物名
1	2.536	31693	22664	21.348			
2	2.976	27244	19813	18.351			
3	4.776	65729	44641	44.274			
4	5.173	185	66	0.125		M	
5	9.161	23608	10035	15.902		V	
Total		148460	97219				

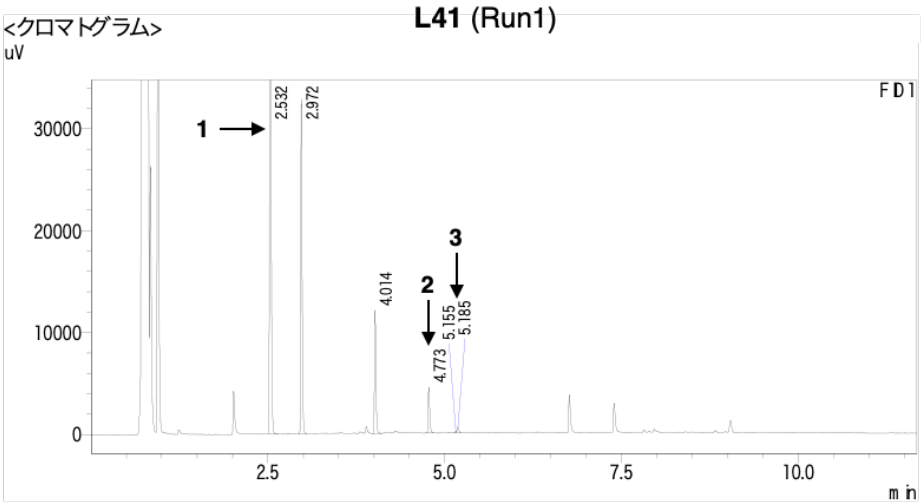

<ピークレポート>

FD1	Ret. Time	Area	Height				
ピーク#	保持時間	面積	高さ	濃度	単位	マーク	化合物名
1	2.532	95330	69832	57.906			
2	2.972	44291	32438	26.904			
3	4.014	17164	11736	10.426			
4	4.773	6735	4437	4.091		M	
5	5.155	157	145	0.096		M	
6	5.185	951	585	0.578		V M	
Total		164628	119174				

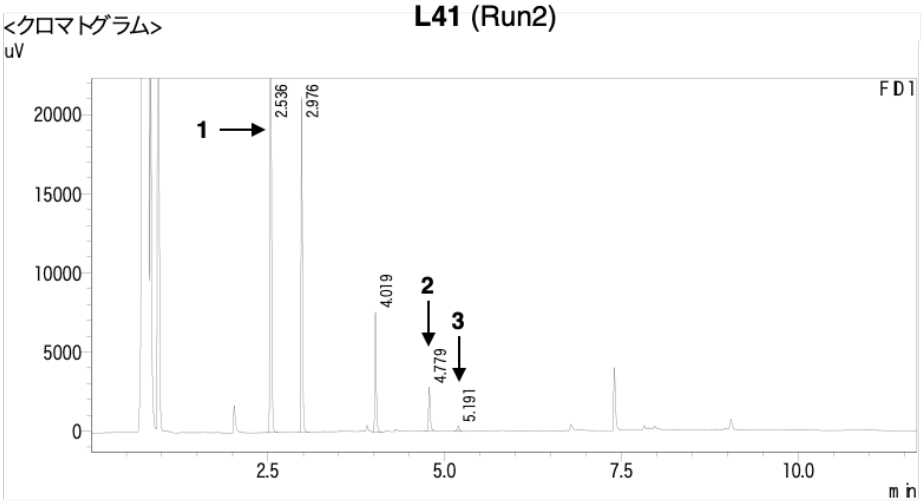

<ピークレポート>

FD1	Ret. Time	Area	Height				
ピーク#	保持時間	面積	高さ	濃度	単位	マーク	化合物名
1	2.536	60150	43182	57.501			
2	2.976	28697	20898	27.433			
3	4.019	10856	7294	10.378		V	
4	4.779	4298	2702	4.108		M	
5	5.191	607	344	0.581		M	
Total		104608	74420				

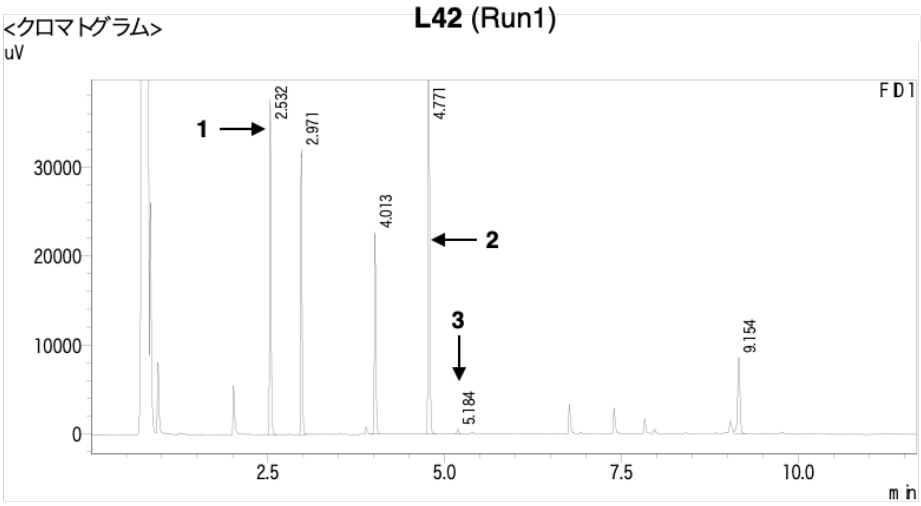

<ピークレポート>

FD1 Ret. Time Area Height

ピーク#	保持時間	面積	高さ	濃度	単位	マーク	化合物名
1	2.532	51162	37062	20.205			
2	2.971	43165	31661	17.047			
3	4.013	32039	22142	12.653		V	
4	4.771	106165	72504	41.926			
5	5.184	894	524	0.353		M	
6	9.154	19792	8531	7.816		V	
Total		253217	172423				

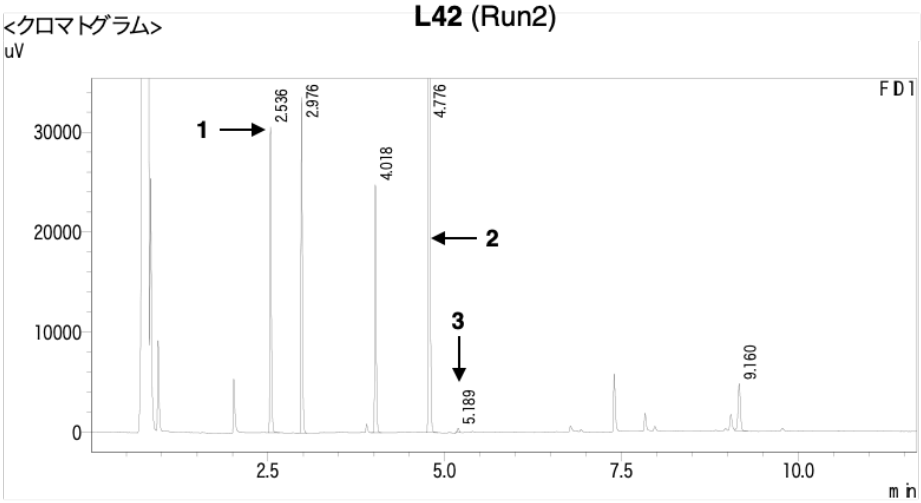

<ピークレポート>

FD1 Ret. Time Area Height

ピーク#	保持時間	面積	高さ	濃度	単位	マーク	化合物名
1	2.536	41935	29525	15.563			
2	2.976	45242	33036	16.791			
3	4.018	35025	24396	12.999		V	
4	4.776	135526	92907	50.297			
5	5.189	707	418	0.262		M	
6	9.160	11014	4716	4.088		V	
Total		269450	184999				

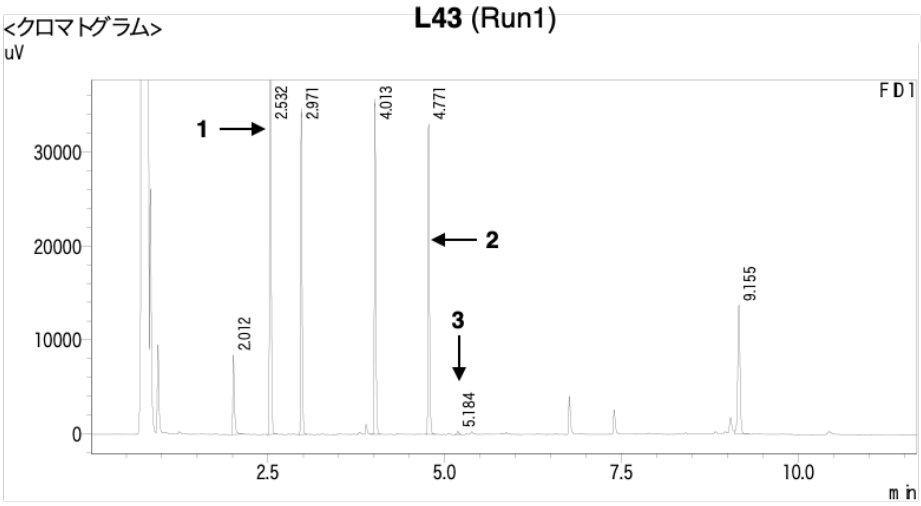

<ピークレポート>

FD1	Ret. Time	Area	Height				
ピーク#	保持時間	面積	高さ	濃度	単位	マーク	化合物名
1	2.012	13158	8171	4.837			
2	2.532	83040	60665	30.528			
3	2.971	46858	34289	17.226			
4	4.013	50062	34744	18.404		V	
5	4.771	47457	32125	17.447			
6	5.184	633	340	0.233		M	
7	9.155	30803	13631	11.324		V	
Total		272010	183966				

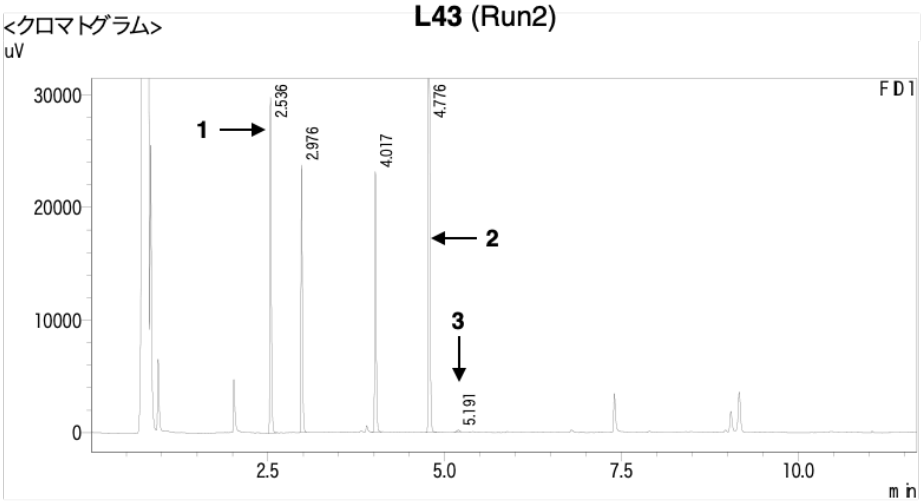

<ピークレポート>

FD1	Ret. Time	Area	Height				
ピーク#	保持時間	面積	高さ	濃度	単位	マーク	化合物名
1	2.536	40247	28763	23.044			
2	2.976	32022	23374	18.335			
3	4.017	32725	22797	18.738		V	
4	4.776	69306	46655	39.683			
5	5.191	348	167	0.199		M	
Total		174648	121757				

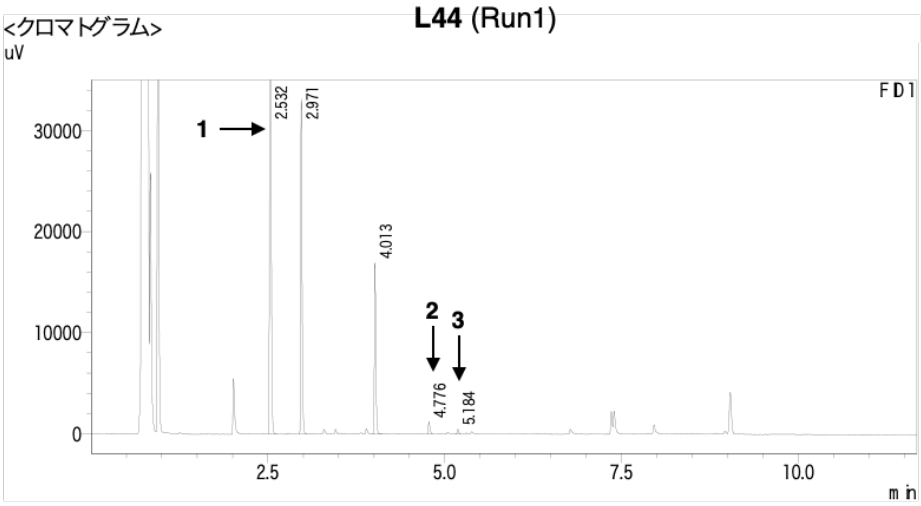

<ピークレポート>

FD1	Ret. Time	Area	Height				
ピーク#	保持時間	面積	高さ	濃度	単位	マーク	化合物名
1	2.532	95612	69865	57.284			
2	2.971	44735	32759	26.802			
3	4.013	24108	16622	14.444		V	
4	4.776	1827	1177	1.094		M	
5	5.184	626	435	0.375		M	
Total		166907	120858				

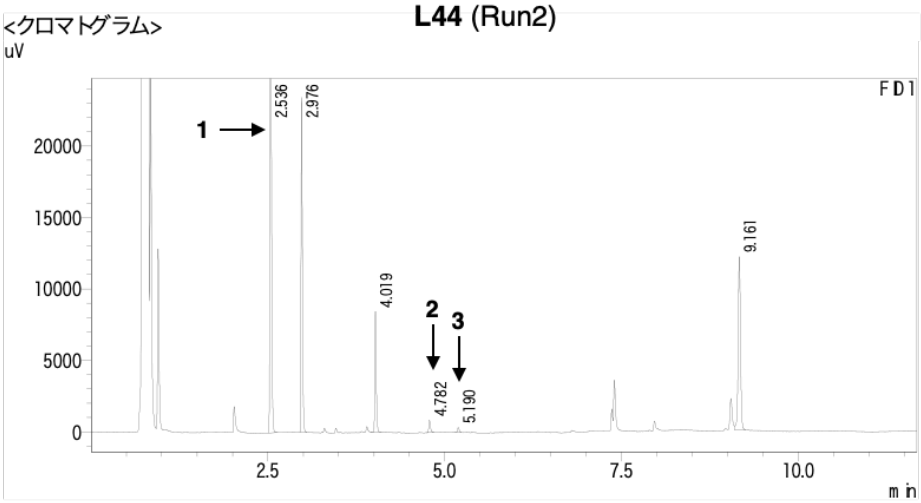

<ピークレポート>

FD1	Ret. Time	Area	Height				
ピーク#	保持時間	面積	高さ	濃度	単位	マーク	化合物名
1	2.536	67659	48857	47.990			
2	2.976	31474	23142	22.324			
3	4.019	12097	8180	8.580		V	
4	4.782	1380	852	0.979		M	
5	5.190	549	334	0.390		M	
6	9.161	27826	11971	19.737		V	
Total		140985	93336				

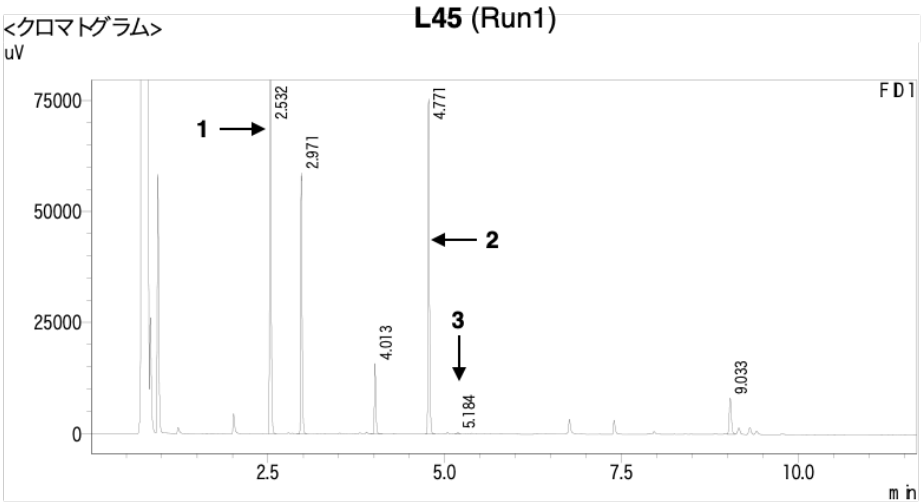

<ピークレポート>

FD1 Ret. Time Area Height

ピーク#	保持時間	面積	高さ	濃度	単位	マーク	化合物名
1	2.532	131477	97233	36.736			
2	2.971	78705	58018	21.991			
3	4.013	22514	15560	6.291		V	
4	4.771	107530	73485	30.045			
5	5.184	564	305	0.157		M	
6	9.033	17112	8132	4.781		V	
Total		357901	252734				

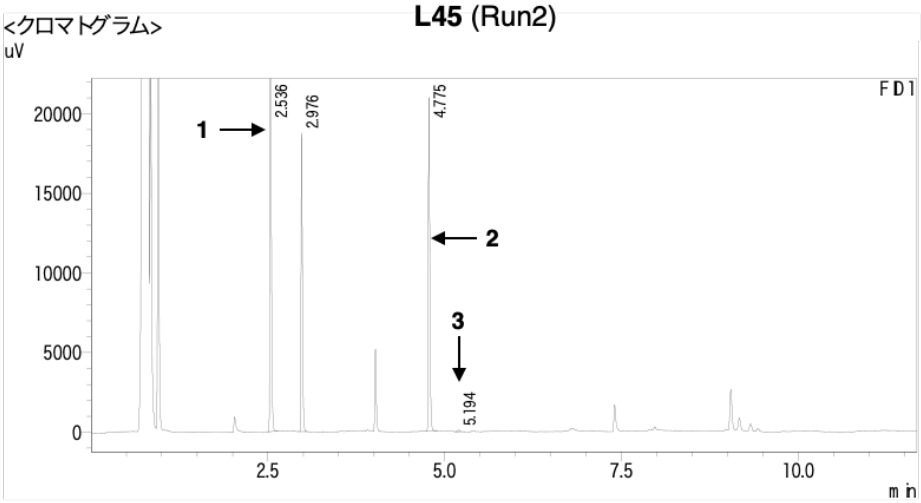

<ピークレポート>

FD1 Ret. Time Area Height

ピーク#	保持時間	面積	高さ	濃度	単位	マーク	化合物名
1	2.536	42275	30174	42.866			
2	2.976	25559	18528	25.917			
3	4.775	30614	20223	31.042			
4	5.194	172	88	0.175		M	
Total		98620	69013				

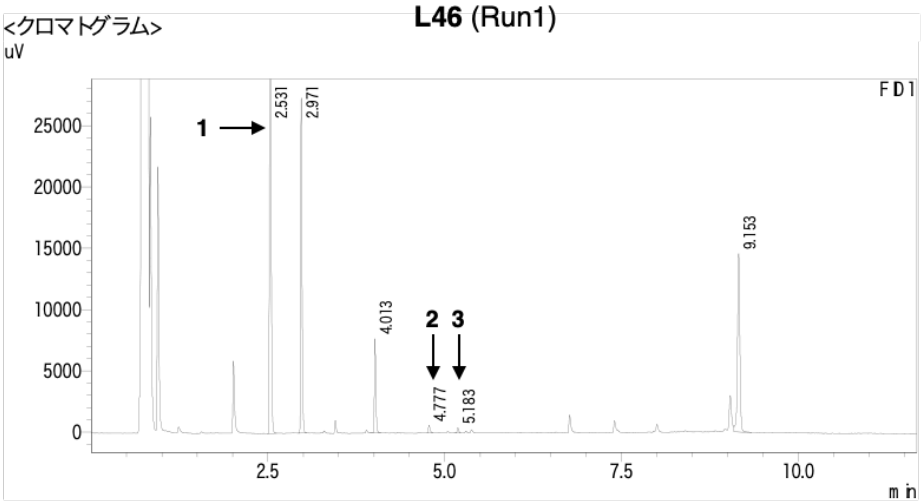

<ピークレポート>

FD1

ピーク#	Ret. Time 保持時間	Area 面積	Height 高さ	濃度	単位	マーク	化合物名
1	2.531	79065	57101	48.755			
2	2.971	36916	26978	22.764			
3	4.013	10970	7540	6.765		V	
4	4.777	1023	631	0.631		M	
5	5.183	633	415	0.390		M	
6	9.153	33561	14403	20.695		V	
Total		162169	107070				

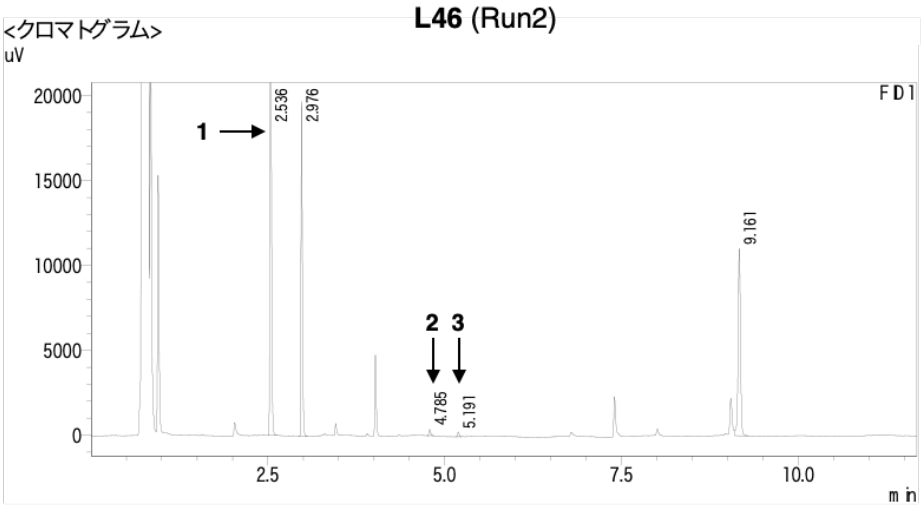

<ピークレポート>

FD1

ピーク#	Ret. Time 保持時間	Area 面積	Height 高さ	濃度	単位	マーク	化合物名
1	2.536	56627	40500	51.750			
2	2.976	26521	19455	24.237			
3	4.785	616	367	0.563		M	
4	5.191	412	271	0.376		M	
5	9.161	25249	10864	23.075		V	
Total		109424	71457				

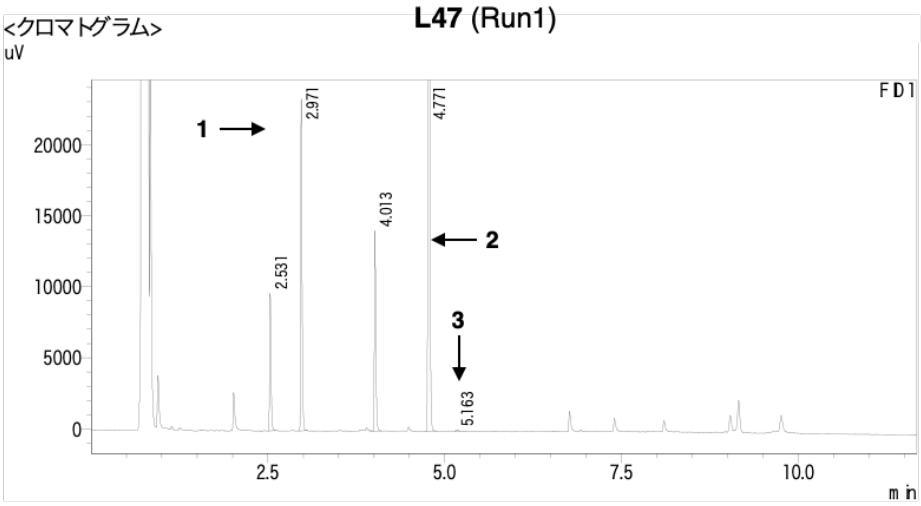

<ピークレポート>

FD1	Ret. Time	Area	Height				
ピーク#	保持時間	面積	高さ	濃度	単位	マーク	化合物名
1	2.531	13513	9504	7.009			
2	2.971	31667	23067	16.424			
3	4.013	20128	13871	10.439		V	
4	4.771	127262	86267	66.004			
5	5.163	240	87	0.124		M	
Total		192809	132797				

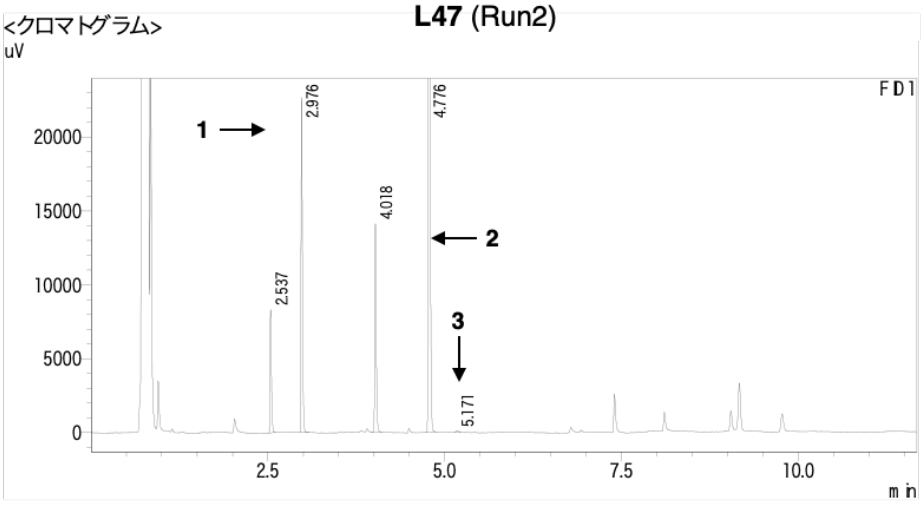

<ピークレポート>

FD1	Ret. Time	Area	Height				
ピーク#	保持時間	面積	高さ	濃度	単位	マーク	化合物名
1	2.537	11616	8221	6.067			
2	2.976	30795	22399	16.082			
3	4.018	20393	13736	10.650		V	
4	4.776	128441	88078	67.077			
5	5.171	237	84	0.124		M	
Total		191482	132517				

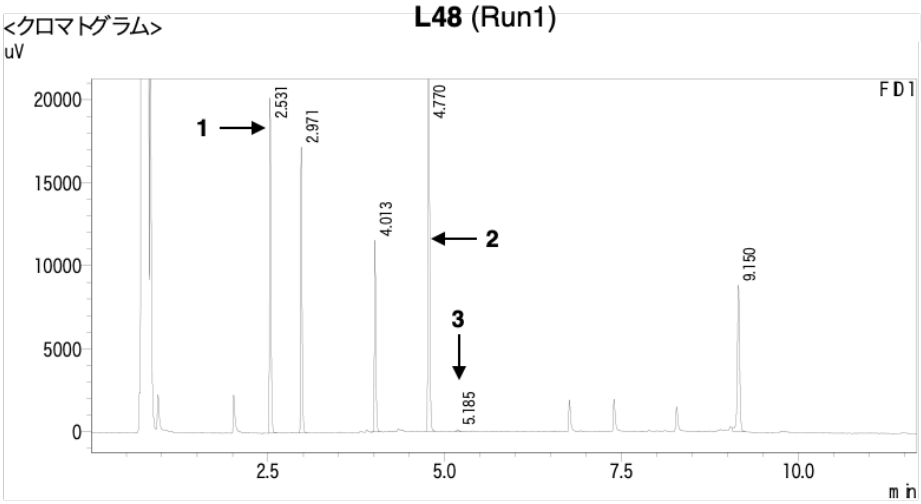

<ピークレポート>

FD1 Ret. Time Area Height

ピーク#	保持時間	面積	高さ	濃度	単位	マーク	化合物名
1	2.531	27518	19479	19.440			
2	2.971	23280	16977	16.446			
3	4.013	16411	11350	11.593		V	
4	4.770	54538	36392	38.528			
5	5.185	213	101	0.151		M	
6	9.150	19593	8768	13.842		V	
Total		141554	93068				

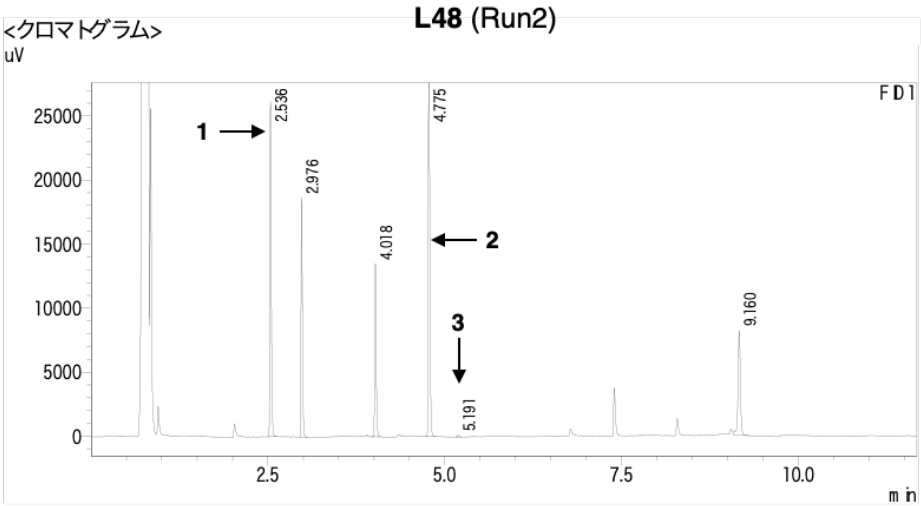

<ピークレポート>

FD1 Ret. Time Area Height

ピーク#	保持時間	面積	高さ	濃度	単位	マーク	化合物名
1	2.536	35659	25293	24.208			
2	2.976	25483	18438	17.300			
3	4.018	19061	13283	12.940		V	
4	4.775	47829	31958	32.471			
5	5.191	232	115	0.157		M	
6	9.160	19036	8124	12.923		V	
Total		147299	97210				

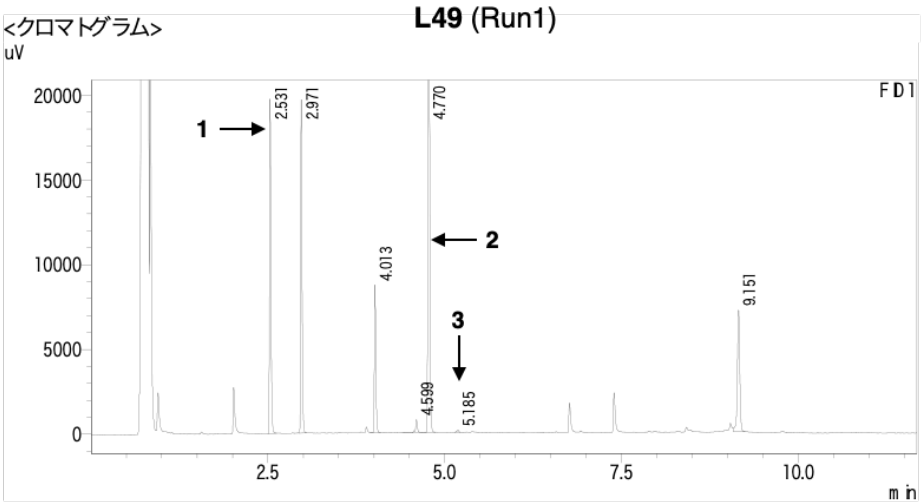

<ピークレポート>

FD1	Ret. Time	Area	Height				
ﾋﾟｰｸ#	保持時間	面積	高さ	濃度	単位	ﾏｰｸ	化合物名
1	2.531	26932	18958	17.384			
2	2.971	26658	19365	17.208			
3	4.013	12439	8597	8.029		V	
4	4.599	1064	733	0.686		M	
5	4.770	70715	47813	45.646			
6	5.185	266	131	0.171		M	
7	9.151	16848	7140	10.875		V	
Total		154921	102737				

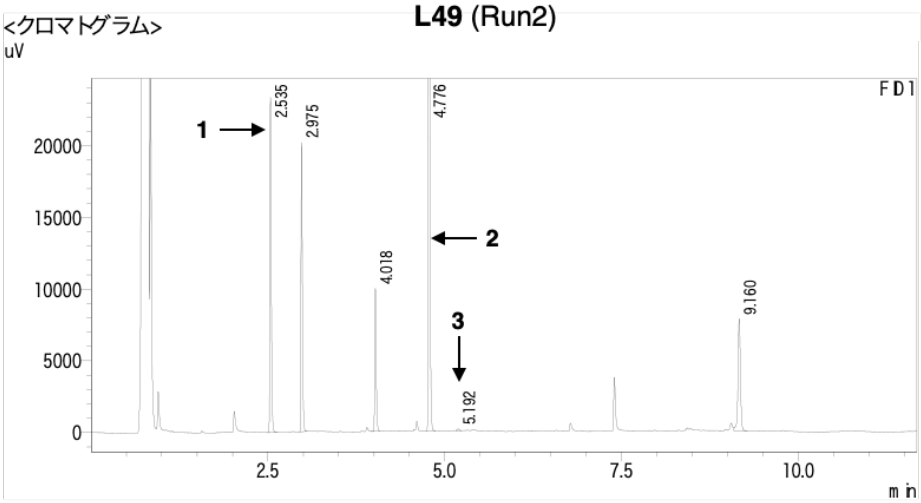

<ピークレポート>

FD1	Ret. Time	Area	Height				
ﾋﾟｰｸ#	保持時間	面積	高さ	濃度	単位	ﾏｰｸ	化合物名
1	2.535	31934	22542	20.622			
2	2.975	27446	19848	17.724			
3	4.018	14128	9746	9.124		V	
4	4.776	62571	42263	40.407			
5	5.192	257	124	0.166		M	
6	9.160	18517	7772	11.958		V	
Total		154853	102295				

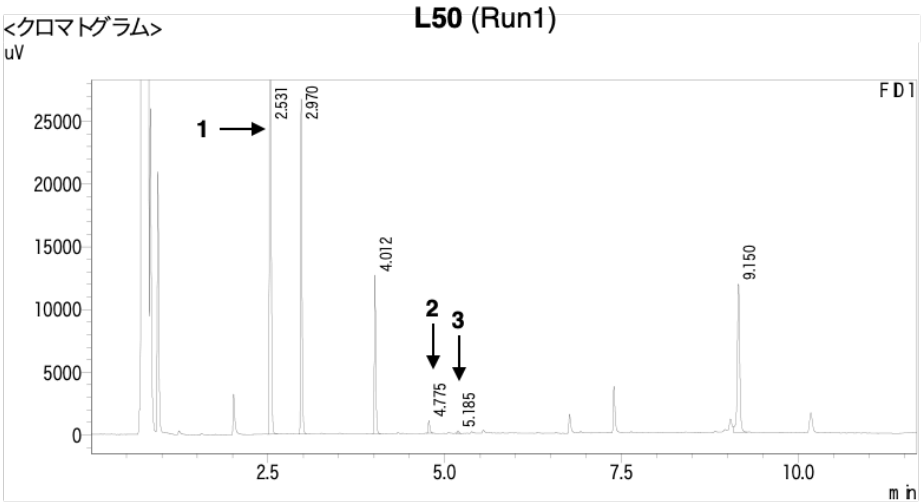

<ピークレポート>

FD1

ピーク#	Ret. Time 保持時間	Area 面積	Height 高さ	濃度	単位	マーク	化合物名
1	2.531	87357	63113	51.042			
2	2.970	36206	26122	21.155			
3	4.012	17867	12489	10.439			
4	4.775	1583	972	0.925		M	
5	5.185	300	191	0.175		M	
6	9.150	27834	11765	16.263		V	
Tota		171147	114652				

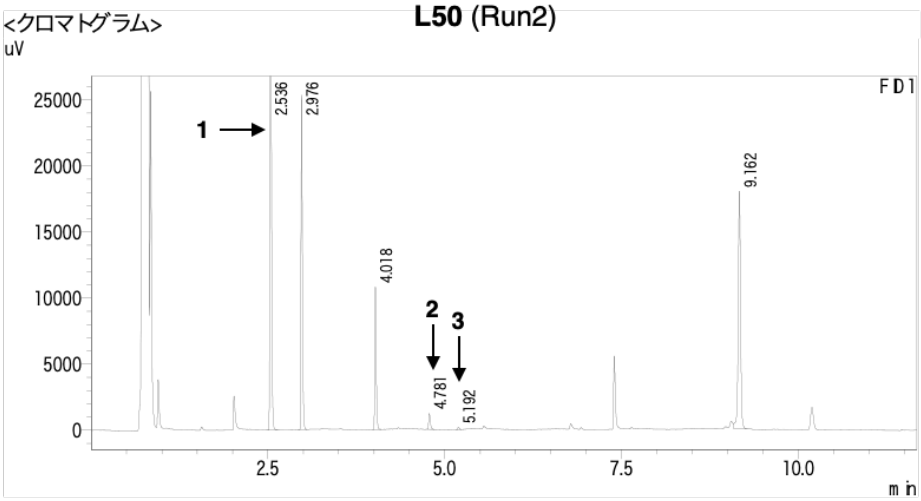

<ピークレポート>

FD1

ピーク#	Ret. Time 保持時間	Area 面積	Height 高さ	濃度	単位	マーク	化合物名
1	2.536	74145	53840	44.428			
2	2.976	34295	25032	20.550			
3	4.018	15359	10457	9.203			
4	4.781	1875	1180	1.124		M	
5	5.192	240	158	0.144		M	
6	9.162	40972	17851	24.551		V	
Tota		166887	108518				

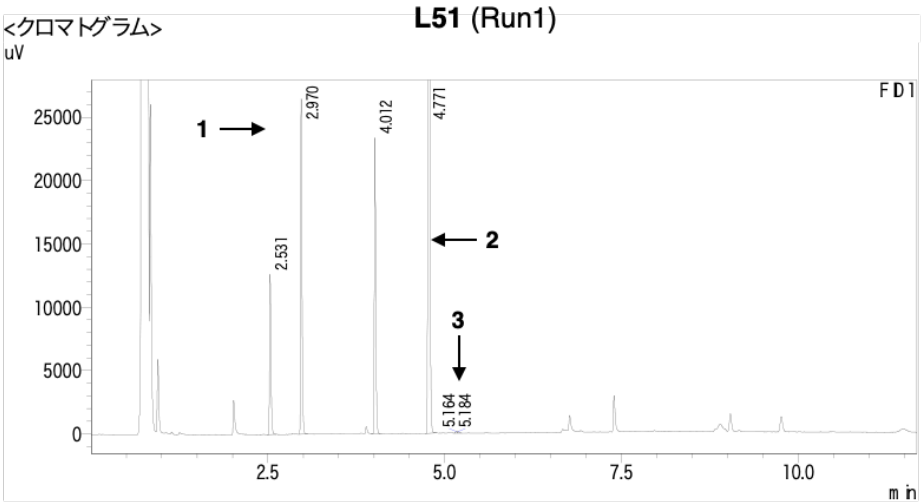

<ピークレポート>

FD1	Ret. Time	Area	Height				
ピーク#	保持時間	面積	高さ	濃度	単位	マーク	化合物名
1	2.531	17451	12257	6.995			
2	2.970	35586	25968	14.264			
3	4.012	33033	23112	13.241		V	
4	4.771	163055	110983	65.359			
5	5.164	134	117	0.054		M	
6	5.184	218	119	0.087		V M	
Total		249477	172556				

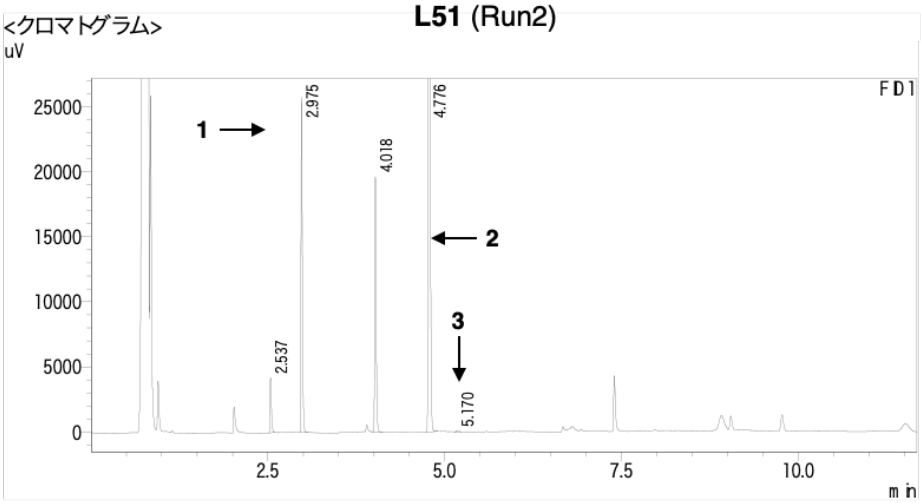

<ピークレポート>

FD1	Ret. Time	Area	Height				
ピーク#	保持時間	面積	高さ	濃度	単位	マーク	化合物名
1	2.537	5901	4130	2.502		M	
2	2.975	34872	25321	14.786			
3	4.018	27502	19320	11.662		V	
4	4.776	167303	113343	70.941			
5	5.170	258	100	0.109		M	
Total		235835	162213				

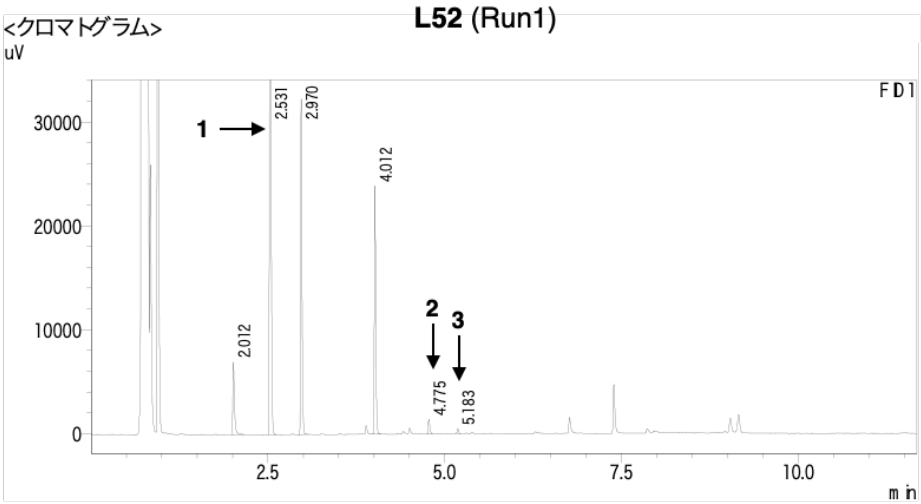

<ピークレポート>

FD1	Ret. Time	Area	Height				
ピーク#	保持時間	面積	高さ	濃度	単位	マーク	化合物名
1	2.012	11151	6844	5.611			
2	2.531	107725	77682	54.211			
3	2.970	43542	31601	21.912			
4	4.012	33555	23635	16.886			
5	4.775	2159	1363	1.087		M	
6	5.183	582	424	0.293		M	
Tota		198714	141549				

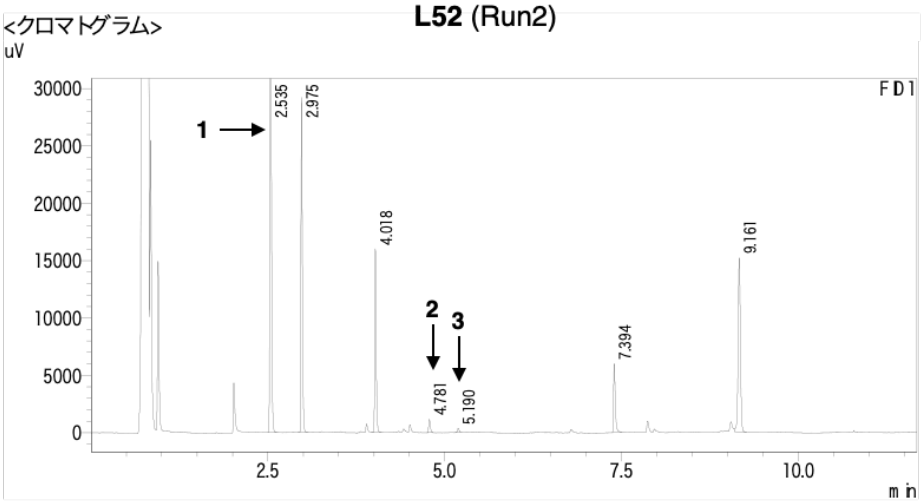

<ピークレポート>

FD1	Ret. Time	Area	Height				
ピーク#	保持時間	面積	高さ	濃度	単位	マーク	化合物名
1	2.535	82829	59508	43.326			
2	2.975	39632	28729	20.731			
3	4.018	22646	15709	11.846		V	
4	4.781	1820	1148	0.952		M	
5	5.190	541	353	0.283		M	
6	7.394	10203	5943	5.337			
7	9.161	33504	15002	17.525		V	
Tota		191174	126392				

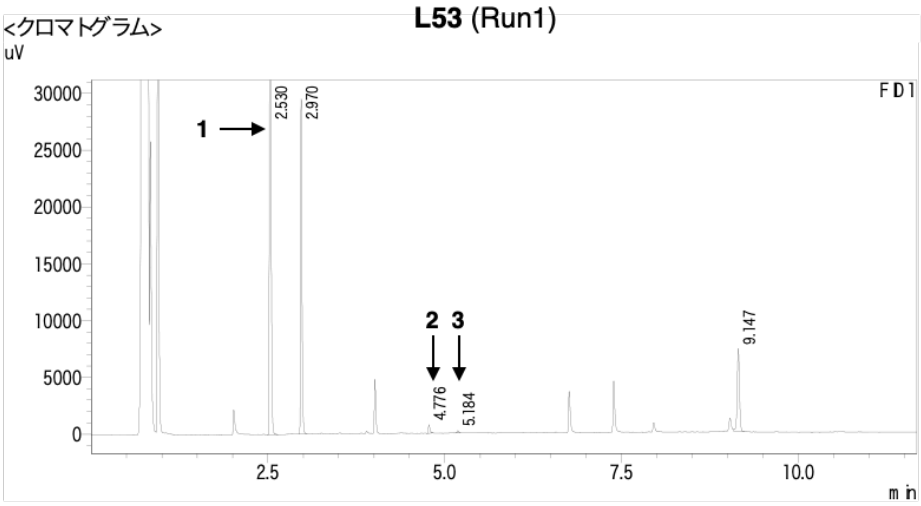

<ピークレポート>

FD1	Ret. Time	Area	Height				
ピーク#	保持時間	面積	高さ	濃度	単位	マーク	化合物名
1	2.530	94950	67760	62.339			
2	2.970	39708	28652	26.070			
3	4.776	1210	733	0.795		M	
4	5.184	295	194	0.194		M	
5	9.147	16149	7182	10.602		V	
Total		152312	104522				

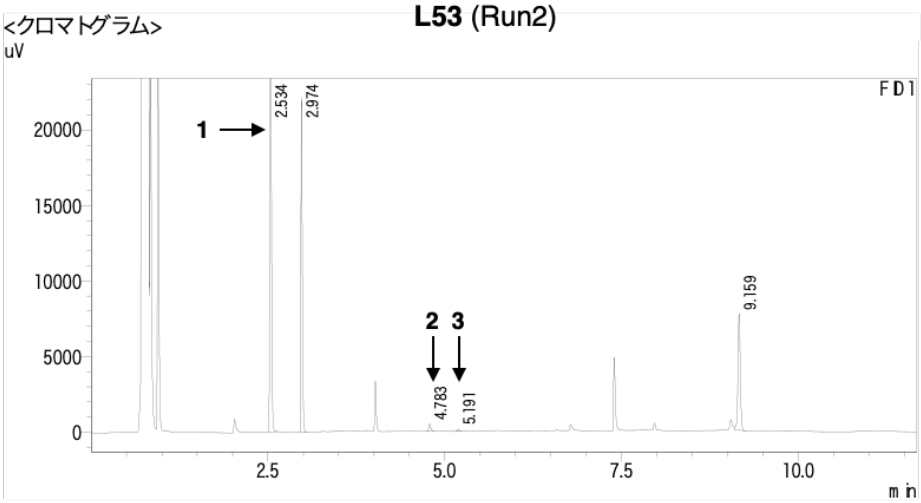

<ピークレポート>

FD1	Ret. Time	Area	Height				
ピーク#	保持時間	面積	高さ	濃度	単位	マーク	化合物名
1	2.534	64168	45688	56.754			
2	2.974	30204	21615	26.714			
3	4.783	815	461	0.721		M	
4	5.191	211	143	0.187		M	
5	9.159	17665	7696	15.624		V	
Total		113064	75603				

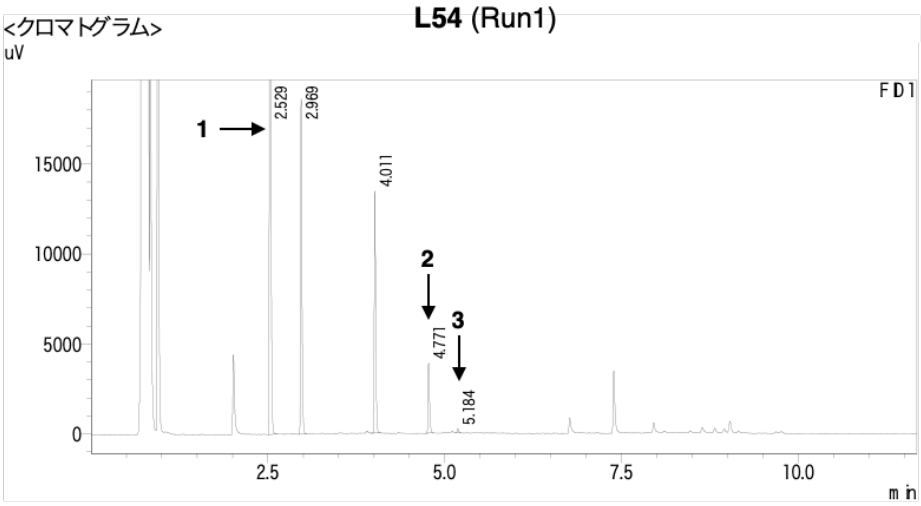

<ピークレポート>

FD1 Ret. Time Area Height

ピーク#	保持時間	面積	高さ	濃度	単位	マーク	化合物名
1	2.529	57415	41359	53.225			
2	2.969	25270	17987	23.426			
3	4.011	18982	13295	17.596		V	
4	4.771	5842	3820	5.416		M	
5	5.184	364	241	0.337		M	
Total		107872	76702				

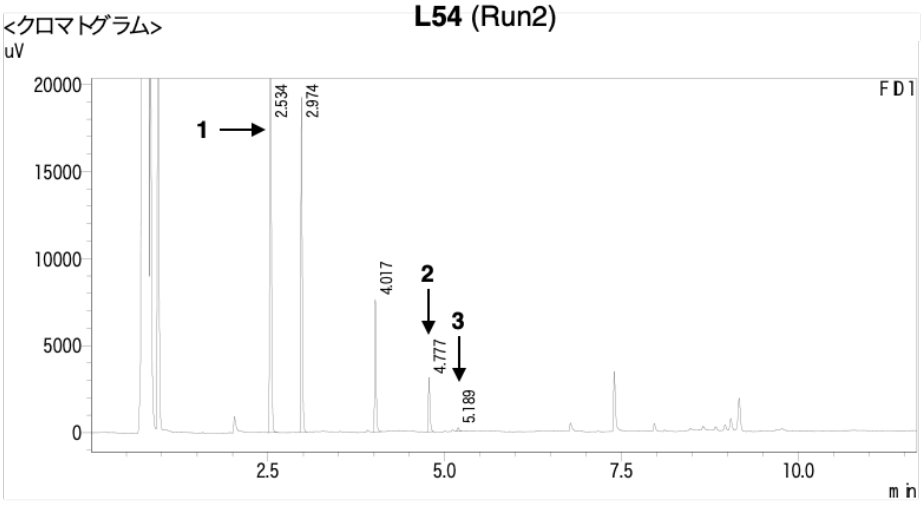

<ピークレポート>

FD1 Ret. Time Area Height

ピーク#	保持時間	面積	高さ	濃度	単位	マーク	化合物名
1	2.534	54001	39131	56.102			
2	2.974	26236	18381	27.257			
3	4.017	10945	7534	11.371			
4	4.777	4778	3084	4.964		M	
5	5.189	294	195	0.305		M	
Total		96255	68325				

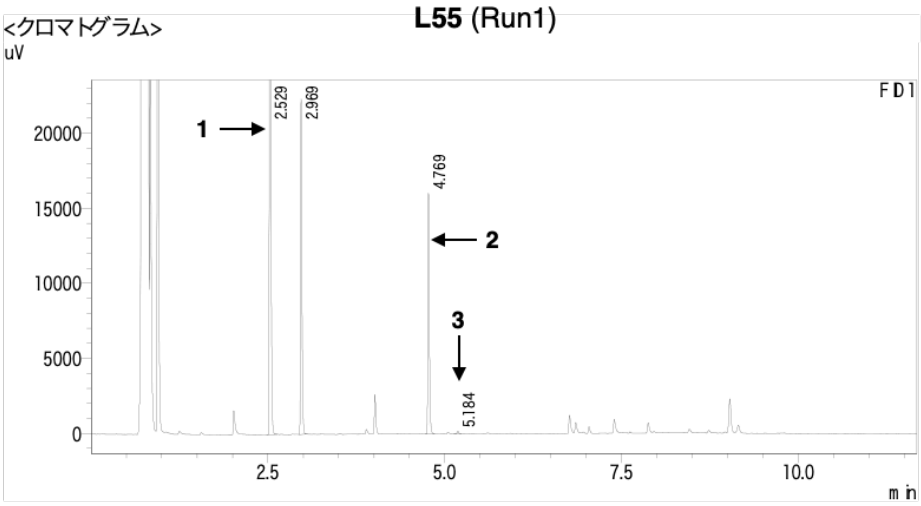

<ピークレポート>

FD1	Ret. Time	Area	Height				
ピーク#	保持時間	面積	高さ	濃度	単位	マーク	化合物名
1	2.529	66120	47814	55.171			
2	2.969	30147	21307	25.155			
3	4.769	23310	15814	19.450		M	
4	5.184	269	168	0.225		M	
Total		119845	85102				

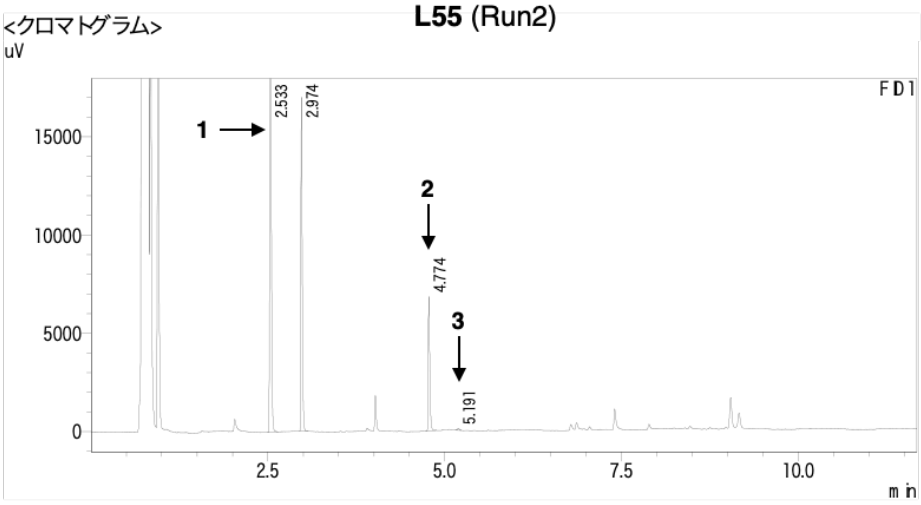

<ピークレポート>

FD1	Ret. Time	Area	Height				
ピーク#	保持時間	面積	高さ	濃度	単位	マーク	化合物名
1	2.533	45279	32613	57.367			
2	2.974	23144	16283	29.323			
3	4.774	10318	6613	13.073			
4	5.191	187	98	0.237		M	
Total		78929	55607				

L56 (Run1)

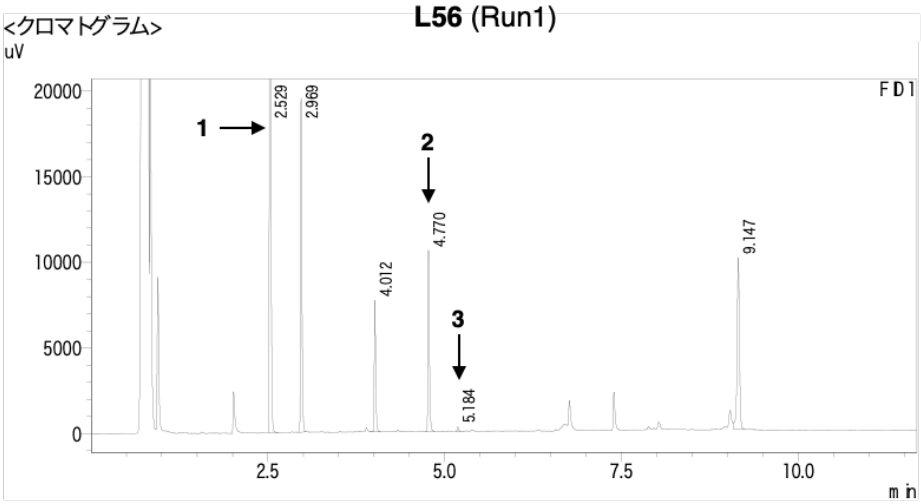

<ピークレポート>

FD1	Ret. Time	Area	Height				
ピーク#	保持時間	面積	高さ	濃度	単位	マーク	化合物名
1	2.529	57306	41559	42.872			
2	2.969	26474	18581	19.805			
3	4.012	10985	7581	8.218		V	
4	4.770	15640	10274	11.701			
5	5.184	364	252	0.272		M	
6	9.147	22901	9869	17.133		V	
Tota		133670	88115				

L56 (Run2)

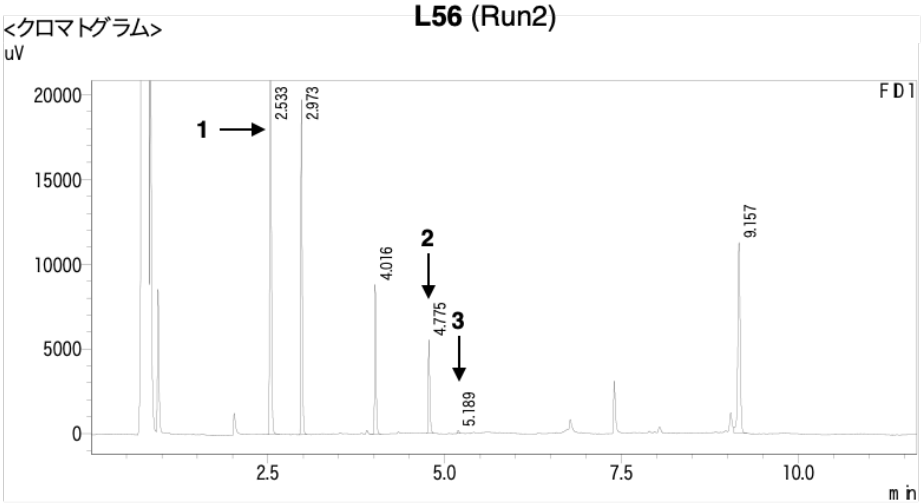

<ピークレポート>

FD1	Ret. Time	Area	Height				
ピーク#	保持時間	面積	高さ	濃度	単位	マーク	化合物名
1	2.533	55162	40102	42.872			
2	2.973	26856	19000	20.872			
3	4.016	12560	8721	9.762		V	
4	4.775	8169	5333	6.349		M	
5	5.189	262	182	0.203		M	
6	9.157	25657	11097	19.941		V	
Tota		128666	84435				

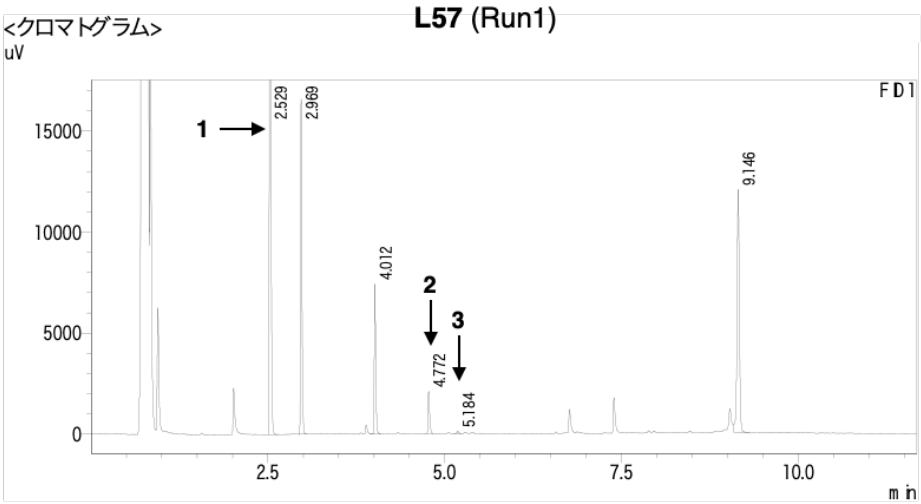

<ピークレポート>

FD1 Ret. Time Area Height

ピーク#	保持時間	面積	高さ	濃度	単位	マーク	化合物名
1	2.529	55469	40016	46.466			
2	2.969	22537	15921	18.879			
3	4.012	10614	7334	8.891		V	
4	4.772	3186	2054	2.669		M	
5	5.184	222	119	0.186		M	
6	9.146	27347	11936	22.908		V	
Total		119375	77379				

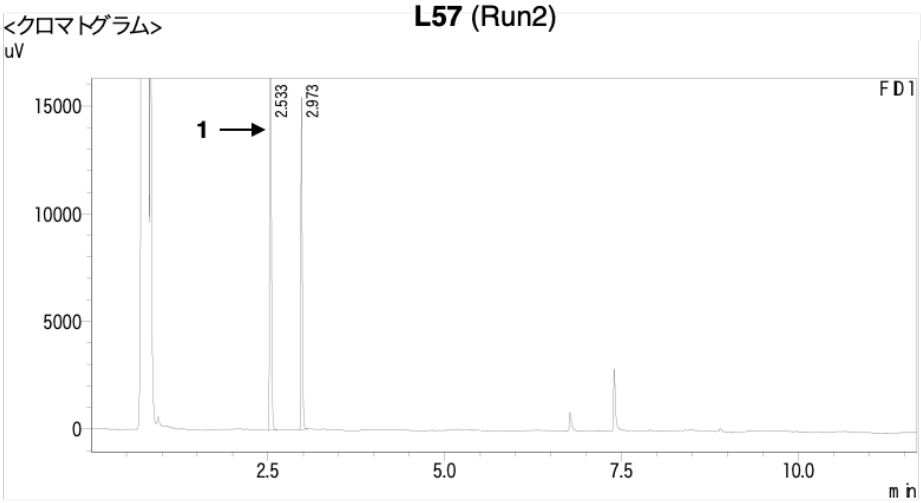

<ピークレポート>

FD1 Ret. Time Area Height

ピーク#	保持時間	面積	高さ	濃度	単位	マーク	化合物名
1	2.533	44863	32557	0.000			
2	2.973	21151	14797	0.000			
Total		66014	47354				

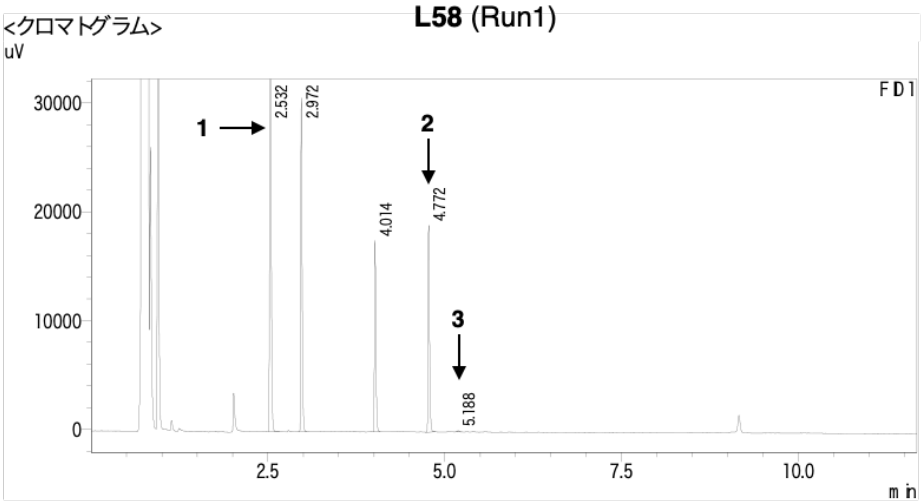

<ピークレポート>

FD1	Ret. Time	Area	Height				
ﾋﾟｰｸ#	保持時間	面積	高さ	濃度	単位	ﾏｰｸ	化合物名
1	2.532	75457	55196	44.531			
2	2.972	41254	30122	24.346			
3	4.014	24940	16915	14.718			
4	4.772	27644	18749	16.314			
5	5.188	154	105	0.091		M	
Total		169450	121087				

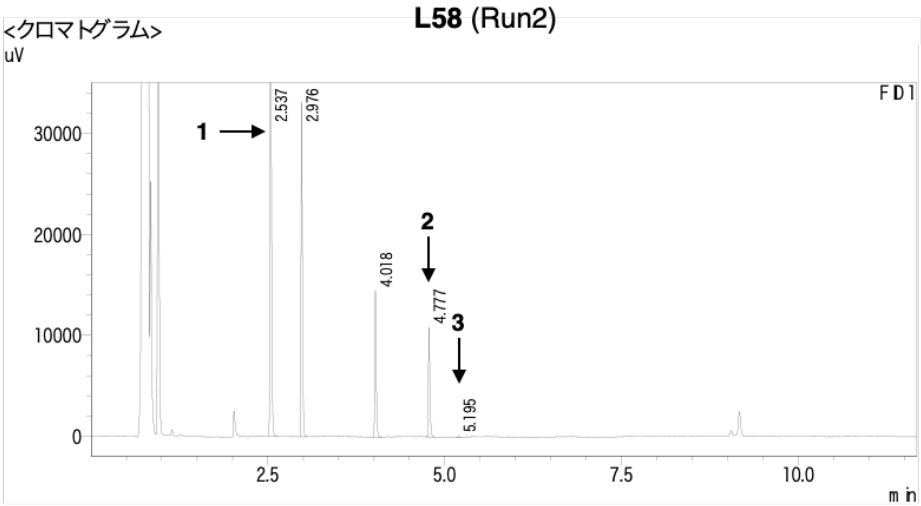

<ピークレポート>

FD1	Ret. Time	Area	Height				
ﾋﾟｰｸ#	保持時間	面積	高さ	濃度	単位	ﾏｰｸ	化合物名
1	2.537	87099	63635	51.683			
2	2.976	44722	32802	26.537			
3	4.018	20591	14014	12.218			
4	4.777	15987	10765	9.486			
5	5.195	128	76	0.076		M	
Total		168527	121292				

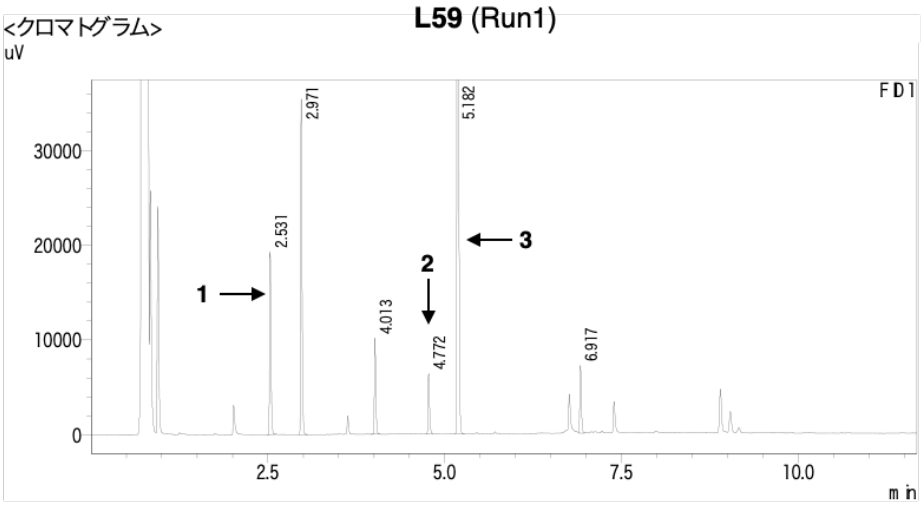

<ピークレポート>

FD1	Ret. Time	Area	Height				
ﾋﾟｰｸ#	保持時間	面積	高さ	濃度	単位	ﾏｰｸ	化合物名
1	2.531	26307	18806	9.483			
2	2.971	47566	34932	17.146			
3	4.013	14317	9978	5.161		V	
4	4.772	9292	6231	3.349		M	
5	5.182	169047	117028	60.938			
6	6.917	10882	6885	3.923		V	
Total		277411	193860				

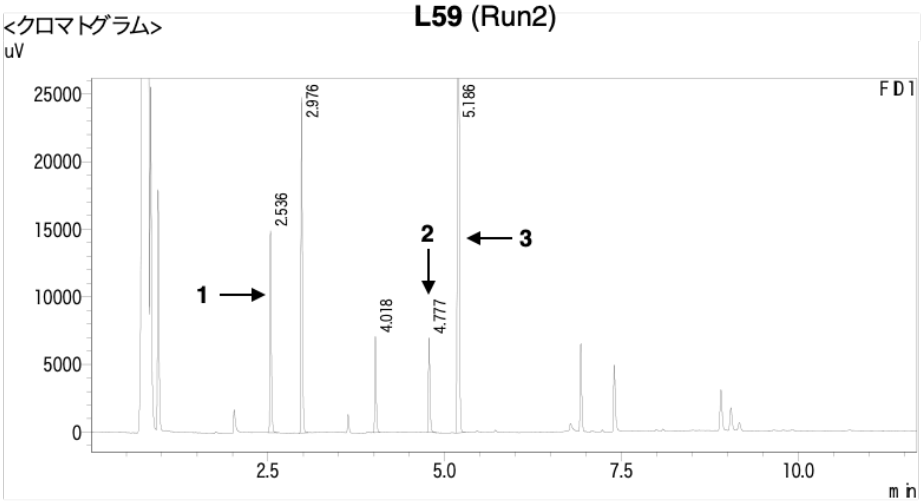

<ピークレポート>

FD1	Ret. Time	Area	Height				
ﾋﾟｰｸ#	保持時間	面積	高さ	濃度	単位	ﾏｰｸ	化合物名
1	2.536	20669	14405	0.000			
2	2.976	33812	24426	0.000			
3	4.018	10091	6923	0.000		V	
4	4.777	10508	6954	0.000			
5	5.186	109606	75291	0.000			
Total		184686	128000				

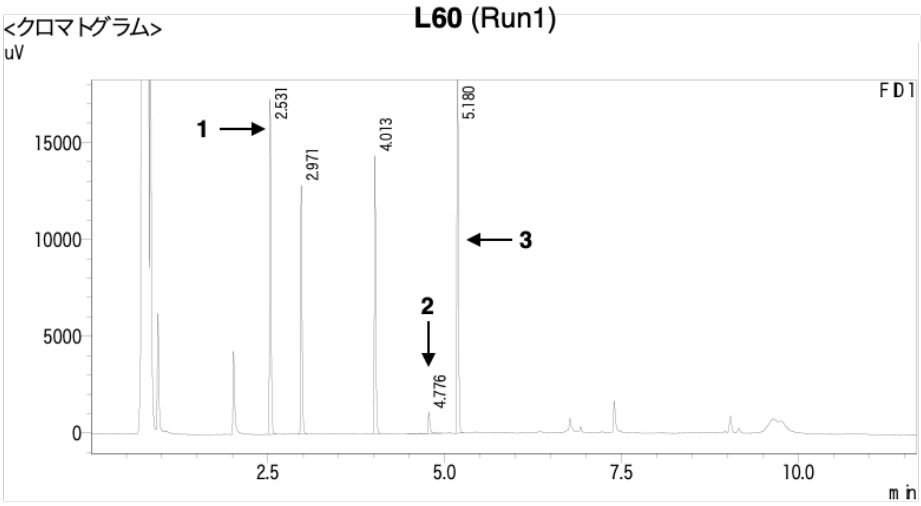

<ピークレポート>

FD1	Ret. Time	Area	Height				
ﾋﾟｰｸ#	保持時間	面積	高さ	濃度	単位	ﾏｰｸ	化合物名
1	2.531	23755	16827	25.259			
2	2.971	17573	12680	18.686			
3	4.013	20386	14123	21.677			
4	4.776	1814	1066	1.929		M	
5	5.180	30517	20932	32.449			
Total		94045	65628				

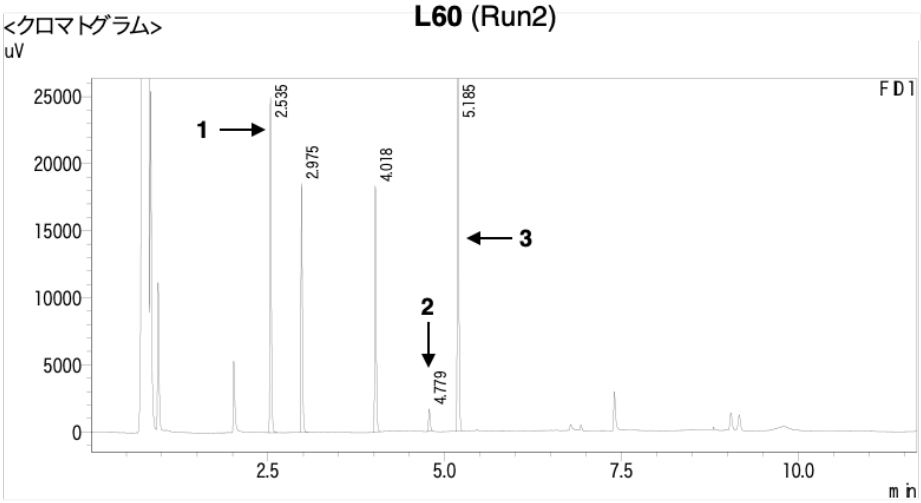

<ピークレポート>

FD1	Ret. Time	Area	Height				
ﾋﾟｰｸ#	保持時間	面積	高さ	濃度	単位	ﾏｰｸ	化合物名
1	2.535	34134	23960	25.497			
2	2.975	25269	18275	18.875			
3	4.018	26068	18051	19.472			
4	4.779	2469	1598	1.844		M	
5	5.185	45933	31909	34.311			
Total		133873	93793				

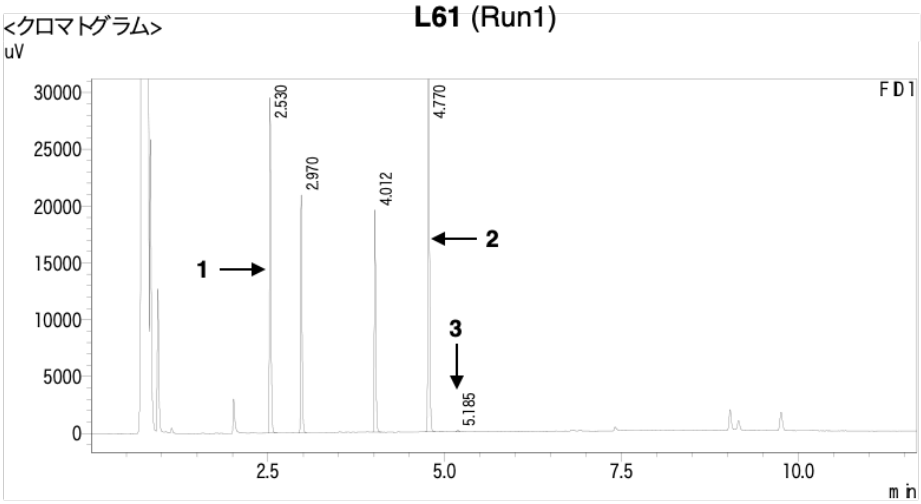

<ピークレポート>

FD1	Ret. Time	Area	Height				
ピーク#	保持時間	面積	高さ	濃度	単位	マーク	化合物名
1	2.530	40018	28188	24.805			
2	2.970	28399	20588	17.603			
3	4.012	27532	19347	17.066			
4	4.770	65184	43735	40.404			
5	5.185	196	115	0.122		M	
Total		161329	111972				

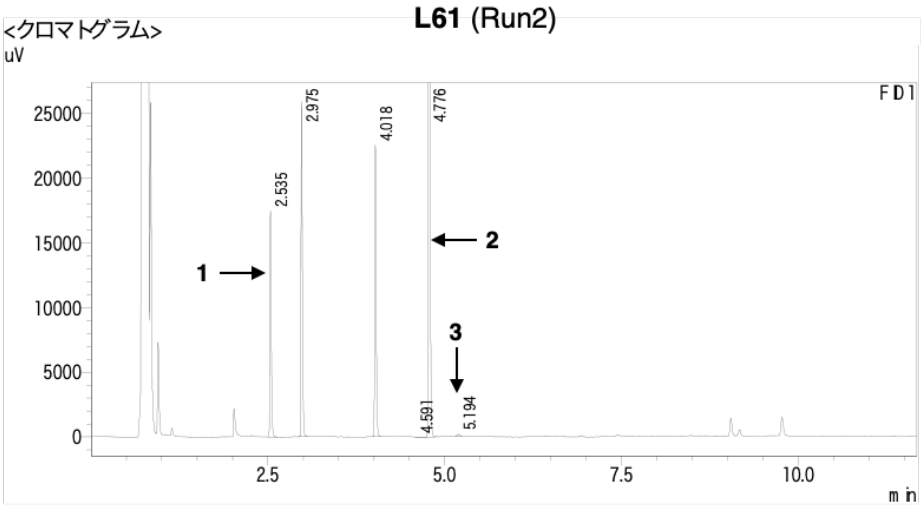

<ピークレポート>

FD1	Ret. Time	Area	Height				
ピーク#	保持時間	面積	高さ	濃度	単位	マーク	化合物名
1	2.535	24001	16839	11.995			
2	2.975	34900	25492	17.442			
3	4.018	31764	22123	15.875			
4	4.591	31	11	0.015		M	
5	4.776	109094	74490	54.523			
6	5.194	297	152	0.148		M	
Total		200087	139106				

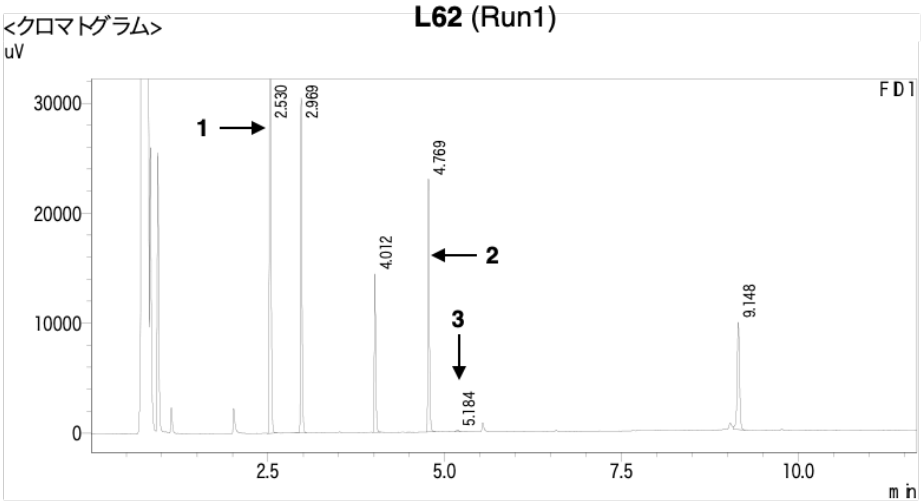

<ピークレポート>

FD1 Ret. Time Area Height

ピーク#	保持時間	面積	高さ	濃度	単位	マーク	化合物名
1	2.530	80104	57368	40.480			
2	2.969	41129	29422	20.784		V	
3	4.012	20340	14242	10.279			
4	4.769	33299	22511	16.827			
5	5.184	276	126	0.140		M	
6	9.148	22737	9666	11.490		V	
Total		197885	133336				

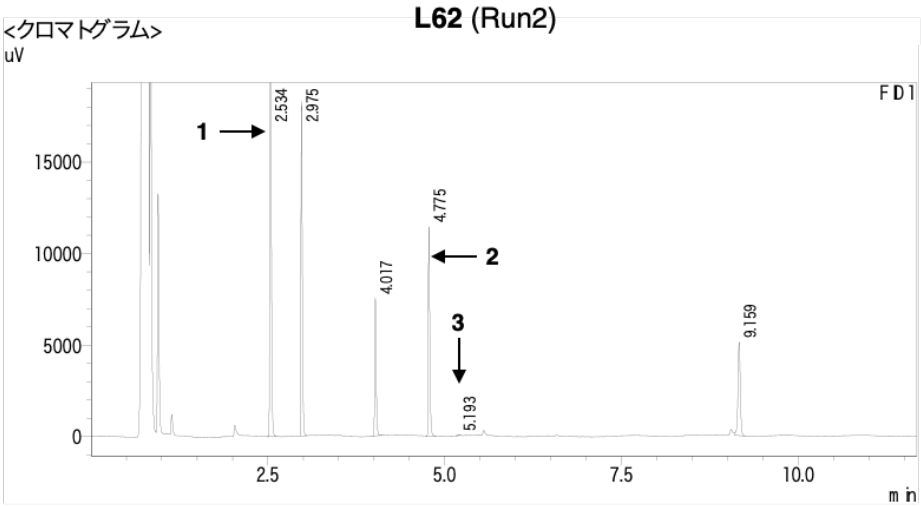

<ピークレポート>

FD1 Ret. Time Area Height

ピーク#	保持時間	面積	高さ	濃度	単位	マーク	化合物名
1	2.534	40967	28948	38.888			
2	2.975	24751	17862	23.495			
3	4.017	10831	7396	10.281			
4	4.775	16963	11029	16.102			
5	5.193	119	56	0.113		M	
6	9.159	11716	5089	11.121		V	
Total		105348	70381				

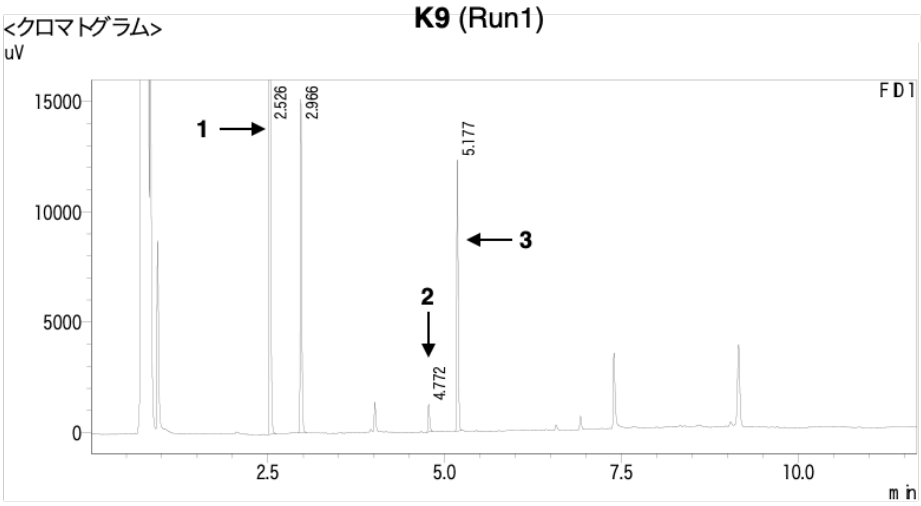

<ピークレポート>

FD1 Ret. Time Area Height

ピーク#	保持時間	面積	高さ	濃度	単位	マーク	化合物名
1	2.526	42892	30152	51.711			
2	2.966	20629	14775	24.871			
3	4.772	1973	1229	2.379		M	
4	5.177	17451	11910	21.039			
Total		82945	58065				

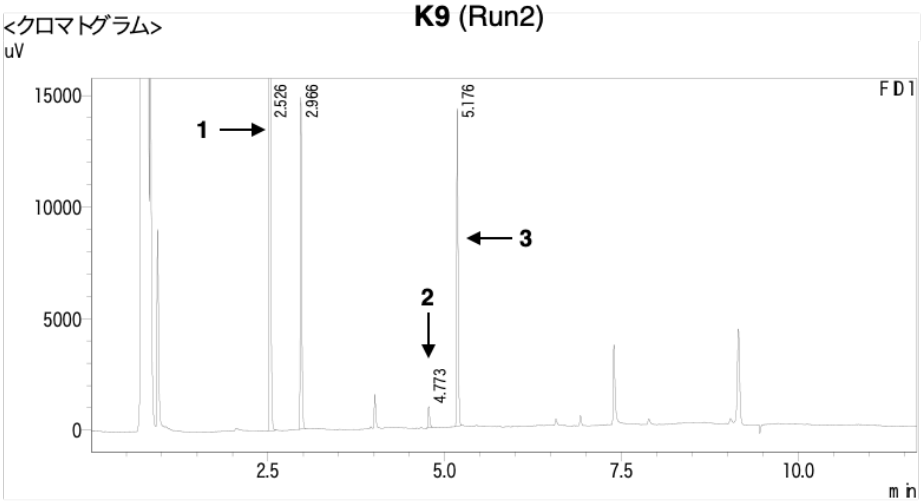

<ピークレポート>

FD1 Ret. Time Area Height

ピーク#	保持時間	面積	高さ	濃度	単位	マーク	化合物名
1	2.526	44761	31429	51.585			
2	2.966	20299	14633	23.394			
3	4.773	1478	934	1.703		M	
4	5.176	20234	13690	23.318			
Total		86771	60687				

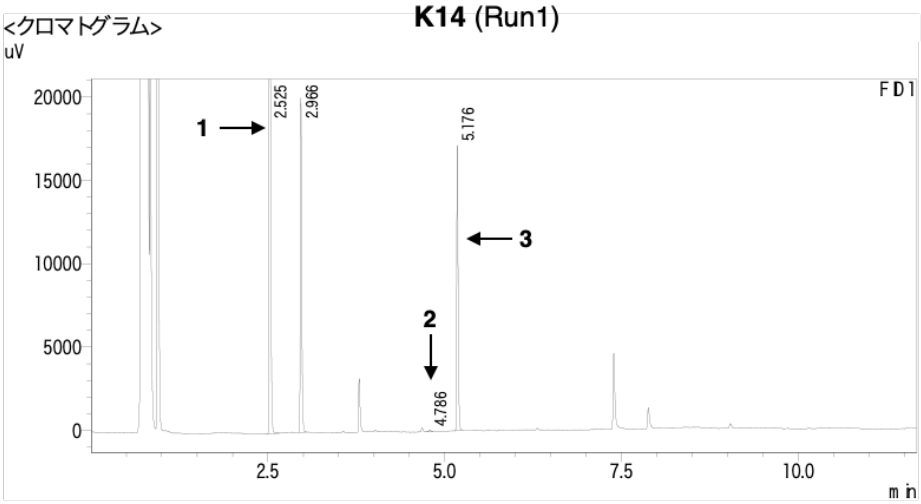

<ピークレポート>

FD1 Ret. Time Area Height

ピーク#	保持時間	面積	高さ	濃度	単位	マーク	化合物名
1	2.525	54970	38328	51.521			
2	2.966	27453	19711	25.730			
3	4.786	173	92	0.162		M	
4	5.176	24100	16439	22.587			
Total		106696	74570				

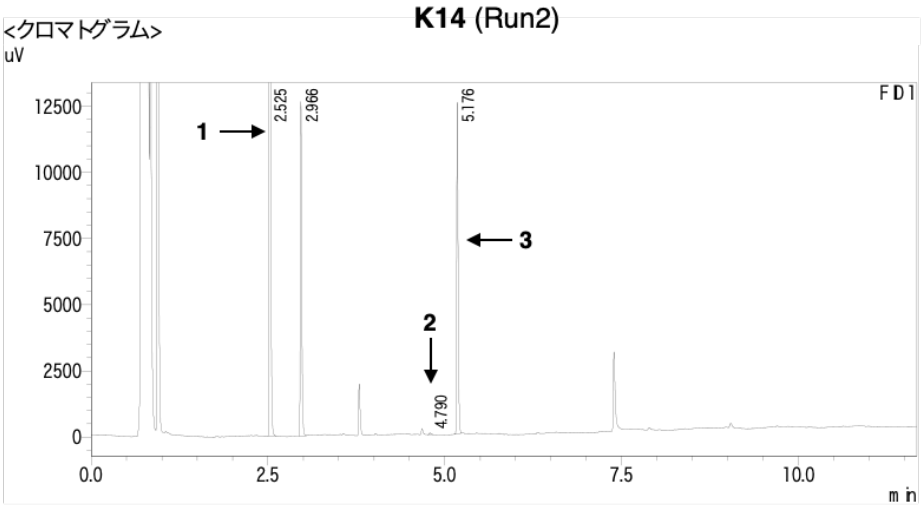

<ピークレポート>

FD1 Ret. Time Area Height

ピーク#	保持時間	面積	高さ	濃度	単位	マーク	化合物名
1	2.525	37459	26037	51.517			
2	2.966	17362	12453	23.878			
3	4.790	98	58	0.135		M	
4	5.176	17793	12010	24.470			
Total		72713	50557				